Final Technical Report

NASA Cooperative Agreement NCC2-551

"OBSERVATIONAL RESEARCH ON STAR AND PLANETARY SYSTEM FORMATION"

July 10, 1998

by

Janet P. Simpson,
Principal Investigator
SETI Institute

1

INTRODUCTION:

NCC 2–551 was originally awarded to the SETI Institute in 1988, and in 1991 was renewed for three more years. In September of 1994, an additional three years were awarded ending in FY 1997.

NCC 2–551 was originally formed to enable SETI Institute scientists to collaborate with a number of NASA Ames scientists on observational studies of star and planetary system formation to their mutual benefit. As part of this collaboration, SETI scientists have, from 1988 to the present:

(i) Contributed to the technical studies at NASA Ames of the Stratospheric Observatory for Infrared Astronomy (SOFIA), an infrared 2.5 meter telescope in a Boeing 747, which will replace the Kuiper Airborne Observatory (KAO), a 0.9 meter telescope in a Lockheed C-141. SOFIA will be an important facility for the future exploration of the formation of stars and planetary systems, and the origins of life, and as such will be an important future facility to SETI scientists;

(ii) Worked with the Laboratory Astrophysics Group at Ames, carrying out laboratory studies of the spectroscopic properties of ices and pre-biotic organics, which could be formed in the interstellar or interplanetary media;

(iii) Helped develop a photometric approach for determining the Frequency of Earth-Sized Inner Planets (FRESIP) around solar-like stars, a project (now called Kepler) which complements the current efforts of the SETI Institute to find evidence for extraterrestrial intelligence; and

(iv) Carried out independent observational research, in particular research on the formation of stars and planetary systems using both ground-based telescopes as well as the KAO.

During FY 1995 the science projects (ii) and (iii) above were for the most part moved to two different cooperative agreements at the SETI Institute, NCC 2-850 (Dr. Salama as P.I.) and NCC 2-867 (Dr. Jenkins as P.I.), respectively. Due to these changes, the personnel level supported by NCC 2-551 during the years from 1995 through 1997 decreased to: Dr. Davidson (Principal Investigator), Ms. Savage (Associate Research Scientist), Mr. McDonald (Associate Research Scientist, who replaced Mr. Ford in FY95), and Ms. Sablan (Science Aide, who replaced Ms. Willoughby in FY96). Mr. Granados and Mr. Pham, who worked on the FRESIP project through this cooperative agreement before FY 1995, ended their association with NCC 2-551, and the SETI Institute, in late 1995. The FRESIP funds remaining in NCC 2-551 after their departure were used to support FRESIP efforts by Mr. McDonald into FY 1996, who also worked on occultation studies (see below). The FRESIP efforts were carried out in collaboration with Dr. Jenkins.

During FY 1997, both Dr. Davidson and Ms. Savage (see below) went to work for USRA (Universities for Space Research Association), and hence were no longer funded by NCC 2-551. Unused funds in NCC 2-551 were then supervised first by Dr. Colgan and then by Dr. Simpson, both SETI Institute PIs on other cooperative agreements with NASA. The unused funds were used by Ms. Sablan and Mr. McDonald, until the funds were depleted in late FY 1997.

SUMMARY OF WORK COMPLETED FROM FY 1995 THROUGH FY 1997

A. SOFIA Studies:

During FY 1995, Dr. Davidson, assisted by Ms. Willoughby:

       (i) Edited the Airborne Astronomy Symposium Proceedings which was published in March 1995 as the 73rd volume in the Astronomical Society of the Pacific (A.S.P) Conference Series;

       (ii) Helped organize advocacy efforts within the science community for Airborne Astronomy, and for SOFIA in particular;

       (iii) Attended SOFIA Science Working Group Meetings during 1995; and

       (iv) Reviewed existing documents on SOFIA science requirements (document SOF-1009 in particular) and translated these to technical specifications for the observatory (document SOF-1011 in particular).

In the beginning of FY 1996, Dr. Davidson assisted by Ms. Sablan, continued to work as a scientific advisor to the SOFIA Project Office at Ames. However, starting in February 1996, she ceased to be apart of the SOFIA Project Office effort in order to participate in the USRA Team's bid to win the NASA contract for the development and operation of SOFIA. Funds for Dr. Davidson's effort on the USRA Team's proposal were paid to the SETI Institute by USRA; NASA funds were not used to support this effort in any way.

In December of 1996, NASA announced that the USRA Team had won the SOFIA contract. At this time, Dr. Davidson ceased to be a SETI Institute employee and became the SOFIA Project Scientist for USRA: Consequently, at that time, the SOFIA studies by this Cooperative Agreement ended. Ms. Sablan then concentrated on observational research under this grant.

B. FRESIP (Kepler) Project:

During FY 1995, Mr. Granados carried out research on CCD camera hardware and software in regards to the FRESIP photometer design, especially in regards to camera stability characteristics. Mr. Pham studied solar variability based on the data from Solar Max Acrim 1. The results of this study were used to determine the sensitivity limits of FRESIP to detect small planets.

During late FY 1995 and FY 1996, Mr. McDonald worked on long-term stability and photometric tests of the FRESIP CCD camera system. In addition, he implemented a liquid nitrogen fill system for the CCD camera. This system supported the camera for several days between fills and reduced the physical shock to the camera due to such fills.

C. Observational Studies:

During FY1995, Dr. Davidson, assisted by Ms. Savage:

> (i) Continued work on the construction of the ADR/Fabry-Perot Interferometer in collaboration with scientists at Ames and Cornell University;
> (ii) Gave a review talk/paper at a conference on Polarimetry, and attended and presented a paper at a conference on Magnetohydrodynamics in Astrophysics;
> (iii) Studied from the KAO and various ground-based observatories: the magnetic field structure in the Galactic Center, the luminosity variability of embedded protostars, and the "turn-on epoch" of protostar outflows; and
> (iv) Finished a paper for the Astrophysical Journal on the Galactic Center.

The ADR/Fabry-Perot Interferometer is an extension of the ADR photometer which was built by Dr. Davidson and Ms. Savage during 1991–1994. It will be a very sensitive submillimeter spectrometer to be used on ground-based telescopes to study the interstellar medium of close and distant galaxies. It will eventually be used on a telescope at the South Pole.

During FY1995, Mr. McDonald

> (i) Replaced Mr. Ford in June (see Mr. Ford's tasks as listed in the 1995 NCC 2–551 renewal proposal);
> (ii) Worked on occultation predictions at Lick Observatory;
> (iii) Observed the Triton/Tr 148 occultation at Lick Observatory;
> (iv) Worked on astrometry data analysis; and
> (v) Helped with noise reduction in an occultation CCD camera system.

Occultation observations are used to determine the physical nature of the atmospheres of the planets and their moons in our solar system.

During FY1996, Dr. Davidson, with assistance from Ms. Savage and Ms. Sablan:

> (i) Continued work on the construction of the ADR/Fabry-Perot Interferometer in collaboration with scientists at Ames and Cornell University;
> (ii) Reduced data from 1995 KAO observations, which were made to study the luminosity variability of embedded protostars;
> (iii) Prepared two papers for the Astrophysical Journal, one on the infrared variability of the embedded source in B5, the other on the far-IR luminosity in the Arched Filaments near the Galactic Center; and
> (iv) Assisted with the preparations and running of the Symposium "From Stardust to Planetesimals", held at the University of Santa Clara in June 1996, and hosted by NASA Ames and the Astronomical Society of the Pacific.

The ADR/Fabry-Perot Interferometer development in 1996 involved integrating detectors into the ADR and testing them electrically, and integrating the ADR dewar to the Cornell University

Fabry-Perot dewar. This was done at Cornell University in August of 1996. Mechanically the integration was a success.

During FY1996, Mr. McDonald:

(i) Worked on astrometry data analysis and occultation predictions;
(ii) Helped with noise reduction in a occultation CCD camera systems;
(iii) Participated in occultation observations of 51 Pegasi at Lick Observatory;

During FY 1996 and 1997, Ms. Sablan worked with Drs. Colgan and Simpson on the development of an Airborne Infrared EchelleSpectrometer for SOFIA called AIRES. This involved assisting in preparing the proposal to NASA (which was accepted in October, 1997) and various laboratory tests of prototype gratings and detectors. She also studied bowshock structures on HST-NICMOS images of OMC-1 in Orion.

III. PUBLICATIONS

Reviewed Publications in 1995 through 1997:

Telesco, C.M., Davidson, J.A., and Werner, M.W., "10 - 30 μm Maps of the Central 5 pc of the Galaxy: Heating of the Cavity and Neutral-Gas Disk", Ap.J. 456, 541-556 (1996).

Davidson, J.A., Morris, M., Harvey, P.M., Lester, D.F., Smith, B., and Werner, M.W., "Far-Infrared Emission from the Thermal Arched Filaments", Ap. J. (in preparation)

Charnley, S., Savage, M., Davidson, J.A., and Pendleton, Y., "The Infrared Variability of the Embedded YSO B5 IRS1", Ap.J. (in preparation)

Proceedings in 1995 through 1997 due to NCC 2–551 :

J.A. Davidson, D. Schleuning, J.L. Dotson, C.D. Dowell, and R.H. Hildebrand, "The Magnetic Field Structure in High-Mass Star Formation Regions", in Airborne Astronomy Symposium on the Galactic Ecosystem: From Gas to Stars to Dust, eds. M.R. Haas, J.A. Davidson, and E.F. Erickson, San Francisco: ASP, 225 (1995).

J.A. Davidson, "The Magnetic Field Structure in the Galactic Center" in Polarimetry of the Interstellar Medium, eds. W. Roberge and D. Whittet, San Francisco: ASP (1996).

Stacey,G.J., Bradford, C.M., Swain, M.R., Jackson, J.M., Bolato, A.D., Davidson, J.A., and Savage,M., "The South Pole Imaging Fabry Perot Interferometer (SPIFI)" in Submillimeter and Far-Infrared Space Instrumentation, ESTEC, Noordwijk, The Netherlands, ESA SP-388 (1996).

Books produced in 1995 through 1997 due (in part) to NCC 2-551 :

A.S.P. Conference Series Vol. 73, "Airborne Astronomy Symposium on the Galactic Ecosystem: From Gas to Stars to Dust", eds. M.R. Haas, J.A. Davidson, and E.F. Erickson, San Francisco: ASP (1995).

SOFIA Reports and Documents prepared in 1995 through 1997 due (in part) to NCC 2-551:

"SOFIA: The Future of Airborne Astronomy", by E.F. Erickson and J.A. Davidson, 1995

SOF-1009   SOFIA Science Rationale
SOF-1011   SOFIA Telescope Requirements Document

"Tertiary Mirror Size for SOFIA", by J.A. Davidson, November 1995.

THE SOUTH POLE IMAGING FABRY PEROT INTERFEROMETER (SPIFI)

G.J. Stacey[1], C.M. Bradford[1], M.R. Swain[1], J.M. Jackson[2], A. D. Bolatto[2], J.A Davidson[3], and M. Savage[3]

[1] Department of Astronomy, Cornell University, Ithaca, NY 14853
[2] Department of Astronomy, Boston University, Boston, MA 02215
[3] SETI Institute, NASA/Ames Research Center, Mountain View, CA 94035

ABSTRACT

We have designed and constructed the South Pole Imaging Fabry-Perot Interferometer (SPIFI). SPIFI is a direct detection imaging spectrometer for use in the far-IR and submm bands (200, 350, 450 and 600 μm) accessible to the 1.7m AST/RO telescope at the South Pole, and in the submm bands accessible to the 15m JCMT. SPIFI employs a 5 × 5 silicon bolometer array, and three cryogenic Fabry-Perot interferometers in series to achieve velocity resolutions between $\Delta v \sim 300$ and 30 km s^{-1} over its entire field of view. Much higher resolution - up to 1 km s^{-1} - is possible for the central pixel. At 370 μm, SPIFI's beam is 55" and 7", and field of view is 300" × 300" and 38" × 38" respectively for AST/RO and JCMT. SPIFI should be 45, 15 and 4 times more sensitive at 200, 350 and 450 μm respectively *per pixel* than the best heterodyne systems for lines well matched to the velocity resolution. In addition, for mapping projects, the 25 element array offers a *factor of 25 spatial multiplex gain*. SPIFI is completely fabricated, and undergoing cryogenic tests at Cornell. We hope to use SPIFI on JCMT in 1997.

Scientific goals for SPIFI include large scale maps in the $^3P_2 \rightarrow ^3P_1$ (370 μm) [CI] and $^3P_1 \rightarrow ^3P_0$ (205 μm) [NII] fine-structure lines, and the CO (7 → 6) and (6 → 5) rotational transitions of star formation regions, the Galactic Center, and nearby galaxies. In addition, the SPIFI-JCMT combination can detect [CII] (158 μm) line emission from distant galaxies. In 4 hours, SPIFI can detect [CII] lines from bright ($L_{far-IR} > 3 \times 10^{11}$ $L_\odot$) galaxies at z ~ 1.2. [CII] emission traces the ambient far-UV stellar radiation fields, so that these observations probe star formation in the epoch of galaxy formation.

Keywords: Direct Detection, Bolometers, Fabry-Perot, Submillimeter, Far-Infrared.

1. SCIENTIFIC JUSTIFICATION

Stars form from condensations within molecular clouds. The detailed mechanisms along the pathway from molecular cloud through condensation and collapse to stars, however, is not well understood. Our scientific interests center on the interactions between the newly formed stars and the nascent interstellar medium (ISM).

The far-IR and submm spectral windows available to SPIFI pass spectral lines that provide unique diagnostics of the physical conditions in the ISM (Table 1). These lines are unaffected by interstellar extinction so that the dusty environments associated with star formation and galactic nuclei are accessable for study. Furthermore, the fine-structure line emitting levels require little kinetic energy for excitation, and are collisionally excited at modest densities. Therefore, they are both sensitive physical probes and important coolants for much of the low density ionized and molecular ISM.

The [CI] lines were predicted to be strong from the warm, dense photodissociation regions (PDRs) at the surface of far-UV (6 eV $\leq$ hν < 13.6 eV) exposed molecular clouds [1]. Observations of the 609 μm line, however, indicate that [CI] emission arises from the bulk of the molecular cloud as well [2,3]. Since the [CI] lines are optically thin, they may, in fact, be better tracers of molecular cloud structure and mass than the (very optically thick) low-J CO lines. The [CI] lines penetrate cloud cores, so that they can be used to trace morphology, excitation, mass, and dynamics in embedded structures such as molecular disks confining molecular flows, or the circumnuclear ring (CNR) at our Galactic Center [4].

TABLE 1
SPECTRAL LINES AVAILABLE TO SPIFI

Species n_{crit}[2]	Transition	E.P.[1] (K)	λ (μm)	A (s^{-1})	(cm^{-3})
N$^+$	$^3P_1 \rightarrow ^3P_0$	70	205.178	2.1 E-6	48
C^o	$^3P_2 \rightarrow ^3P_1$	63	370.415	2.7 E-7	1200
	$^3P_1 \rightarrow ^3P_0$	24	609.135	7.9 E-8	470
^{12}CO	J=13 → 12	503	200.273	2.4 E-4	5.6 E6
^{12}CO	J = 7 → 6	155	371.651	3.6 E-5	3.9 E5
^{12}CO	J = 6 → 5	116	433.338	2.2 E-5	2.6 E5
^{13}CO	J = 6 → 5	111	453.497	2.0 E-5	2.3 E5
HCN	J = 9 → 8	191	375.944	2.5 E-2	2 E9
HCO$^+$	J = 9 → 8	193	373.593	2.5 E-2	9 E7

[1] Excitation potential: energy of upper level above ground.
[2] Critical Density. Molecules: Collision partner H$_2$ (100 K). Atoms: [CI] (H atoms), [NII] (electrons).

The mid-J CO lines trace substantially higher density gas than the low-J CO or [CI] lines. They trace density clumps in PDRs, and shock excited gas. The mid-J lines are prominent in the CNR [5], Galactic outflow sources [6,7], and interface regions [8,9].

[NII] emission arises from low density HII regions. Observations of the 205 μm line (not available to ISO), together with ISO 122 μm observations constrain the density of the gas. Together with ISO [NIII] (57 μm), [OIII] (52 and 88 μm), and [CII] fine-structure line observations, the [NII] lines yield the hardness of the ambient radiation fields (earliest type stars), and the interstellar N/O ratio, hence age (degree of processing) of

the ISM, and the cooling of the ionized ISM. [NII] (205 μm) and [CII] line comparisons are of particular interest. Recent observations of external galaxies and the Milky Way [10,11] suggest that much (30 to 60%) of the [CII] emission from the galactic disk arises from *either* diffuse ionized gas, or "standard" atomic clouds. N^+ is only found in HII regions, while C^+ is found both in HII regions, and far-UV exposed neutral clouds (including atomic clouds). Since the 205 μm line has the same density dependence in HII regions as the [CII] line, a simple line ratio yields the fraction of [CII] that arises from HII regions - hence the fraction from atomic clouds - subject only to an N/C abundance ratio. Since half of the mass of the ISM is in atomic clouds, and the [CII] line cools these clouds, these observations are crucial for galactic ISM studies. The 200 μm window requires the very low water vapor at the South Pole site (see below), so that SPIFI-AST/RO is the only platform for [NII] studies until SOFIA.

Also listed in Table 1 are the J= 13 → 12 (CO) and J = 9 → 8 (HCN and HCO$^+$) rotational transitions, which trace very high density or shocked gas which will only be detectable in bright galactic sources (e.g. Orion, [12]).
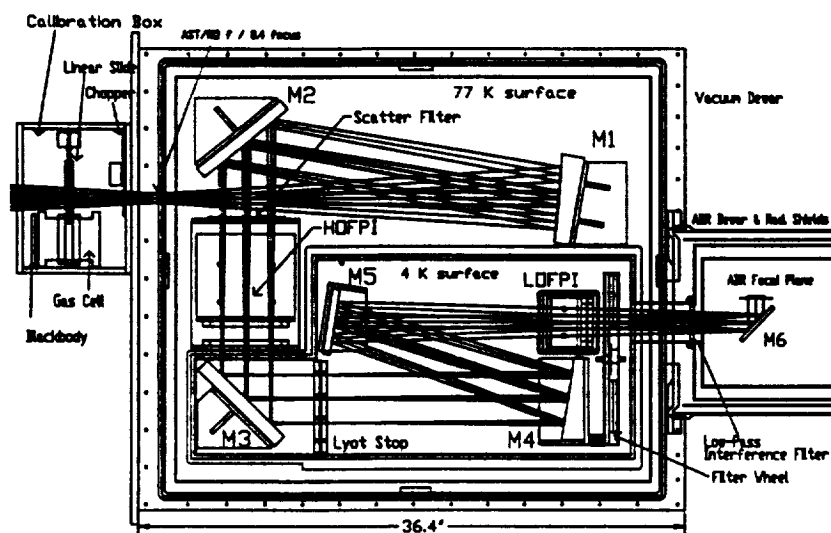
Monochrometers, such as grating spectrometers and Fabry-Perot interferometers (FPIs) are the spectrometers of choice for background limited systems. However, for spectral resolutions ~ $\lambda/\Delta\lambda$ = 10,000 at 370 μm, a single pass grating needs to be > 1.8 meters long! Clearly a multiple pass instrument such as a FPI is preferred. This choice is strengthened by the spatial multiplexing afforded by our 5 x 5 array of bolometers.

2.2. Optical Path.

SPIFI is an imaging spectrometer based on three cryogenic Fabry-Perots in series and a 5 x 5 detector array in an ADR. Figure 1 illustrates SPIFI's optical path.

SPIFI was designed to mount on the azimuth arm pedestal of the AST/RO telescope accessing an f/8.3 Naysmith focus. To mount on the JCMT left Naysmith arm, will require an f-converter. The beam transits the calibration module, containing a gas cell and blackbody for spectral calibration and flat fielding, reaches a focus just outside of SPIFI, then enters the main dewar via a polyethylene window. Mirrors M1 and M2 are at IN_2 temperature, and M3, M4 and M5 are at lHe temperature.

Figure 1. SPIFI Optical Path

2. SPIFI DESIGN

2.1. Why an Imaging Fabry-Perot?

Nearly all astronomical spectroscopy to date in the submillimeter band has been performed with heterodyne receivers using Schottky diodes, or SIS junctions as mixers. These receivers are likely to remain the instruments of choice at the highest spectral resolutions - resolutions sufficient to obtain detailed velocity profiles of galactic sources. However, bolometer materials and fabrication techniques have reached a stage of sophistication such that background limited *direct detection* is possible in the submm bands at spectral resolutions up to a few km s^{-1}. It can be shown that *in principle* a background limited Fabry-Perot is more sensitive *per pixel* than a coherent system if the receiver noise temperature of the coherent system is more than three times the quantum limit! [13]. Clearly, for low to moderately high spectral resolution at high frequencies, direct detection is better.

The final mirror, M6 is in the ADR dewar, at 4 K. The beam is collimated at 9 cm by M1, and is sent through the scatter filter and high order FPI (HOFPI) via flat mirror, M2. The scatter filter rejects wavelengths shortward of 70 μm. Flat mirror M3 directs the beam through the lHe temperature Lyot stop to the decollimator, M4. From here, flat mirror M5 directs the beam through the low order FPI (LOFPI), the filter wheel, containing fixed 1st order FPI's, and the 300 μm low pass filter on its way into the ADR. Flat M6 then directs the beam to the Winston cones of the bolometer array. The final f# is 12.6, so that the mirrors M1 and M4 are nearly in a Czerny-Turner configuration, minimizing coma. Ray tracing indicates the spot size for worst (most off-axis) pixels is < 1 mm, well below the diffraction limited beam size of 5.6 mm.

2.3. Cryogenic Fabry-Perots.

Our scientific goal is to map sources with intrinsic line widths which range from ~ 300 km s^{-1} to as small as ~ 10 km s^{-1}. The resolving power of a FPI is given by R =

NEF/Ω, and the equivalent (SSB) system temperature at wavelengths of interest. The first row at each wavelength is for R = 10,000, and the second row is for R = 1000.

At 370 μm, the point source NEF for SPIFI-JCMT is ~ 6 times better than for the SPIFI-AST/RO combination since the JCMT has 78 times more collecting area, but the Mauna Kea sky is only ~ 30% transparent, and the JCMT aperture is ~ 20% efficient.

TABLE 2
EXPECTED SENSITIVITIES FOR SPIFI on AST/RO

λ (μm)	Beam (arcsec)	Ω_{BEAM} (sr)	NEF (W cm^{-2} Hz$^{-1/2}$)	NEI (erg s^{-1}cm^{-2} sr^{-1}Hz$^{-1/2}$)	T_{rec}(SSB) (K)
200	30	2.4 E-8	1.17 E-20	5.0 E-6	111
			3.70 E-20	1.5 E-5	111
370	55	8.0 E-8	7.23 E-21	9.1 E-7	94
			2.29 E-20	2.9 E-6	94
434	65	1.1 E-7	6.40 E-21	5.8 E-7	90
			2.03 E-20	1.8 E-6	90
609	90	2.1 E-7	4.96 E-21	2.3 E-7	82
			1.56 E-20	7.3 E-7	82

Note: T_{rec}(SSB) is the equivalent *single side-band* heterodyne receiver temperature to give the system NEI's quoted for SPIFI. We do not include the spectral multiplex advantage of the heterodyne system, or the spatial multiplex advantage for SPIFI. In the tradition of FIR spectroscopy, we have referred the NEP's, NEF's and NEI's to the sky, i.e. they include all losses due to telescope coupling, sky transparency, chopping, nodding etc. T_{rec}(SSB) refers to the input to the receiver, i.e. it does not include these losses.

These sensitivities are quite good. To map the entire CNR (400 × 200" region) in the [CI] 370 μm line (SNR ~ 35) at 7" resolution with SPIFI-JCMT takes just 7 hours of integration time (50% efficiency). SPIFI-ASTRO can detect the diffuse [CI] and [NII] line emission (SNR ~ 25 and 50, respectively) from *between* M83's spiral arms in four hours of integration time. With AST/RO SPIFI can map the entire thermal arches region of the Galactic center in the [CI] and [NII] lines in less than an hour per line (SNR > 50 → 100). SPIFI-JCMT can detect redshifted [CII] emission from distant IR bright galaxies. A moderately bright ($L_{farIR} > 3 \times 10^{11} L_\odot$) galaxy emits > 1.2 × 10^9 $L_\odot$ in the [CII] line [18]. SPIFI-JCMT can detect (SNR ~ 7) such a line in 4 hours integration time.

4. COMPARISON WITH COHERENT SYSTEMS.

SPIFI NEI's given above, include all loses. To properly compare SPIFI with heterodyne systems receiver temperatures, T_{rec}(SSB), we must remove the forward losses: telescope coupling (<50% - single polarization), nodding ($\sqrt{2}$), chopping ($\sqrt{2}$), and sky transmission (t_{sky} ~ 75%). SPIFI's NEI, ΔI is then related to T_{rec} by:

$$\Delta I = 2 \cdot 2 \cdot 1/t_{sky} \cdot (2 \, kT_{rec}(SSB) \, \Delta\nu)/\lambda^2 \cdot (\Delta t \cdot \Delta v)^{-1/2}$$

At 370 μm, SPIFI has an equivalent receiver temperature of 94 K (SSB) independent of the spectral resolution (Table 2). To build a heterodyne receiver with such a low

receiver temperature would be quite challenging, as this is only *2.4 times the quantum limit*.

The best SSB receiver temperatures that we are aware of are 5000 K [19], 1444 [20], and 350 K [21] at 1.5 THz (200 μm), 800 GHz (370 μm) and 492 GHz (609 μm) respectively. SPIFI should be therefore ~ 45, 15, and 4 times more sensitive *per pixel* than the best heterodyne receivers. While the heterodyne system spatially multiplexes, SPIFI still has to spectrally scan about 5 resolution elements, so for a point source, the efficiency of line detection is $\sqrt{5}$ worse. However, SPIFI spatially multiplexes with its 25 element array, so that for mapping projects SPIFI's efficiency is 25 times higher.

5. THE SOUTH POLE AND AST/RO

Through the Center for Astronomical Research in Antartica (CARA), the NSF funded the construction of the 1.7 m AST/RO telescope at the South Pole. AST/RO was installed at the pole in 1994 November, and is producing high quality scientific results (e.g. [22]. The South Pole is an exceptionally good site for submm astronomy. Direct radiosonde measurements taken from February through November 1995, indicate the median zenith water vapor burden was only 300 μm [17]. Often the burden gets as small as *100 microns* - suitable for observations in the *far-infrared*. For example, at the [NII] 205 μm, and CO (J = 13 → 12) 200 μm lines, the transmissions are ~ 67% during 100 μm periods, and a very usable 30% during 300 μm periods. During the winter months, *submm observations are always possible* in the 350 and 450 μm windows, and *often in the 200 μm window* as well. The surface accuracy of AST/RO's primary dish is good enough to permit observations at 200 μm: ~ 9 μm rms, or λ/40 at 370 μm and λ/23 at 205 μm.

REFERENCES

1 Tielens, A.-, & Hollenbach, D. 1985, ApJ, 291, 722.
2 Phillips, T.G., & Huggins, P.J. 1981, ApJ, 251, 533.
3 Keene, J., et al. 1985, ApJ, 299, 967.
4 Serabyn, E., et al. 1994, ApJ, 424, L95.
5 Harris, A.I., et al. 1985, ApJ, 294. L93.
6 Jaffe, D., et al. 1989, ApJ, 344, 265.
7 Mitchell, G.F., et al. 1995, ApJ, 438, 794.
8 Schmid-Burgke J., et al. 1989, A&A, 215, 150.
9 Stacey, G.J., et al. 1993 ApJ, 404, 219.
10 Madden, S.C., et al. 1993, ApJ, 407, 579.
11 Wright, N. et al. 1991, ApJ, 381, 200.
12 Stutzki, J., et al. 1988, ApJ. 330, L125.
13 Harris, A.I. 1990, ESA SP-314, 165.
14 Stacey, G.J., et al. 1995, ASP Conf. Series 73, 215.
15 Moseley, S.H. personal communication.
16 Lugten, J.B., PhD Thesis, UC Berkeley.
17 Chamberlin, et al. 1996, ApJL, submitted.
18 Stacey, G., et al. 1991, ApJ, 373, 423.
19 Boreiko, R.T., & Betz, A.L. 1993, ApJ, 405, L39.
20 Gaidis, M.C., et al. 1996, Supercond. Sci. Tech.
21 Walker, C.K., et al. 1992 IJIMM Waves.
22 Bolatto, A.D., et al. 1996, BAAS 28, 90.

$\lambda/\Delta\lambda = n \cdot F$, where F is the finesse of the cavity, and n is the order of the resonance at wavelength λ. To optimally detect lines, the spectral resolution of a background limited spectrometer should be matched to the expected source line width. Therefore, the spacing (order) between the HOFPI mirrors should be externally adjustable.

SPIFI attains high spectral resolution and high spectral purity with three FPI in series. Each FPI is constructed of free standing metal mesh, has $F \sim 30$ to 60, and transmissions $\sim 60 \rightarrow 80\%$. The orders, n, of the HOFPI ($n \sim 30 \rightarrow 2000$) are sorted by a LOFPI ($n \sim 1 \rightarrow 40$) whose orders are sorted by fixed 1st order FPIs on a filter wheel. The filter wheel holds 6 fixed FPI tuned to specific lines. Changing between lines takes only a few minutes. In addition, there is a low pass filter (P. Ade, QMW) for rejecting higher order resonances of the fixed FPI. SPIFI is therefore extremely spectrally pure at spectral resolutions as high as 2 km s^{-1}.

Light entering a Fabry-Perot off-axis sees a different path, therefore a different resonance frequency, than the normal ray. For this reason, there is both a spectral shift and reduced spectral resolution for the off axis pixels. The outermost pixels in SPIFI's array are shifted ~ 36 km s^{-1} blueward of the central pixel. Within a beam the limiting velocity resolution, $\Delta V_{min} = c + R_{max} = c \cdot \Delta\lambda_{min}/\lambda$ (km s^{-1}), is roughly the difference between the wavelength at the inner edge of the beam (at Θ_{inner}), and that at the outer edge of the beam (at Θ_{outer}) [14]:

$$\Delta V_{min} = c \cdot \Delta\lambda_{min}/\lambda = c/2 \cdot (D_p/D)^2 \cdot \{\Theta^2_{outer} - \Theta^2_{inner}\}$$

where D is the diameter of the collimated beam through the HOFPI (9 cm), and D_p is the diameter of the telescope primary. For 55" beams on the 1.7m AST/RO, we have $\Delta V_{min} \sim 24$ km s^{-1} for the corner pixels, ~ 12 km s^{-1} for the inner 9 pixels, and ~ 1 km s^{-1} for the innermost pixel.

The LOFPI design is identical in principle to that used successfully in our 35 μm imaging Fabry-Perot system for the KAO (KWIC, [14]. It is fully tunable, has a clear aperture of 6 cm, and uses a flex vane translation stage. Course adjustments to the plate separation are made via an external crank. Fine adjustments are made with a model P-245.5 (PI, Waldbronn, Germany) PZT stack which expands ~ 24 μm at /He temperature. Plate spacing is measured and stabilized with a capacitive bridge circuit using the metal mesh itself as a capacitor. The rings are electrically isolated by nylon plugs, and held in place with magnets.

To enable changes in the spectral resolution while cold, the HOFPI employs a coarse translation stage, accessible via an external crank. The stage is all stainless steel (Newport Model 462) with a travel of 2.54 cm corresponding to 137 orders at 370 μm. When the system is warm, the center position of the stage is adjustable from a gap of 1.25 cm to 10 cm ($\leftrightarrow$ R $\sim$ 30,000). For most applications, the center position will be 2.84 cm so that we can change from 25th to 162th order at 370 μm while cold. With $F \sim 60$, the resolution changes from 200 km s^{-1} to 30 km s^{-1}. In one configuration, then, SPIFI is both well matched to the broad line widths in galaxies, and optimized for mapping the narrow lines in Galactic molecular clouds. Scanning within a spectral order is attained with a PI model P-239.90 PZT, which pushes a flex vane stage riding piggy-back on the coarse stage. At /N$_2$ temperatures, this PZT translates 60 μm, or 60 μm +

$(\lambda/(2 \cdot F)) = 20$ resolution elements (370 μm, $F = 60$) - ample for any application. The HOFPI mirror gap is large, precluding their use as linear capacitors in a bridge circuit. Therefore, we use an "outrigger" capacitor to achieve linearity in spectral scanning. The clear aperture of the HOFPI is 12 cm.

Spectral calibration is achieved via absorption lines (e.g. CO) from a gas cell in front of a chopped blackbody. The blackbody also serves for both spatial and spectral flat fielding.

2.4. ADR and Detector Array.

To be background limited at high spectral resolution in the submillimeter requires bolometer temperatures < 100 mK, which we achieve with an adiabatic demagnetization refrigerator (ADR). One of us (JAD) developed an ADR for use with a 5 × 5 bolometer array for broad band ($\lambda/\Delta\lambda \sim 5$) work at 800 μm on the CSO. The ADR achieves controlled focal plane temperatures between 50 and 100 mK for about 16 hours before thermal cycling, and was modified for use with SPIFI. The ADR and SPIFI dewars share vacuum to prevent the large background from any warm intermediary windows from seriously affecting the sensitivity. The ADR bolts to the aft end of the SPIFI dewar, and shares radiation shields, but the two dewars maintain their independent cryogenic systems.

SPIFI uses a 5 × 5 rectangular array of Goddard monolithic silicon bolometers. The bolometers have excellent performance with detector noise equivalent powers (DNEPs) better than 5×10^{-18} W Hz$^{-1/2}$ at 70 mK and zero background [15]. This is a few times smaller than the noise from the thermal background radiation referred to the detector so that SPIFI should be background limited for most situations.

3. SENSITIVITY

The noise equivalent flux, NEF, of a background limited model spectrometer consisting of warm optical elements at temperature T, with transmission, t_w and emissivity, ϵ, cold optical elements with transmission t_c (emissivity 0), in terms of the detector quantum efficiency, η is [16]:

$$NEF = \frac{h\nu}{A\eta t_c t_w} \left[\frac{2^4 A\Omega}{\lambda^2} \Delta\nu \epsilon \eta t_c \bar{n}(1 + \epsilon \eta t_c \bar{n}) \right]^{1/2} Wcm^{-2}Hz^{-1/2}$$

where h is Planck's constant, ν is the frequency, $A\Omega/\lambda^2$ is the number of photon modes, and $\bar{n}$ is the mode occupation number = $1/(exp(h\nu/kT)-1)$. The FPI instrumental profile is nearly Lorentzian, so that the equivalent bandwidth reaching the detector, $\Delta\nu$, is $\pi/2$ times the resolution bandwidth, $\Delta\nu = \pi/2 \cdot \nu/R$, (R = $\lambda/\Delta\lambda$). The various factors of 2 are due to (1) detecting both polarizations of light, (2) expressing the result in Hz$^{-1/2}$, (3) chopping, and (4) nodding (position switching).

For SPIFI on AST/RO (A = 22,700 cm^2), t_w through the telescope to the source is $\sim 60\%$ ($t_{sky} \sim 75\%$ [17]), $\epsilon \sim 40\%$, T ~ 220 K, $\eta \sim 50\%$, and $t_c \sim 50\%$. Evaluating constants, and expressing the wavelength in microns:

$$NEF = 1.8 \text{ E-15 } \lambda(\mu m)^{-3/2} \cdot [\bar{n}(1+0.089\bar{n})/R]^{1/2} W cm^{-2} Hz^{-1/2}$$

The solid angle appropriate for Gaussian beams is: $\Omega = \pi \cdot (1.22 \lambda/2D)^2 \cdot (1/\ln(2))$. Table 2 lists the NEF for SPIFI-AST/RO, the noise equivalent intensity NEI =

10–30 MICRON MAPS OF THE CENTRAL 5 PARSECS OF THE GALAXY: HEATING OF THE CAVITY AND NEUTRAL GAS DISK

C. M. TELESCO[1]

Space Science Laboratory, NASA/Marshall Space Flight Center; and Department of Astronomy, University of Florida,
SSRB 211 Gainesville, FL 32611;[2] telesco@astro.ufl.edu

J. A. DAVIDSON[1]

SETI Institute and NASA/Ames Research Center, MS 245-6, Moffett Field, CA 94035; davidson@cma.arc.nasa.gov

AND

M. W. WERNER[1]

Jet Propulsion Laboratory, MS 233-303, 4800 Oak Grove Drive, Pasadena, CA 91109; michael.w.werner@jpl.nasa.gov

ABSTRACT

We present 10, 20, and 30 μm maps of the central $60'' \times 90''$ (R.A. $\times$ decl.) of the Galaxy made at approximately $4''$ resolution with the NASA/Marshall Space Flight Center bolometer array. The maps span 2.5×3.8 pc centered near Sgr A IRS 1 and are the first to show the thermal emission from dust particles in both the ionized cavity and the neutral-gas ring with high sensitivity and an angular resolution as good as several arcseconds. In addition to warm dust associated with previously identified filaments in the central $40''$, these maps show the detailed distribution of dust along the entire Western Arc of ionized gas at the inner edge of the neutral-gas ring. A prominent tongue of high 30 μm optical depth extends from the northern part of the ring into the cavity near IRS 1, nearly bisecting the cavity; since we detect warm dust in this 30 μm-emitting feature, which we call the Northern Intruder, it must be heated by radiation emitted in the cavity, thus confirming previous speculations based on far-infrared and O^0 observations that substantial neutral material protrudes into the cavity and may constitute infalling matter that fuels the central activity. We show that *all* the major ionized filaments (the Western Arc, the Bar, the Northern Arm, and the Eastern Arm) are ionization fronts at the interfaces between low- and high-density regions, as had been previously demonstrated convincingly only for the Western Arc. The locations of these ionization fronts are consistent with the dominant UV heating and ionizing sources being centrally located in the cavity. The derived dust temperatures strongly support this picture: they decrease away from the region of IRS 1 and Sgr A*, and they drop abruptly where the gas density increases at the ring. We determine that the total ultraviolet luminosity emitted by the central cluster and required to heat the dust to the inferred temperatures is $1.7 \pm 0.5 \times 10^7 L_\odot$, which agrees with our derived infrared luminosity. Half of this ultraviolet luminosity is absorbed by dust in the cavity, and more than 40% of the ultraviolet radiation that propagates to the edge of the cavity is absorbed by dust in the neutral-gas ring.

Subject headings: dust, extinction — Galaxy: center — infrared: ISM: continuum

1. INTRODUCTION

The Infrared appearance of the central 5 pc of the Galaxy at $\lambda > 50$ μm is dominated by two lobes separated along the Galactic plane by several parsecs. In contrast, the infrared continuum at shorter wavelengths is much more concentrated to the nuclear core (Harvey, Campbell, & Hoffmann 1976; Rieke, Telesco, & Harper 1978; Becklin, Gatley, & Werner 1982; Davidson et al. 1992). All of the infrared continuum radiation observed longward of a few microns is emitted by heated dust particles, and so this striking dichotomy is thought to represent a ring of cool dust encircling a central, lower density cavity filled with hotter dust (Becklin et al. 1982). This model, which has been confirmed in detail, has been remarkably useful for the interpretation of the broad range of observations of the Galactic center (see, e.g., Jackson et al. 1993 for an overview).

Infrared, submillimeter, and radio spectroscopy of atoms and molecules shows that the cool ring is composed primarily

of neutral gas, that it is rotating and clumpy, and that it extends from about 1.5 pc at its inner edge to at least 7 pc (e.g., Güsten et al. 1987; Jackson et al. 1993). The ring is inclined about 65° to the line of sight (e.g., Lacy, Achtermann, & Serabyn 1991). An intense arc of ionized gas, detected in radio continuum and Ne$^+$ line emission, coincides with the ring to the west and southwest of the nucleus and almost certainly represents ionization of the inner edge of the ring by UV radiation from the cluster of sources located in the cavity (Serabyn & Lacy 1985). It has been speculated that other diffuse and filamentary ionized features in the cavity may have a similar origin. Despite the first impression that the cavity is filled only with ionized gas, it probably also contains substantial neutral gas (Davidson et al. 1992; Jackson et al. 1993; this paper).

The cavity contains numerous compact sources detected from 1 to 30 μm. Many are apparently internally heated (e.g., Smith, Aitken, & Roche 1990; Gezari, Dwek, & Varosi 1993), and there is strong evidence that at least a dozen of them are blue supergiants undergoing strong mass loss (Rieke, Rieke, & Paul 1989; Allen, Hyland, & Hillier 1990; Krabbe et al. 1991). The relative roles of those stars and the putative black hole coincident with the bright nonthermal radio source Sgr A* in

heating the dust and generating the luminosity of the Galactic center are unknown, but simple assumptions about the stars indicate that they may be sufficiently luminous to provide all of the central far-infrared luminosity (e.g., Allen et al. 1990; Krabbe et al. 1991). These rare blue supergiants probably represent only a small fraction of a large number of OB stars, most of which are much less luminous than the supergiants, that formed within the last $\sim 10^6$ yr in the central few parsecs of the Galaxy (Rieke et al. 1989; Krabbe et al. 1991).

The appearance of the Galactic center is determined largely by the spatial distributions of the matter and radiation and the luminosity of the heating sources. Infrared-emitting dust is a useful probe of these properties because it permeates both ionized and neutral regions in rough proportion to the gas densities there, and its temperature reflects the value of the local radiation field. In this paper we present 10, 20, and 30 μm maps that are the first to show the thermal emission from dust particles in both the cavity *and* the ring with high sensitivity and an angular resolution as good as several arcseconds. Almost all previous mid-infrared (5–30 μm) maps of the dust, including two at approximately 30 μm (Rieke et al. 1978; Gatley, Becklin, & Telesco, published in Gatley 1982), spanned only the cavity region. An exception is the 20″ resolution, 10 μm map by Rieke et al. (1978) showing faint emission from the ring region southwest of the cavity. All other maps showing the emission from dust in both the cavity and the ring are based on airborne far-infrared observations with angular resolutions no better than approximately 20″ (Harvey et al. 1976; Rieke et al. 1978; Becklin et al. 1982; Davidson et al. 1992). Our maps provide new information about the structure and energetics of the central 5 pc of the Galaxy, permitting in particular a unique appraisal of the distributions of dust density and temperature and of the total luminosity of the heating sources. In this paper we assume a distance of 8.5 kpc to the Galactic center.

2. OBSERVATIONS AND PROCEDURE

We mapped the Galactic center on UT 1992 May 3–5 using the Marshall Space Flight Center bolometer array (Big Mac) at the NASA Infrared Telescope Facility (IRTF). Maps were made at 10.8 μm ($\Delta\lambda = 5.3$ μm, FWHM), 19.2 μm ($\Delta\lambda = 5.2$ μm), and 30 μm ($\Delta\lambda = 5$ μm). The array consists of 20 square pixels arranged in a 5 × 4 (R.A. × decl.) configuration with only a small dead space between adjacent pixels. The field of view (FWHM) of each pixel was 3″9 × 4″2. (Although each pixel is intrinsically square, the pixel profiles are smeared by the $\sim$10 Hz oscillation, or "chopping," of the telescope secondary mirror.) The pixel center-to-center separation was 4″5, and the full array subtended 23″ × 18″. The separation between the object and sky-reference positions was 75″ along P.A. = 123° (i.e., perpendicular to the Galactic plane) for the large-scale map at 19.2 μm and 90″ in right ascension for all other maps (see below). We saw evidence for source flux in the reference beam when we tried to extend our maps to more than about 40″ to the northwest and southeast from IRS 1, and so data from those regions were discarded; airborne observations at 30–50 μm (Becklin et al. 1982; Davidson et al. 1992) imply that the mid-infrared fluxes are concentrated enough in the Sgr A region that the 10–30 μm maps we present should not be affected by flux in the reference beams.

The star α Sco was used for absolute flux calibration at 10.8 and 19.2 μm, assuming flux densities of 2291 and 834 Jy, respectively, based on interpolation from values in the IRTF

list of standard stars. The 30 μm filter has a small spectral leak at $\lambda < 5$ μm. Therefore, stellar standards are inappropriate for calibrating this passband, but experience shows that accurate photometry can be obtained with this filter as long as the program objects and standards have relatively "cool" spectral energy distributions; i.e., they must be relatively deficient in short-wavelength flux, which applies to the Galactic center region discussed here. To calibrate photometrically our 30 μm maps, obtained on UT 1992 May 4, we observed the Galilean satellite Callisto on the same night, determining that its 10.8 to 19.2 μm color temperature was 164 K; we then took the 30 μm flux level of Callisto to be that of a 164 K blackbody normalized to the 10.8 and 19.2 μm flux densities. We estimate the uncertainties in the absolute calibration to be 7%, 10%, and 20% at 10.8, 19.2, and 30 μm, respectively. Air-mass corrections at each wavelength were determined by frequent monitoring of the flux from the bright Galactic center source IRS 1. All photometry presented in this paper has been corrected for the nonzero widths of the filter passbands assuming the average spectral energy distribution of the Galactic center region.

Two maps were made at each of the three wavelengths 10.8, 19.2, and 30 μm: a large-scale mosaic composed of contiguous array settings spanning the central 60″ × 90″ of Sgr A, and a smaller, fully (Nyquist) sampled map lying within the boundaries of the larger one but concentrated primarily to the region in the southwest quadrant. The two maps at each wavelength consist of independent data. The large-scale maps are shown in Figure 1, and the fully sampled maps are shown in Figure 2. The contour intervals are logarithmic. To improve the signal-to-noise ratio in the lobe region of the fully sampled maps, the flux distributions there were smoothed with a 4″5 (1 pixel size) boxcar. The observational procedure consisted of maximizing the signal detected in a central pixel of the array on the Galactic center source IRS 1 at 10.8 μm, after which the filter passband was changed and the telescope was offset as desired. This peaking procedure is unambiguous, because IRS 1, indicated by a cross in the figures, is compact and substantially brighter at 10.8 μm than any other source in this region (see, e.g., Becklin & Neugebauer 1975). We estimate the uncertainty in the peaking and offsetting procedures to be $\pm 1''$, which also characterizes the uncertainty in the relative positions of the different maps. The 1950 positions assumed in this paper for IRS 1 and Sgr A* are $17^h42^m29^s74$, $-28°59'18″2$ and $17^h42^m29^s32$, $-28°59'18″4$, respectively (see Smith et al. 1990; Eckart et al. 1992, and references therein).

3. RESULTS

3.1. The Mid-Infrared Maps

The large-scale maps in Figure 1 span about 60″ × 90″ (R.A. × decl.), which corresponds to 2.5 pc × 3.8 pc. The maps at all three wavelengths show the bright emission centered near IRS 1 and Sgr A* associated with the central cluster and a prominent ridge or lobe of emission (the "southwest lobe") extending about 50″ to the southwest of IRS 1. In the regions of overlap, the fully sampled maps shown in Figure 2 agree well with the large-scale maps. The fully sampled map at 10.8 μm includes only the southwest lobe, whereas the 19.2 and 30 μm maps span the southwest lobe and much of the region around IRS 1. Many of the prominent compact sources detected at 10 μm (e.g., Rieke & Low 1973; Becklin & Neugebauer 1975; Gezari et al. 1987) are indicated in the fully
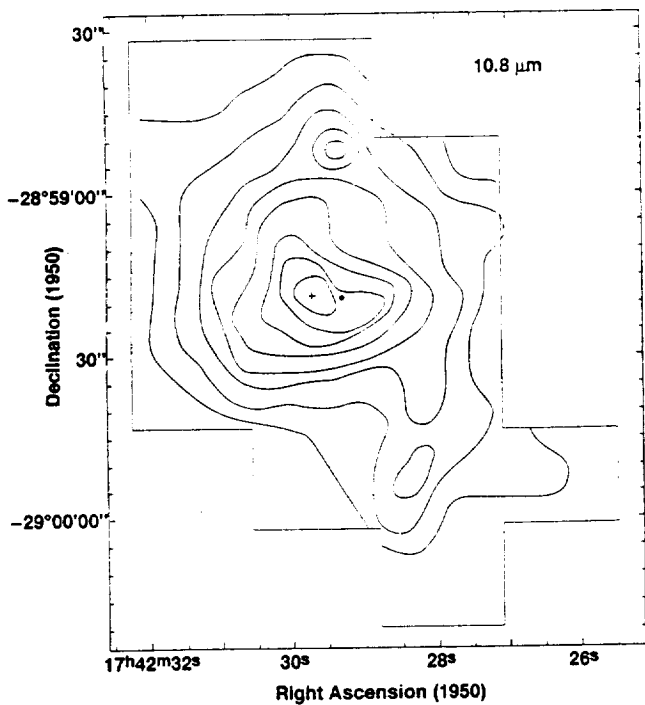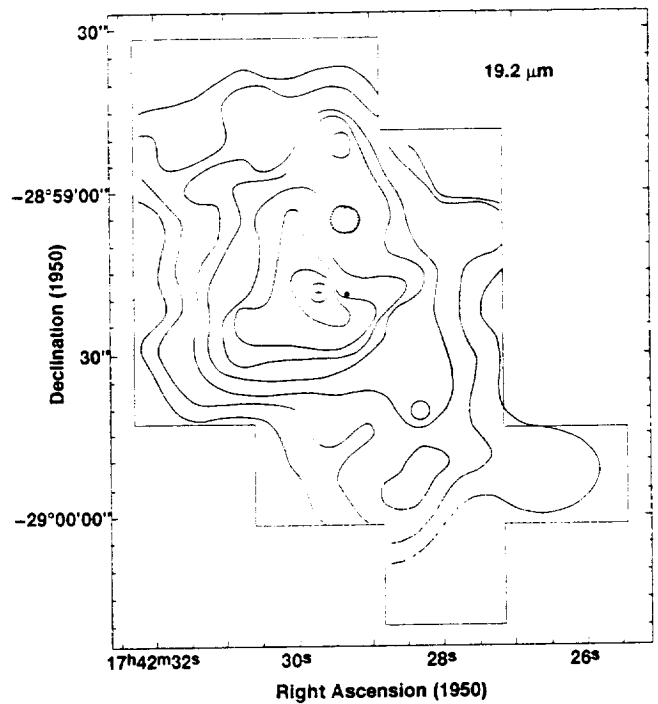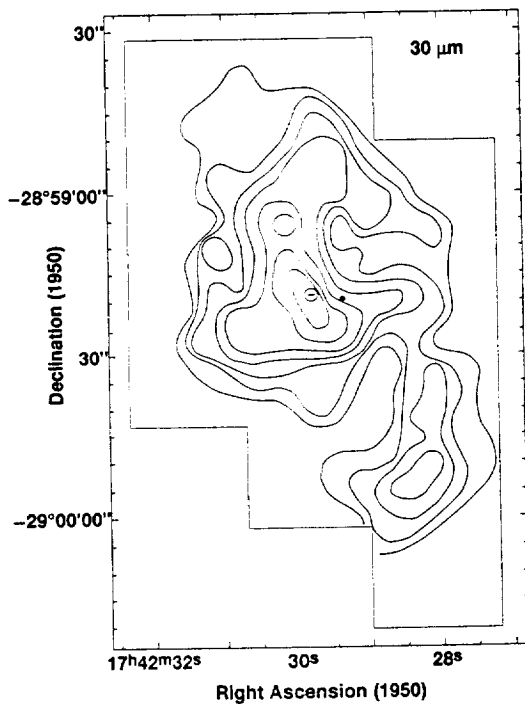
FIG. 1a

10.8 μm

FIG. 1b
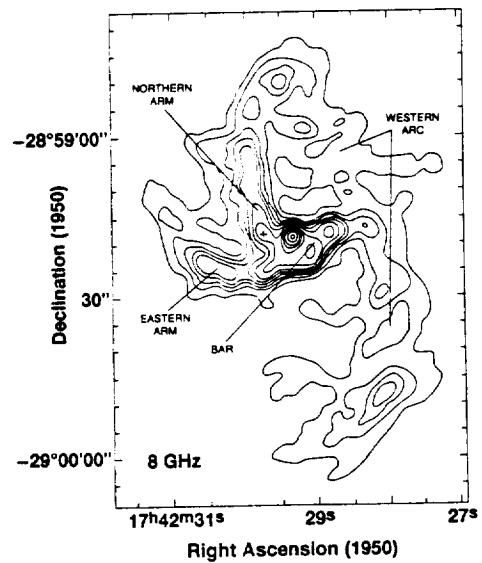
19.2 μm

FIG. 1c

30 μm

FIG. 1d

8 GHz

NORTHERN ARM
WESTERN ARC
EASTERN ARM
BAR

FIG. 1.—(a) Large-scale map of the Galactic center at 10.8 μm. The cross and the filled circle indicate the position of IRS 1 and Sgr A*, respectively. Contour levels (Jy pixel^{-1}) are logarithmically spaced at 0.5, 1, 2, 4, 8, 16, 32, and 64, with an uncertainty (standard deviation of the measured mean value) of 0.1. The peak intensity (at IRS 1) is 116 Jy pixel^{-1}. (b) Large-scale map at 19.2 μm. Contour levels (Jy pixel^{-1}) are logarithmicaly spaced at 2, 4, 8, 16, 32, 64, 128, and 256, with an uncertainty of 0.5. The peak intensity is 274 Jy pixel^{-1}. (c) Large-scale map at 30 μm. Contour levels (Jy pixel^{-1}) are logarithmically spaced at 28, 39, 55, 77, 108, 150, 210, and 295, with an uncertainty of 10. The peak intensity is 296 Jy pixel^{-1}. (d) Map of 8 GHz continuum by Roberts et al. (1991) made with a resolution of 2″.4. The brightest point is the nonthermal source Sgr A*. Contour levels (mJy beam^{-1}) are 30, 50, 70, 90, 110, 150, 200, 300, 500, and 700, with an rms uncertainty of 0.4. (e) The cavity and ring regions, defined by thin lines, overlaid on an outline of the 30 μm map (thick lines). The figure indicates the total observed flux densities from each region.
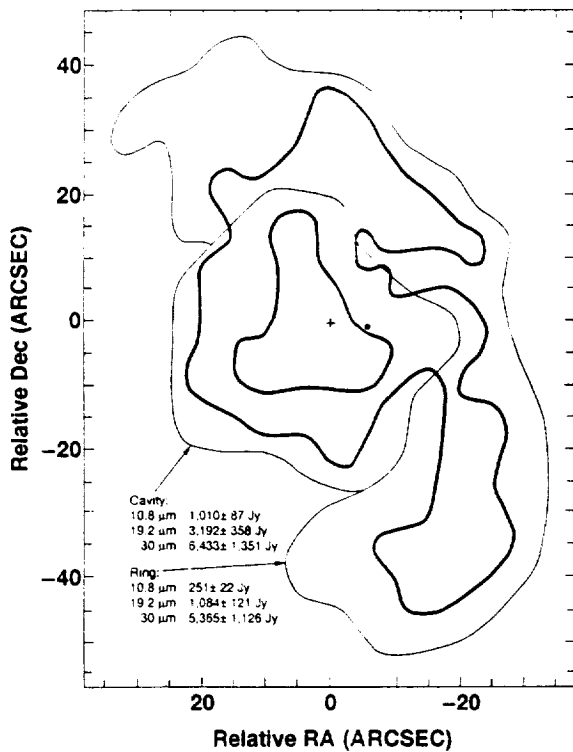
FIG. 1e

sampled 19.2 μm map in Figure 2b. Discrete sources at 19.2 and 30 μm coincide within 1″ with IRS 1, 3, and 4, and the contours extend suggestively toward IRS 2, 5, 6, and 10. Nearly all of the 10 μm sources seem to have counterparts in the fully sampled 19.2 and 30 μm maps. However, the study of these discrete sources in the central complex was not the primary goal of our program, and so the observational strategy, angular resolution, and subsequent analysis have not been optimized to illuminate their properties.

In Figure 1d we show the 8.3 GHz continuum emission observed with 2″4 resolution (Roberts et al. 1991), which traces primarily the distribution of ionized gas, although the brightest peak is the nonthermal source Sgr A*. Generally accepted terminology, as summarized by Lacy et al. (1991) is also indicated. The impression is that the mid-infrared emission is distributed like the ionized gas. All the major radio features (the Northern Arm, the Bar, the Eastern Arm, and the Western Arc) have counterparts in the infrared maps, as previously noted at 10 μm (e.g., Gezari & Yusef-Zadeh 1990) and 30 μm (Gatley et al., published in Gatley 1982) for regions near the central cluster. The similarity of the *large-scale* morphologies of ionized gas and mid-infrared–emitting dust, shown here for the first time, is striking, especially at 30 μm. For example, the southwest infrared lobe corresponds to the southern extension of the Western Arc, of which the entire length northward to IRS 8 is well defined at 30 μm. Our maps show clearly that the southwest lobe consists of two dominant emission regions of comparable surface brightness. Comparison of our maps to the radio continuum emission reveals that the northern of the two dominant mid-infrared sources in the southwest lobe coincides with an extended radio peak, whereas the centroid of the southern mid-infrared source is offset about 4″ to the southeast along the arc from the nearest radio peak that is also the brightest radio source in the southwest lobe. We also note that the lowest

contour in the southwest lobe bulges noticeably to the west at 10.8 and 19.2 μm but not obviously at 30 μm. This structure is real (§ 6) but probably not evident at 30 μm because the 30 μm sensitivity is much lower than that at the shorter wavelengths (see Figs. 1 and 2).

Although the mid-infrared and radio morphologies are very similar, there are important differences. In Figure 3a we show the mid-infrared and 8 GHz flux densities along a right ascension scan through the southwest lobe indicated by the horizontal line in Fig. 2b; the scan is roughly perpendicular to the molecular ring in this region and cuts across the boundary between the cavity and ring. The infrared data are from the fully sampled maps (Fig. 2), and the radio data were read off the 8 GHz map presented in Figure 1d. The positions of maximum 10.8 μm and 8 GHz fluxes coincide, but with increasing wavelength there is a progressive shift of the peak emission away from the cavity. The warmest dust, which dominates the 10.8 μm emission, must be mixed with the ridge of ionized gas, and the somewhat cooler dust, which dominates the longer wavelength emission, is located to the west and southwest, where the densities are higher. Thus, we see clear evidence for a temperature gradient in the dust across the cavity-ring boundary. The wavelength dependence of the flux seen in this scan is part of a large-scale pattern reflecting the distribution of matter and radiation throughout Sgr A, which we explore further below.

The flux densities integrated within the lowest contours of our large-scale maps are 1260 ± 110 Jy at 10.8 μm, 4280 ± 480 Jy at 19.2 μm, and 11,800 ± 2480 Jy at 30 μm. The uncertainties include those in absolute calibration and data reduction. For the purposes of determining the cavity and ring flux densities separately, we indicate the two regions in Figure 1e on an outline of the 30 μm map. This separation into cavity and ring regions is somewhat ambiguous but consistent both with the usual terminology used for Sgr A and the distribution of optical depth discussed below. The cavity region so defined is about 40″ (1.7 pc) in diameter. The flux densities determined for each region are listed in Figure 1e. We see that the ring contributes about 20% of the total observed flux density at 10.8 μm, 25% at 19.2 μm, and 45% at 30 μm. To determine the emitted luminosities, fairly large corrections for interstellar extinction must be applied to these values (§ 3.2). Note that integration over a 30″ diameter circular region centered on IRS 1 yields a 30 μm flux density of 4200 Jy, which agrees well with the value observed by Becklin et al. (1982) in a 30″ beam.

Because of the uniqueness of our 30 μm observations, it is worthwhile to see what limits they place on the flux density of the unusual source Sgr A* (see Zylka et al. 1994 and Gezari et al. 1994 for discussions of this source and its luminosity). We consider the original grid of data from which we constructed the fully sampled 30 μm map presented in Figure 2c. While observing this grid, a pixel of the detector array was centered at a position 0″8 from Sgr A*, so that the source was located fortuitously near the most sensitive part of the pixel. The 30 μm flux density detected in that pixel is 69 ± 10 Jy, which is precisely consistent with the smooth contours shown in Figure 2c at the location of Sgr A* (*filled circle*). Therefore, the contours at that location exhibit no structure that we can attribute to emission from a point source. Roughly then, we can assign a 2 σ upper limit of 20 Jy to the 30 μm flux density from Sgr A*. Although unique, this limit is not a particularly tight constraint on the spectrum of Sgr A* (see Zylka et al. 1994). From a similar analysis of our fully sampled 19.2 μm map (Fig. 2b),
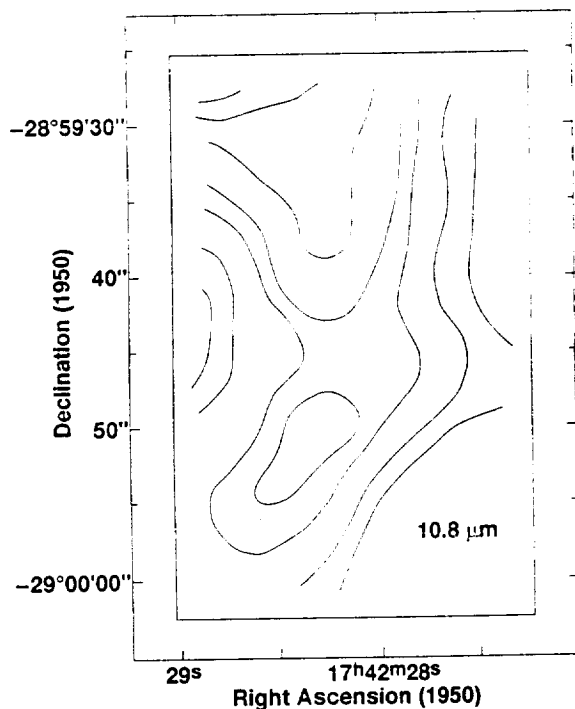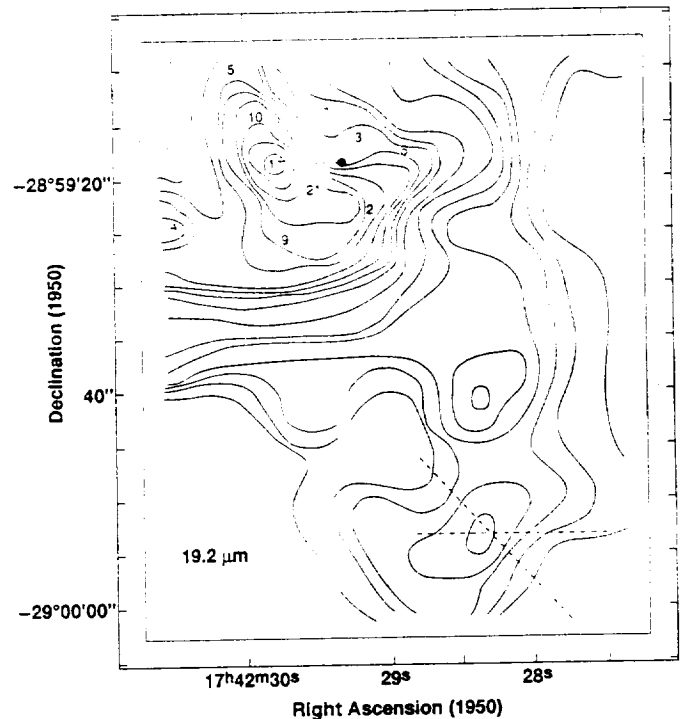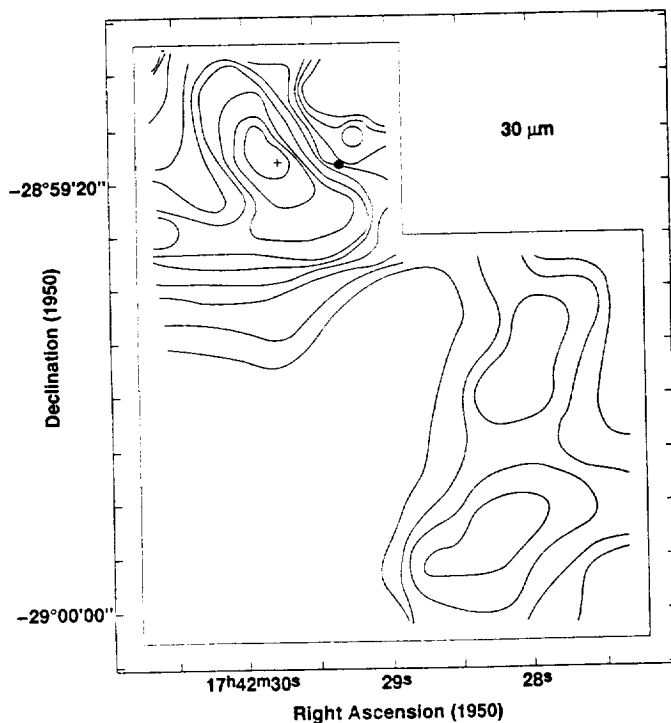
Fig. 2a

Fig. 2b

Fig. 2c

FIG. 2.—Fully sampled mid-infrared maps, with logarithmically spaced contours. The cross and filled circle indicate IRS 1 and Sgr A*, respectively. (a) Map at 10.8 μm of the southwest lobe region. Contour levels (Jy pixel⁻¹) are 0.9, 1.2, 1.5, 2.0, 2.6, 3.4, and 4.4, with an uncertainty of 0.1. (b) Map at 19.2 μm of cluster and southwest lobe regions. Contour levels (Jy pixel⁻¹) are 4, 5, 7, 9, 12, 15, 20, 26, 33, 43, 56, 74, 96, 124, 161, 209, and 271, with an uncertainty of 0.5 in the cluster region and 0.3 in the southwest lobe. The peak intensity is 274 Jy pixel⁻¹. The locations of the most prominent 10 μm cluster sources are

we derive an upper limit of 1.4 Jy, which is comparable to the more carefully derived 20 μm limit obtained by Gezari et al. (1994) from images made with much higher angular resolution than ours.

3.2. Extinction Corrections

Much of the discussion in this paper will focus on the interpretation of the infrared colors in terms of the temperatures and optical depths of the Galactic center dust. For this interpretation to be reliable, accurate account must be taken of the large interstellar extinction, corresponding to $A_V \approx 30$, which significantly modifies the observed spectral energy distribution of the Galactic Center even at these long wavelengths (e.g., Gezari et al. 1993; Zylka et al. 1994). The extinction correction is particularly important for determining the emitted luminosity of the Sgr A cavity, for which the spectral energy distribution peaks in the mid-infrared and is attenuated by nearly an order of magnitude by interstellar absorption. The extinction in our mid-infrared passbands consists of an absorption continuum and the broad silicate absorption features centered near 9.7 and 19 μm (see, e.g., McCarthy et al. 1980; Mathis 1990). Explicit corrections must be made for the absorption in these silicate features; in the mid-infrared it is not sufficient to assume, as is often done at longer wavelengths (e.g., Gatley et al. 1977), that the absorption follows a power law (i.e., $Q_v \propto v^{1-2}$). Using 5" resolution observations, Smith et al. (1990) inferred that the 9.7 μm feature seen in absorption toward Sgr A is actually composed of a deep absorption feature of roughly

indicated by their IRS numbers. The dashed lines in the southwest lobe correspond to the scan paths discussed in Fig. 3. (c) Map at 30 μm of the cluster and southwest lobe regions. Contour levels (Jy pixel⁻¹) are 34, 44, 58, 74, 100, 126, 163, 212, and 276, with an uncertainty of 10 Jy in the cluster region and 5 Jy in the southwest lobe. The peak intensity is 290 Jy pixel⁻¹.
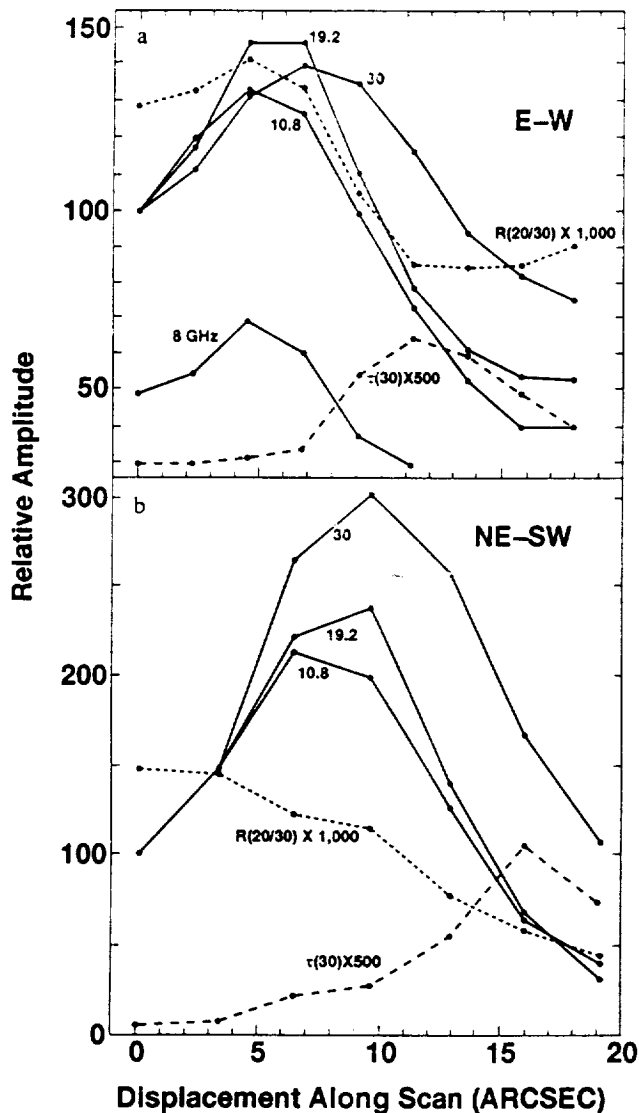
Displacement Along Scan (ARCSEC)

FIG. 3.—Scans through the southwest lobe showing the distributions of 10.8, 19.2, and 30 μm flux densities, color $R(20/30)$, and optical depth $\tau(30)$. The scan paths are constructed from data in the fully sampled maps and are indicated by the dashed lines in Fig. 2b. Also shown in (a) is a scan of the 8 GHz continuum, as extracted from the map of Roberts et al. (1991). The flux densities are normalized to the value 100 at 0″ displacement, $R(20/30)$ and $\tau(30)$ are normalized as indicated in the figure, and the amplitude for the 8 GHz scan is in units of mJy beam^{-1}.

uniform depth $\tau(9.7) = 3.6 \pm 0.3$ across the source and an emission feature with a strength that depends more strongly on position. McCarthy et al. (1980) observed the 16–30 μm spectrum of the central 30″ of Sgr A and detected a broad silicate absorption feature centered near 19 μm. Their fit of the spectrum, assuming it results from hot dust in Sgr A and cool intervening dust, implies $\tau(19) \approx 2.1$ at the center of the feature for the cool (interstellar) dust, a value which agrees with that determined more recently by Chan et al. (1995). McCarthy et al. (1980) assumed that the silicate emissivity is similar to that deduced for the circumstellar dust of oxygen-rich stars.

Taking $\tau(19) = 2.1$ at the center of the feature and assuming that the emissivity varies with wavelength as indicated by McCarthy et al. (1980), we infer an optical depth, averaged across our 19.2 μm passband, of $\tau_{ISM}(19.2) = 1.9$, which corre-

sponds to the absorption by the interstellar dust located between us and the Galactic center; thus, we are detecting only 15% of the flux emitted by Sgr A even at this long wavelength. Likewise, we infer $\tau_{ISM}(30) = 0.8$ (see McCarthy et al., Fig. 3), which is consistent with the value of 0.5 estimated by Herter et al. (1984) at 34 μm; we detect about 45% of the 30 μm flux emerging from the Sgr A region. To determine the extinction averaged across our broad 10.8 μm passband, we refer to the extinction curve presented by Mathis (1990), who used silicate absorption profiles from Draine & Lee (1984). We then estimate that the average broadband absorption at 10.8 μm is 1.6 times that across the 19.2 μm band, with the result that $\tau_{ISM}(10.8) \approx 3.0$.

In this paper we will need to use estimated extinction properties of dust throughout the spectrum. The UV properties of the dust, especially in the Sgr A region, are highly uncertain. Here we consider two different extinction curves summarized by Mathis (1990): one for "diffuse dust," for which the ratio R_V of total-to-selective extinction is typically 3.1, and one for "outer-cloud dust," for which $R_V \approx 5.0$. Because of the proximity of the ionized cavity to the molecular ring, it seems reasonable that these two extinction relations roughly span those applicable to Sgr A, although the abundances and dust properties there may be unusual (e.g., McCarthy et al. 1980; Herter et al. 1989). The key distinction between these two relationships is that the UV extinction at 0.12 μm for the outer-cloud dust is about a factor of 2 less than it is for the diffuse dust. We have extrapolated the extinction curve for the outer-cloud dust to $\lambda < 0.12$ μm by assuming that it is identical in shape to that for the diffuse dust. Note that the extinction curves summarized by Mathis (1990) represent both absorption and scattering of radiation by dust. Although essentially negligible in the infrared, scattering is significant in the UV (see, e.g., Draine & Lee 1984). Our use of these extinction curves assumes, in effect, that scattering of UV photons is equivalent to their absorption, which seems justified by the fact that multiple scattering of UV photons by dust in the cavity substantially increases their chances of being absorbed there.

3.3. Mid-Infrared Colors, Dust Temperatures, and Optical Depths

For optically thin emission, the flux density determined from our broadband observations is $F_\nu = \tau \Omega B_\nu(T_d) \exp(-\tau_{ISM})$, where Ω (3.9×10^{-10} sr) is the pixel size, $B_\nu(T_d)$ is the Planck spectral intensity, τ is the optical depth of emitting dust in Sgr A, and τ_{ISM} is the optical depth of the intervening cool dust referred to in the last section. The color $R(20/30)$ is defined to be the ratio of the flux densities: $R(20/30) \equiv F_\nu(19.2\ \mu m)/F_\nu(30\ \mu m)$. We determine the temperature T_d of the mid-infrared–emitting dust (or, more precisely, the 20–30 μm-emitting dust) from the relation:

$$R\left(\frac{20}{30}\right) = \frac{\tau(19.2)}{\tau(30)} \times \frac{B_\nu(19.2,\ T_d)}{B_\nu(30,\ T_d)}$$

$$\times \exp\left[-\tau_{ISM}(19.2) + \tau_{ISM}(30)\right],$$

where, based on comments in the previous paragraph, $\tau(19.2)/\tau(30) = 2.4$, and the exponential absorption term equals 0.33. Figure 4 presents the temperature distributions determined from our large-scale and fully sampled maps at those positions where the values of $R(20/30)$ have a statistical significance greater than 3. The correspondence between $R(20/30)$ and T_d is given in the figure caption. Knowing the dust temperature and
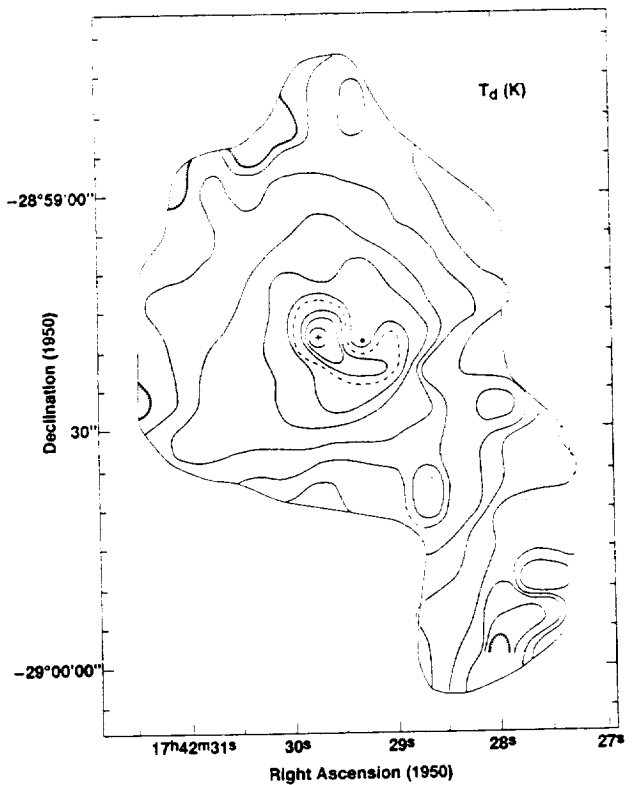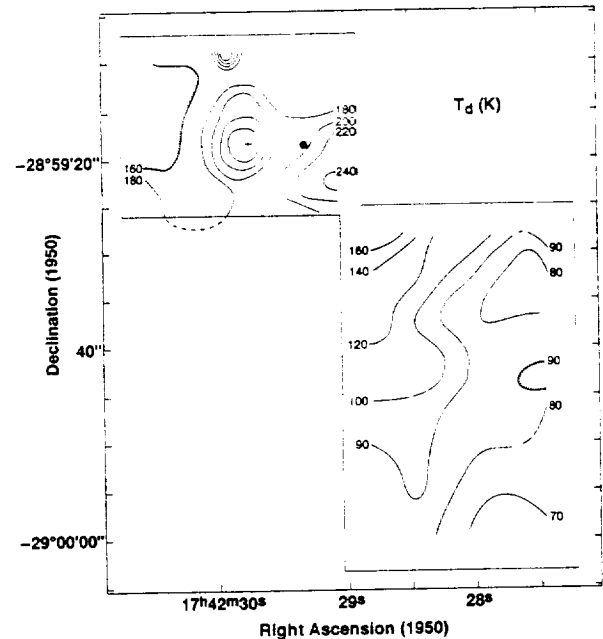
FIG. 4a

FIG. 4b

FIG. 4.—The dust temperature T_d derived from the 19.2 and 30 μm maps after correction for interstellar extinction. (a) Distribution based on large-scale maps. The contour levels are 70, 75, 80, 85, 90, 100, 120, 140, 160, 180, 190 (dashed), 200, 220, and 240 K, where the highest temperature corresponds to the small circular contour centered on IRS 1 (cross). (b) Distribution based on the fully sampled maps. Most contours are labeled by the dust temperature in kelvins; the three unlabeled contours at IRS 1 (cross) correspond to 200, 220, and 240 K. Using the format $T_d(R)$, the correspondence between T_d and $R(20/30)$ is 60(0.034), 70(0.062), 80(0.10), 90(0.15), 100(0.20), 120(0.31), 140(0.43), 160(0.52), 180(0.63), 200(0.73), 220(0.81), and 240(0.89).

the emitted flux density at each position, we can also derive the optical depth $\tau(30)$, shown in Figure 5, of emitting dust along the line of sight.

We emphasize that the values of the optical depth and temperature derived here are average values for each line of sight. Both quantities are weighted by the grain properties in different ways, and, since the properties vary greatly across the Galactic center region, the maps will be distorted or inaccurate to some degree. Although only detailed modeling of the region can define the precise nature of this distortion, our approximate analysis should permit an examination of the region's key features. We also note that Chan et al. (1995) have recently reported the detection of a broad 30 μm emission feature in the Sgr A region. This feature, which resembles that found previously in carbon-rich evolved stars, probably affects quantities we derive from the broadband 30 μm fluxes. An assessment of these effects awaits the availability of more complete characterization of the feature.

4. THE DISTRIBUTION OF MASS AND IONIZATION FRONTS

4.1. Relationship of Mid-Infrared–Emitting Dust to Cavity and Ring

The optical depth determined from our mid-infrared maps corresponds to the distribution of column density of warm dust in the central 5 pc of the Galaxy. The angular resolution is 5 to 10 times better than for any previous maps of the dust spanning this region. The global distribution of $\tau(30)$ is shown

in Figure 5a. We see an irregular, roughly hourglass-shaped region (central dashed contour) of low optical depth surrounded by one of higher optical depth with values ranging from 0.01 in the northeast to 0.2 in the southwest. In Figures 6a and 6b we compare the global distribution of $\tau(30)$ to the 8 GHz continuum (Roberts et al. 1991), which, except for the brightest point (Sgr A*), is thermal bremsstrahlung, and to the distribution of HCN (Wright et al. published in Güsten 1987; see also Güsten et al. 1987). The brightest ionized gas coincides with the regions of lowest 30 μm optical depth, whereas the inner part of the molecular ring coincides with the western ridge of high optical depth. These global mid-infrared properties are therefore in accord with the widely accepted picture of a central cavity encircled by a dense ring.

The column density of mid-infrared–emitting dust across Sgr A spans nearly two orders of magnitude. Combining the gas-to-color excess ratio for either the ρ Oph region or the diffuse interstellar medium (see Savage & Mathis 1979) with the extinction curves of outer-cloud dust or diffuse dust, respectively, we derive the relation $N(H) \approx 4 \times 10^{23}\tau(30)$, where $N(H)$ is the column density (number per square centimeter) of hydrogen nuclei averaged over our 4″ beam. Assuming that the gas-to-dust ratio is constant throughout the Galactic center, we infer that the hydrogen column density varies from about 10^{21} cm^{-2} toward the cavity to nearly 10^{23} cm^{-2} in the southwest lobe at the location of the brightest HCN clump. For a cavity diameter of 2 pc, the average gas density in the ionized region away from major filaments is
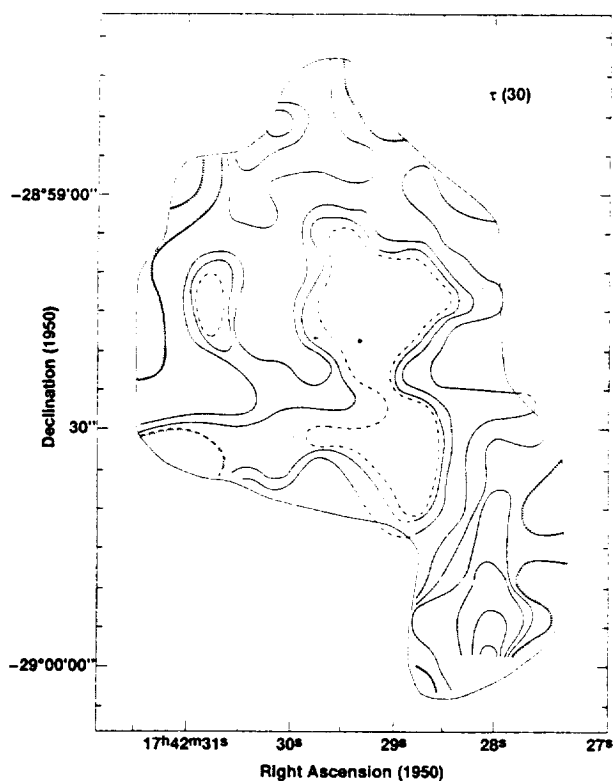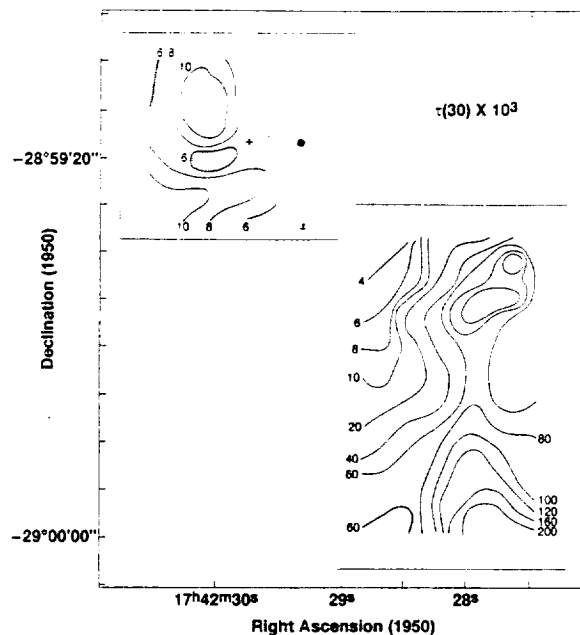
FIG. 5a

FIG. 5b

FIG. 5.—The optical depth $\tau(30)$ of dust emitting at 30 μm. (a) Distribution based on data from the large-scale maps. The contour levels, in units of 10^{-3}, are 6 (dashed lines), 8, 10, 20, 40, 60, 80, 150, and 200. Outer contours with tick marks indicate lower optical depth in the region on the side with the ticks; in units of 10^{-3}, the tick-marked contours to the north and northeast have the value 10, that to the southeast has the value 6, and those to the southwest have the value 40. The roughly hourglass-shaped region enclosed by the central dashed contour is the most obvious part of the cavity; although not indicated explicitly, optical depths as low as 0.003 were found for the central $\sim 5''$ diameter regions of the upper and lower parts of the hourglass. (b) Distribution based on data from the fully sampled maps. Contours are labeled by the optical depth multiplied by 10^3.

about 300 cm^{-2}. If the densest dust concentration in the southwest lobe is 0.5 pc thick, then the average gas density there is about 5×10^4 cm^{-3}, whereas the average densities in other, possibly more typical, parts of the ring (e.g., the northwest) are of the order of 5×10^3 cm^{-3}. However, detailed modeling of the HCN excitation in the ring by Jackson et al. (1993) implies that the actual gas densities are two to three orders of magnitude larger than these average values. Therefore, the volume filling factor of the dense gas and mid-infrared dust in the ring must be only a few percent or less, as also concluded by Jackson et al. (1993) using HCN column densities.

4.2. The Northern Intruder: Inflow into the Cavity

Although the cooler dust emitting at 100 μm is concentrated in two lobes that are coincident with the northeast and southwest parts of the molecular ring (Becklin et al. 1982; Davidson et al. 1992), the maps by Davidson et al. (1992; see also Rieke et al. 1978) indicated that the northern peak of 50 μm emitting dust may not be located on the ring but rather between the Northern and Eastern Arms inside the cavity; however, this displacement is comparable to the positional uncertainties of their maps. Davidson et al. (1992) concluded that if the displacement is real, neutral material protrudes into the cavity from the northeast, and the relative displacement of the 50 and 100 μm peaks corresponds to a gradient in the

temperature of the heated dust there. Our maps unambiguously confirm this speculation, showing that a higher density tongue of material dominates the northeast quadrant of the cavity. Because we see the tongue of dust in emission at 30 μm (i.e., we have derived the optical depth of 30 μm emitting dust), it must be heated by the radiation field in the cavity; it is not foreground or background emission. This tongue is not obviously correlated with molecular emission (Fig. 6b), although there is some overlap, but it does coincide with a large blob of neutral oxygen seen in [O I] 63 μm emission (Jackson et al. 1993) and apparently cool dust emitting at 450 μm (Dent et al. 1993), as indicated in Figures 6c and 6d. Jackson et al. (1993) suggested that the neutral oxygen they observe toward the cavity is actually within it and may constitute most of the gas mass there. Our results, combined with those of Davidson et al. (1992) and Dent et al. (1993), give 10–450 μm color temperatures that imply external heating of the tongue by a source or sources in the cavity (§ 5).

The 30 μm optical depth across the northeast tongue is fairly uniform, although it increases by nearly a factor of 5 near its northern boundary, where it merges with the ring. The feature's optical depth is typically 0.012, so that the hydrogen column density is about 5×10^{21} cm^{-2}, which agrees reasonably well with the 22'' diameter–beam measurements made of oxygen by Jackson et al. (1993) and with the 30'' diameter–beam measurements of $\tau(90)$ by Davidson et al. (1992). This
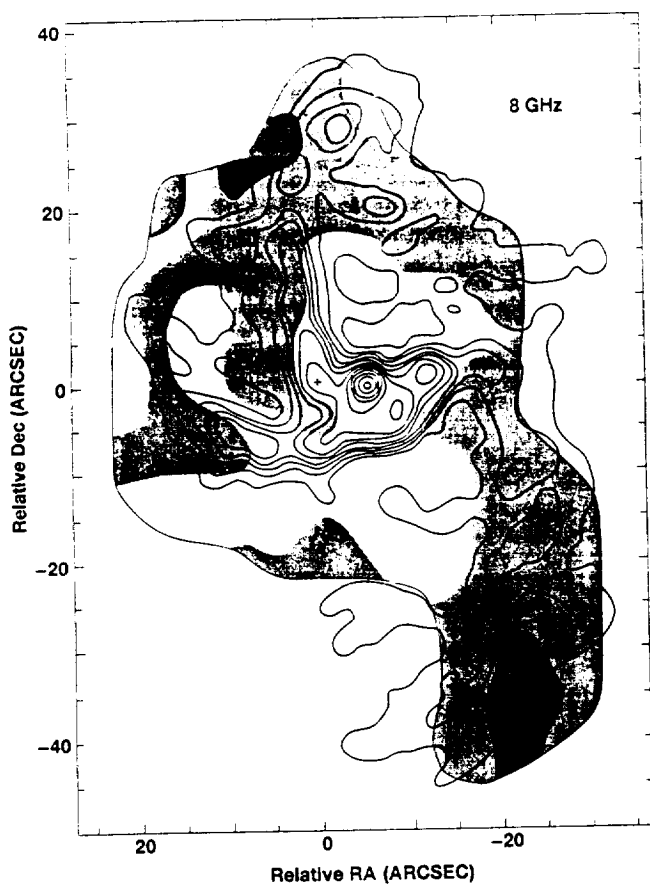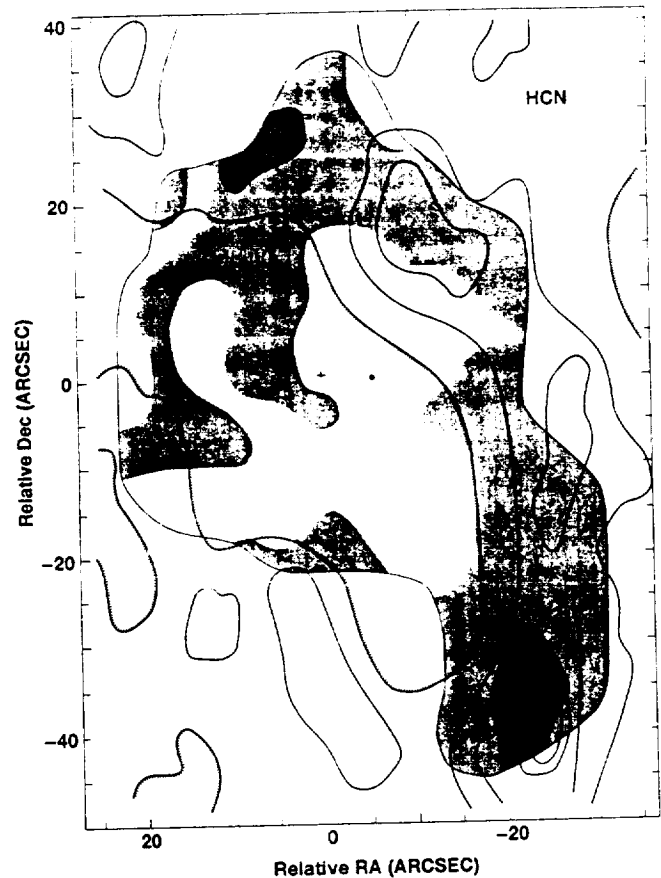
FIG. 6a

FIG. 6b

FIG. 6.—Comparison of the distribution of τ(30) (*shaded area*) derived from the large-scale maps to the following (*a*) 8 GHz continuum (2″.4 beam; Roberts et al. 1991); (*b*) HCN *J* = 1–0 emission (3″ beam; Wright et al., published in Güsten 1987); for clarity, some HCN contours are not shown; (*c*) [O I] 63 μm line emission (22″ beam; Jackson et al. 1993); (*d*) 450 μm continuum emission (7″.2 beam; Dent et al. 1993); for clarity, some 450 μm contours are not shown.

feature probably corresponds to cool matter falling into the cavity, and we refer to it as the Northern Intruder.[3] The Intruder appears to extend about 40″ into the cavity. Based on Figure 5a, we estimate the size of the Intruder to be roughly 20″ × 37″, corresponding to a projected area of about 1.3 pc². Therefore, the total mass of the Intruder is about 50 $M_\odot$, compared to the value of about 7 $M_\odot$ for the mass of ionized gas in the cavity (Jackson et al. 1993). Our estimated mass for the Intruder is about 6 times lower than the value determined by Jackson et al. (1993) for the northern O⁰ lobe; our value

[3] It is worth noting that both the global and fully sampled (Fig. 5b) maps of τ(30) show the concentration of matter about 5″ to the west or northwest of IRS 1 that we associate with the Northern Intruder. Both maps also show matter about 5″ to the south and southwest of IRS 1. However, the maps disagree in the relationship they show between these two concentrations: in the large-scale map, the matter just south of IRS 1 is part of the Intruder, whereas in the fully sampled map it seems to be connected to a tongue of matter that may be part of the eastern segment of the ring. As a practical issue, we consider the large-scale map shown in Fig. 5a to more accurately represent the overall structure of the Intruder, because most of the Intruder was spanned by a single setting of the detector array, which reduced deleterious effects of fluctuating sky transparency at 30 μm. In contrast, the fully sampled map was constructed from fields that were interleaved to achieve Nyquist sampling, with intervening fluctuations in the sky transparency introducing inaccuracies in the inferred structure. The fully sampled data presented for the southwest lobe region is not very affected by this problem, because the maps were constructed from smoothed data (see § 2). Despite these differences, the fully sampled maps clearly corroborate the existence of the Intruder.

may be a better estimate of the neutral gas mass actually protruding into the cavity, whereas theirs, obtained at much lower angular resolution, may better indicate the mass of the whole complex even where it overlaps the ring; however, the dust-to-gas ratio in the Intruder may be lower than the canonical value (Herter et al. 1989; see below), making our estimate a lower limit to the Intruder's mass.

As argued by Jackson et al. (1993), it is likely that neutral gas located in the cavity is infalling rather than being ejected, since gas originating in the central environment, where the dynamical (i.e., mixing) timescales are short and the UV radiation is so intense, would almost certainly be fully ionized. For an infall timescale of 10⁴ yr, the inflow rate is about 0.005 $M_\odot$ yr⁻¹ (see also Jackson et al. 1993), and the Northern Intruder is therefore probably a major source of neutral gas for the cavity, enriching it and fueling the recent star formation there. The Intruder is apparently the leading edge of the large invasive complex that dominates the O⁰ and S⁺ (Herter et al. 1989) and has "punched a hole" in the molecular ring during the infall with such violence that large amounts of dust have been evaporated (Herter et al. 1989).

4.3. Ionized Filaments Viewed as Ionization Fronts

Serabyn & Lacy (1985) and others have proposed that the Western Arc of ionized gas is actually an ionization front

Relative RA (ARCSEC)

FIG. 6c

Relative RA (ARCSEC)
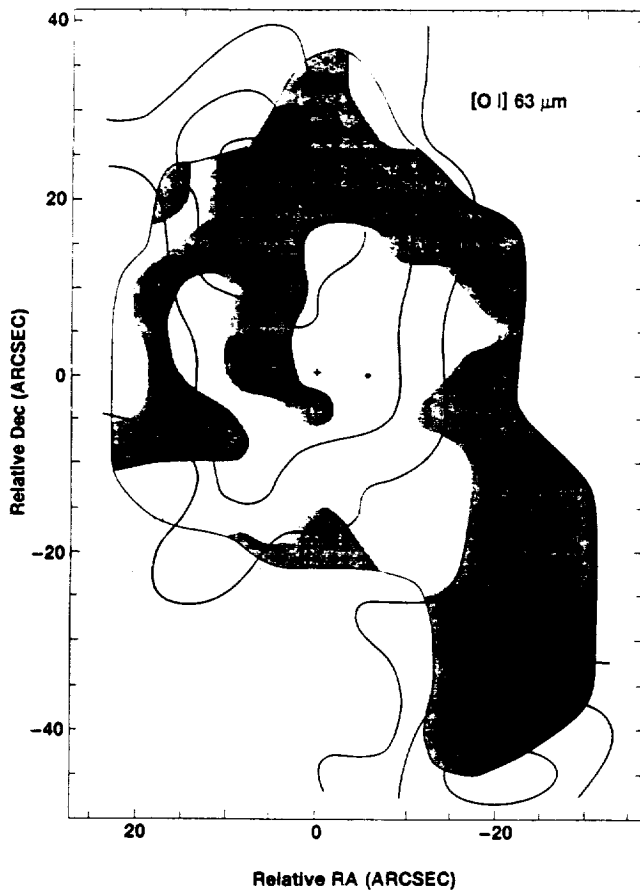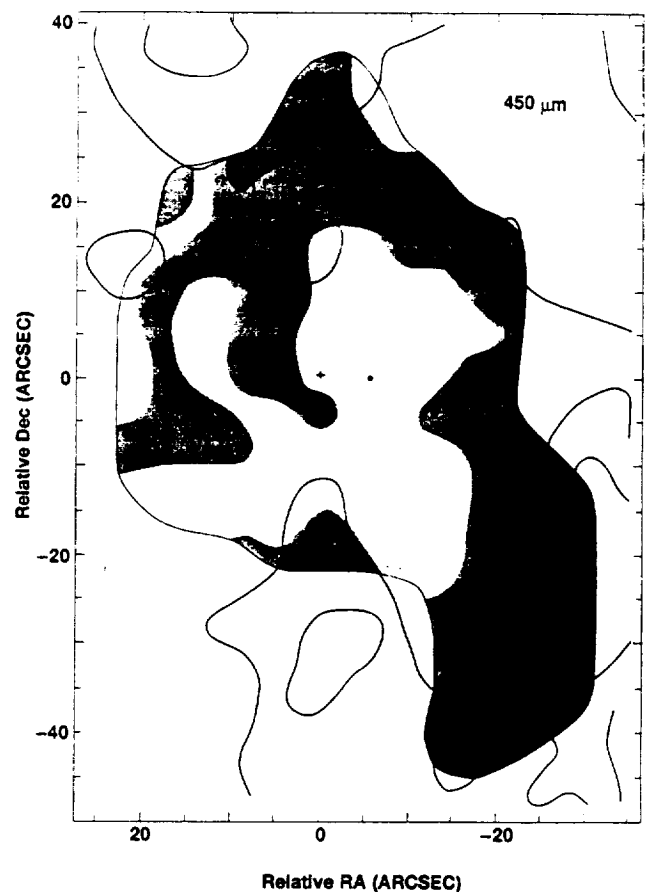
FIG. 6d

located at the inside boundary of the neutral-gas ring. This is evident in Figure 6a, where the Western Arc appears to coincide with the ring, probably because of projection due to the high inclination of the ring with the line of sight. This front presumably results from the ionization by UV sources located within the cavity. Similarly, Davidson et al. (1992) speculated that the Northern Arm is an ionization front associated with higher density gas in the region that we refer to as the Northern Intruder. Our new data permit us to substantially extend these conclusions. Figure 6a indicates that *all* of the major ionized filaments in Sgr A lie along the edges of high-density, high–optical depth features. Without exception, these edges face the center of the cavity, where the complex of potential heating and ionizing sources are located. Within the Western Arc itself, we see that the two ionized peaks in the southwest lobe are at the inner edges of the densest clump; the northern of these two clumps is most clearly shown in Figure 5b. (Note also that the [Ne II] 12.8 μm emission-line map by Lacy et al. 1991 shows much more clearly than does the 8 GHz map presented here that the northern part of the Western Arc is a sharply defined ionization front.) The Northern Arm runs parallel with the Northern Intruder along its entire length all the way from IRS 1 to IRS 8. Especially if we consider the lowest (*dashed line*) $\tau(30)$ contour shown in Figure 5a, it is clear that the Bar lies along the northern edge of a ridge of higher density material (where the hourglass-shaped region is narrowest) that may be the part of the Intruder that curls westward below IRS 1 and Sgr A* toward the Western Arc;

the Bar even appears to press up against the high-density clump located due West of Sgr A*, where the Bar and Western Arc merge. The Eastern Arm is contiguous with a protrusion of high-density material that may coincide with the eastern segment of the molecular ring (see Fig. 6b). It is possible that *that* high-density protrusion, rather than the Intruder, passes south of the Bar and over to the Western Arc, a possibility that is consistent with the fully sampled map of $\tau(30)$ (see footnote 3) and may be more consistent with the known gas dynamics (Serabyn & Lacy 1985). Either way, the Bar appears to be an ionization front at the surface of dense material nearly bisecting the cavity.

On the other hand, the fact that ionization fronts are not located everywhere also tells us something. The bay of lower ionization lying between the Northern and Eastern Arms apparently results from UV shielding of that region by the Northern Intruder; ionizing photons emitted by sources in the cavity do not propagate any farther northeastward than the Northern Arm ionization front. Since the Intruder shields the northeastern part of what is probably a nearly complete ring (Jackson et al. 1993), we must conclude that much of the Intruder lies in the plane of the ring, consistent both with the proposal by Lacy et al. (1991) regarding the location of some of the ionized filaments and the evidence that the Intruder has disrupted the molecular ring (Güsten et al. 1987; Herter et al. 1989). Likewise, the high–optical depth region about 20″ due south of IRS 1 may be unassociated with an ionization front and so may also be shielded from UV radiation by the Bar

region. (However, the Ne$^+$ map by Lacy et al. 1991 shows what may be an ionization front at the northern tip of this feature.)

These comparisons reveal that the ionized filaments that dominate the cavity morphology actually outline the cavity boundaries irradiated by UV radiation. In the next section we explore the distribution of dust temperature throughout the cavity and ring and find that it fits neatly into this picture.

5. THE TEMPERATURE DISTRIBUTION

The main features of the dust temperature throughout the central 5 pc of the Galaxy are most easily seen by considering the three temperature regimes $T_d = 190$–250, 120–140, and 80–90 K. In Figure 7 we show temperature contours from these three regimes overlaid on the map of $\tau(30)$. Each temperature regime corresponds clearly to a zone in Sgr A. Within about 8" of Sgr A*, the temperature distribution resembles roughly that of the emission maps. The hottest dust, at 250 K, coincides with the brightest mid-infrared source IRS 1. Somewhat cooler dust, at about 190 K, is distributed in an arc extending southwest from IRS 1 and westward along the Bar. The maps (see also Fig. 4b) show several temperature peaks, including that at IRS 2 in the Bar. These results are broadly consistent with the distribution of dust effective temperature determined for the same region with higher spatial resolution

by Smith et al. (1990; see also Gezari et al. 1993) using 8.3 and 12.2 μm images. Smith et al. (1990) and others have concluded that many of the discrete sources (e.g., IRS 1 and 2) are heated internally; i.e., they are not merely density enhancements heated by an external source such as Sgr A*.

At distances of 8"–25" from IRS 1, the temperature distribution differs noticably from those of the emission maps from which it was derived. With the exception of a tongue of higher temperature dust extending from IRS 1 toward IRS 4 to the southeast, the isothermal contours across this larger scale region are roughly circularly symmetric. At distances beyond 25", the dust temperatures fall off relatively smoothly with distance from IRS 1, but it is obvious that in the southwest the isothermal contours (e.g., 80–90 K) are tilted almost north-south rather than being perpendicular to the line connecting them to the cavity center near Sgr A* and IRS 1.

The comparison of T_d and $\tau(30)$ in Figure 7 implies that the density and temperature distributions are closely coupled in a way that can be understood in the context of the picture outlined in the previous section. The arc of hottest dust (190–200 K) coincides with the ionization front(s) identified with the Bar and the southern part of the Northern Arm. The temperature of this dust is consistent with this ionization front being the closest ionized feature to the UV heating sources. The intermediate-temperature dust, at 120 K, traces almost precisely the inside edge of the western half of the ring, as expected for external heating. Likewise, the lowest temperature contours (80–90 K) are virtually indistinguishable in shape from the isodensity contours in the southwest lobe and near the high-density concentration located about 30" north of IRS 1.

Although the hottest dust lies unambiguously at the Northern Intruder's ionization front, the intermediate-temperature contours (120–140 K) seem to have no relationship to the Northern Intruder. Rather, they seem to trace what might be the northern and eastern inside edges of the ring. However, that explanation is probably not tenable, because, as we have already shown, the Northern Intruder effectively shields much of the matter in the northeast quadrant from the cluster's UV radiation, which accounts for the paucity of ionized gas there. It seems likely that the temperature determined for this region is that of warm dust mixed with ionized gas located at the front or rear surface of the Intruder. That gas is exposed to ionizing radiation because the cluster of sources is extended along our line of sight and so illuminates the Intruder from a range of directions. Thus, the Northern Arm ionization front is actually part of one that wraps around the front and/or back of the Intruder, and some of the dust that contributes the mid-infrared emission from the main body of the Intruder is heated by UV radiation incident on those surfaces that are more nearly perpendicular to our line of sight. This geometry is consistent with the impression one gets by inspecting Figure 6a; the lower 8 GHz contours of the Northern Arm radiate eastward through the Intruder as though rippling across its front or rear surface.

Some UV and visual radiation may also penetrate into the Intruder and heat the dust there. This is plausible, since $\tau(30) \approx 0.01$ across the Intruder, and the optical depth for outer-cloud dust at $\lambda \leq 0.4$ μm is thus less than 2. If this also corresponds to the radial optical depth of the Intruder, then it is penetrated by more than 10%–15% of the radiation from the cluster that is incident on its surface. The UV radiation that illuminates the Intruder's interior can also dissociate molecules, which would account for their absence there.
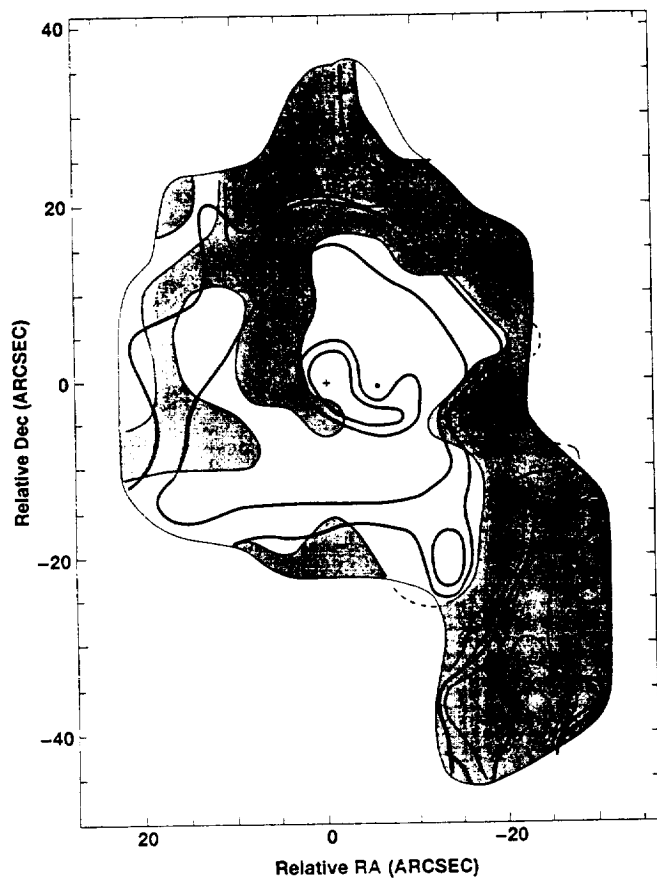

FIG. 7.—Comparison of selected dust temperature contours from Fig. 4a to the distribution of optical depth (Fig. 5a). The temperature contours are 80, 90, 120, 140, 190, and 200 K.

We have computed the temperature distribution expected for dust that is optically thin to UV radiation from a source located near IRS 1. The UV source is assumed to have a blackbody spectral energy distribution with a temperature of 35,000 K, which is the observed excitation temperature of gas in the Sgr A cavity. We solved the equation of radiative equilibrium with the requirement that the dust temperature be 152 K at 12."8 (0.53 pc). This fiducial temperature was chosen because it is the value at the positions 12."8 northwest and 12."8 southwest of IRS 1, which are along lines of sight most typical of the ionized gas away from the neutral gas. As discussed in § 7, the derived luminosity of the source required to heat the dust to these temperatures is different for each of the two extinction curves (§ 3.2), but the resultant temperature distributions are essentially the same. In Figure 8, we show the result of this calculation together with observed temperatures. The plotted symbols indicate the temperatures in the four cardinal directions and toward the southwest into the lobe region. Figure 8 demonstrates that the temperature distribution calculated for optically thin dust defines a loose upper boundary to the distribution of plotted points.. We could have selected some other positions in the map where the temperatures are noticeably above the curve (particularly at point sources such as IRS 4 and 8), but the trends throughout the Sgr A region are well represented by the plotted points.

Temperatures can fall below those expected for several reasons. One is that the dust along our line of sight is at a range of temperatures; only that dust for which the projected distance equals the actual distance from the central heating sources has the highest temperature (which is the computed one shown in Fig. 8), with most of the emitting dust being cooler. This effect is probably most important within 10"–15" of the cluster center, since the line-of-sight temperature gradient is much shallower at larger radii. A related reason is that the neutral-gas ring is tilted about 65° to our line of sight, with the result that dust in the ring along the minor axis is several

times farther away from the cluster than the projected distance and should thus be about 70% cooler than dust at the projected distance. The fact that the isothermal contours so closely follow the optical depth contours along the Western Arc (Fig. 7) is consistent with this expectation.

The dust at a given projected radius may also be lower than expected if the cavity itself is not optically thin to UV radiation. Indeed, in the next section we show that significant UV radiation is absorbed by dust in the cavity. This effect should be most noticeable at the cavity boundary, where there is an abrupt increase in the gas density. In Figure 9 we show contours of $\tau(30)$ and, as shaded pixels, those positions at which the observed temperature is at least 10 K below the temperature predicted from the model of optically thin UV heating by a central source. Dust particles that are much cooler than expected coincide well with regions of higher optical depth, i.e., with dense neutral material. Thus, there is a unambiguous reduction in the amount of radially propagating UV radiation at the cavity-ring boundary, an issue we address further in the next section.

6. THE PROPAGATION OF UV RADIATION IN SGR A

Consider the propagation of UV radiation through the cavity. The optical depth through the cavity is low, with $\tau(30) = 0.003$ being a typical value away from the ionization fronts and dense neutral gas. For outer-cloud dust, the UV
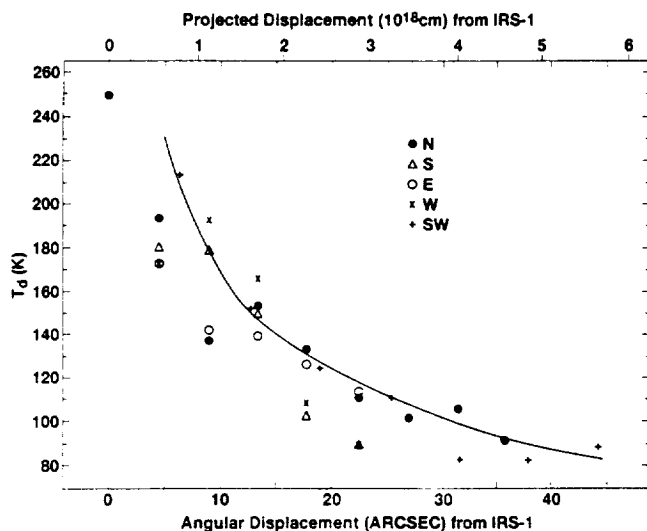

FIG. 8.—Observed dust temperatures (symbols) as a function of distance from IRS 1 in the cardinal directions and to the southwest. The curve represents the distribution of temperature expected for optically thin dust heated by a UV source located near IRS 1. The equation of radiative equilibrium has been solved with the requirement that the dust temperature be 152 K at 12."8 from IRS 1.
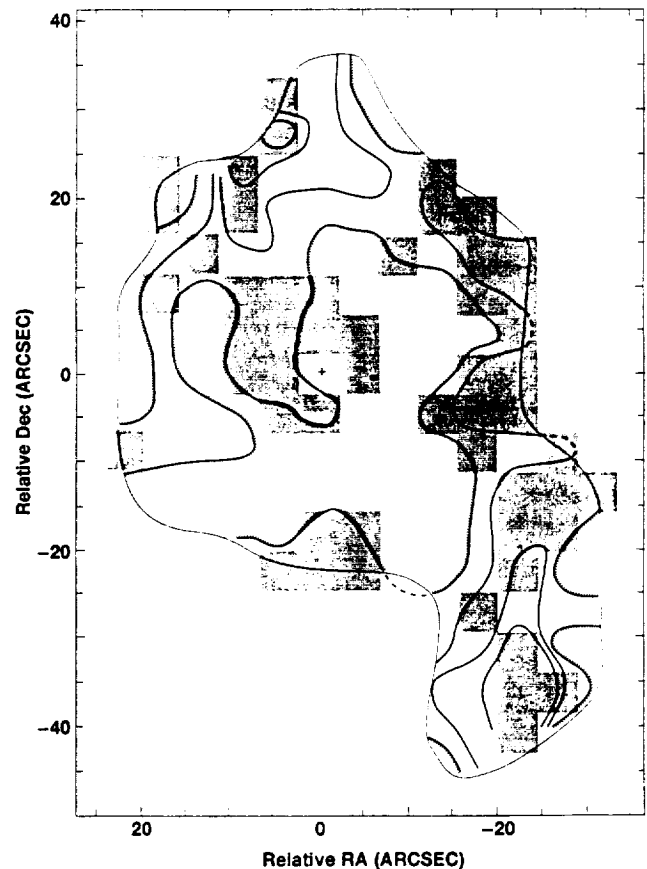

FIG. 9.—The shaded pixels indicate the positions at which the observed dust temperatures are at least 10 K below the temperatures predicted by the model of optically thin UV heating by a central source. The contours indicate regions of higher optical depth in emitting dust (Fig. 5a).

extinction at about 0.14 μm, where the spectrum of a 35,000 K blackbody heating source peaks, is roughly 300 times larger than the 30 μm extinction. For diffuse dust, this ratio is roughly 500. Therefore, $\tau(UV) \approx 0.8$–1.5 *through* the cavity, and we estimate the radial UV optical depth (e.g., from the cavity center near IRS 1 to the edge of the cavity) to be 0.4–0.8. We conclude that about half of the UV photons emitted in the vicinity of IRS 1 and Sgr A* actually propagate to the boundary.

The UV radiation that propagates to the cavity boundary can contribute to (or dominate) the heating of gas and dust in the neutral-gas ring, and it is of interest to ask how far we expect the UV radiation to penetrate into the ring. Along the western part of the molecular ring, $\tau(30)$ ranges from about 0.04 in the northwest to nearly 0.2 in the southwest (Fig. 5). For outer-cloud dust, $\tau(UV) \approx 11$ and 55, respectively, along those lines of sight. The average gas density $\langle n \rangle$ in the southwest lobe is about 5×10^4 cm^{-3} (§ 4). For the more typical parts of the ring, $N(H) \approx 6 \times 10^{21}$ cm^{-2}, with corresponding densities of about 4×10^3 cm^{-3}. The physical distance ΔR over which $\tau(UV) = 1$ defines the cavity-ring interface thickness: $\Delta R = N(H)/\langle n \rangle = (2 \times 10^{21})\tau(UV)/\langle n \rangle$, for outer-cloud and ρ Oph dust (§ 4). Thus, we expect the interface to be roughly 0.02 pc (0″.4) thick toward the southwest lobe and 0.15 pc (3″–4″) thick toward the northwest part of the ring. The optical depth throughout most of the Northern Intruder should be comparable to that in the northwest part of the ring, so the penetration depth of the UV radiation into the Intruder should also be about 0.15 pc, corresponding to 4″–5″, or 1 pixel width.

Some regions at the cavity-ring interface, such as to the northwest, show temperature gradients roughly consistent with our estimates of ΔR, but others do not. If we examine the scans through the southwest lobe presented in Figure 3, we see that the temperature falloff is much less steep there than expected from our simple picture. In fact, the dust temperature along the diagonal scan changes monotonically from about 90 K at 1.3 pc from IRS 1 to about 63 K at 2.1 pc. The temperatures of about 60 K inferred for the southwest lobe are the lowest in the map, but they are nevertheless unexpectedly high for dust located in a region of such high optical depth. As we proposed for the Intruder, this effect may result from there being a tilt of the cavity/ring interface to our line of sight, so that we are seeing some gas along our line of sight to the high-density lobe that is directly illuminated by the central cluster and not physically located in the high-density clump.

A more interesting, but purely speculative, alternative is that a substantial amount of UV radiation may be penetrating far into the southwest cloud complex, again, as we proposed for the Intruder. To see this we assume that the UV luminosity of heating sources located at the cavity center is in the range 0.6–2×10^7 L$_\odot$ (§ 7). The dust temperature at $r = 2.1$ pc, which would be about 80 K for optically thin heating (Fig. 8), is near the observed value of 63 K if the emitted UV radiation is attenuated by an optical depth $\tau(UV) \approx 1$–2. However, based on typical values of $\tau(30)$ in the southwest lobe, we would expect $\tau(UV) > 10$. If the cloud is very clumpy, or porous, UV radiation can penetrate farther into it than indicated by the calculated values of ΔR. Our rough estimate for $\tau(UV)$ implies that more than 10% of the UV radiation incident on the most prominent molecular cloud complex in the southwest lobe might penetrate to several tenths of a parsec into the cloud. If the areal filling factor of this molecular gas at the inner part of the neutral-gas ring is 10%, as estimated by Jackson et al. (1993), then penetration by UV radiation deep into the ring

and even through the molecular gas is possible (see also Herter et al. 1989).

Note also that the right ascension scan shown in Figure 3a indicates a dust temperature beyond 10″ that is roughly constant or at least not rapidly decreasing with distance. It seems most plausible that this sustained temperature level results from the fact that the western end of that scan, like the eastern end, emerges somewhat from the high-density molecular ridge into a region of lower density that is directly exposed to UV radiation from the cavity. Both the $\tau(30)$ and HCN maps (Figs. 5b and 6b) imply that the southwest lobe contains two large molecular complexes. A gap of 5″–10″ (0.2–0.4 pc) in declination separates the two complexes, and we propose that UV radiation from the central cavity passes through the gap and heats gas and dust at larger radii in the ring, including that observed at the west end of the right ascension scan in Figure 3. The locally elevated dust temperature within the gap is also clearly evident in the temperature maps in Figure 4, and it coincides with the prominent southwest lobe of 450 μm emission (Fig. 6d) and a large westward ballooning of the lowest 10.8 and 19.2 μm contours (Figs. 1a and 1b). Thus, we may be seeing direct evidence for the propagation of UV radiation to larger radii through gaps in the larger scale cloud distribution. This effect and the possible porosity of individual cloud complexes could enable UV radiation to propagate outward through the molecular ring, as suggested by Davidson et al. (1992) to account for the extended far-infrared emission from Sgr A.

Equally plausible is the possibility that one or more sources embedded in the ring locally heat that southwest region; indeed, that explanation might more easily account for the coincidence of the localized "hot spot" with NH$_3$ clump G detected there by Jackson, Ho, & Barrett (1987). As a very crude estimate of the properties of this hypothetical source, we assume that all the 19.2 μm flux density of about 3 Jy in the 1 pixel at that location is due to heating of the enshrouded source. With a 10–1000 μm spectral energy distribution like that from the 1′ diameter region at the infrared luminosity peak in Orion (Werner et al. 1976), the southwest source would then have a total luminosity of 4–5 $\times 10^3$ L$_\odot$, about that of an early B star.

7. THE LUMINOSITY OF THE CENTRAL HEATING SOURCES

Determination of the infrared luminosity of Sgr A is complicated by the large mid-infrared extinction to the Galactic center. We have applied the corrections for interstellar extinction discussed in § 3.2 to the flux densities for the cavity and ring presented in Figure 1e. For the far-infrared fluxes of the cavity, we use the 50 and 100 μm flux densities measured by Becklin et al. (1982) for the central 30″ of Sgr A, corrected for extinction and multiplied by the factor $(40/30)^2$ to adjust their fluxes to the somewhat larger cavity area that we assume. The 10–100 μm luminosity emitted by the cavity is then 9×10^6 L$_\odot$. After correcting for interstellar extinction, Gezari et al. (1993) derive a luminosity of 5×10^6 L$_\odot$ for the central 15″ diameter region. From our 10.8 μm map we find that about half of the flux density that we attribute to the 40″ cavity arises in the region considered by Gezari et al. (1993), so that both values of the luminosity are consistent, with ours being a more complete sampling of the power emitted by the whole cavity.

We determine the infrared luminosity of the ring by subtracting the cavity flux densities discussed above from the total 50 and 90 μm flux densities observed across the Sgr A region by
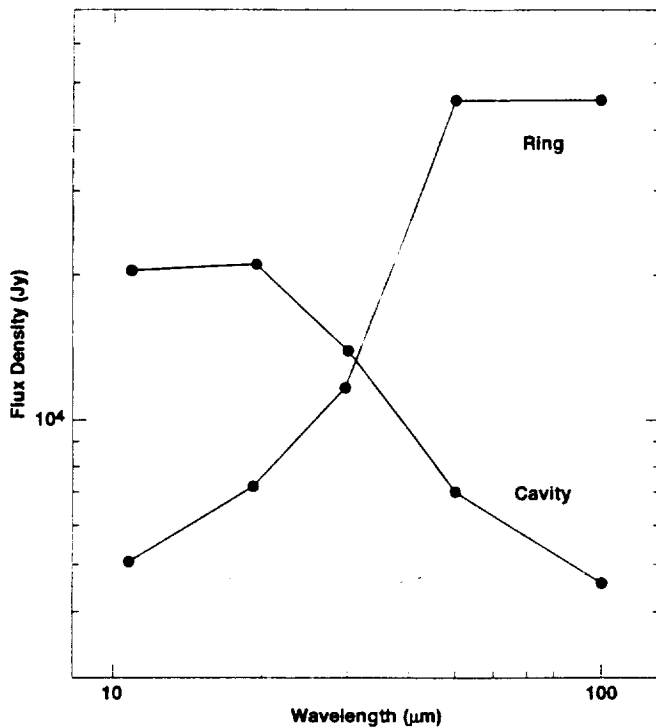
FIG. 10.—The spectral energy distributions of the cavity and the ring after correction for interstellar extinction. These are used to compute the luminosities discussed in the text. The 10–30 μm data are from the present work, and the far-infrared data are from Becklin et al. (1982) and Davidson et al. (1991) (see text).

Davidson et al. (1992), who detected 39,500 Jy at 50 μm and 44,900 Jy at 90 μm (we assume a total 100 μm flux density equal to this 90 μm value). This spectral energy distribution is plotted in Figure 10. The 10–100 μm luminosity emitted by the ring is then 8×10^6 $L_\odot$, and the total infrared luminosity emitted by Sgr A (cavity plus ring) is 1.7×10^7 $L_\odot$.

The uncertainty in the emitted luminosity of the cavity is dominated by the uncertainty in the extinction correction, but, for the ring, it is dominated by measurement uncertainties of the far-infrared fluxes. This is because the extinction correction is large at 10–30 μm, where the spectrum of the cavity peaks, but relatively small at 50–100 μm, where the spectrum of the ring peaks. At 30–100 μm, we take the uncertainty in the extinction correction to be 15%, which is about half of the average value of the applied correction at 50 and 100 μm. Since the measurement and calibration uncertainty of the far-infrared fluxes is about 30%, the emitted far-infrared flux is known to roughly 35%. At shorter wavelengths, we assume that the uncertainty in the extinction correction is character-ized by our ignorance of the shape of the silicate absorption feature toward the Galactic center. As a measure of that uncertainty we take the range of values observed toward various Galactic sources of the ratio of the visual extinction to the depth of the feature at 9.7 μm: $A_V/\tau_s(9.7) = 10$–25 (Gillett et al. 1975; Rieke 1974). Half the range in this value divided by the mean corresponds to an uncertainty of about 43%. Since nearly all (94%) of the cavity flux is emitted at 10–30 μm, the uncertainty in the cavity luminosity is about 43%. About 65% of the ring luminosity is emitted at 30–100 μm, and so we estimate the uncertainty in the luminosity emitted by the ring to be roughly 40%. Thus, the luminosities emitted by the cavity

and ring are $9 \pm 4 \times 10^6$ $L_\odot$ and $8 \pm 3 \times 10^6$ $L_\odot$, respectively. The total for the Sgr A region is $1.7 \pm 0.5 \times 10^7$ $L_\odot$, where we have assumed that the uncertainties in the ring and cavity luminosities are independent since they have essentially different origins.

We have shown that the relationship of the heated dust, and the neutral and ionized gas throughout Sgr A is consistent with heating and ionization by UV radiation originating in the neighborhood of IRS 1 and Sgr A*. We now compare the observed luminosity as determined above to the UV luminosity required to heat the dust to the inferred temperatures. We assume extinction properties of the cavity dust to be those of diffuse dust, and we take the dust temperatures to be those that are fitted by the curve drawn in Figure 8, which corresponds to the temperatures of dust in radiative equilibrium with a central UV source. Points falling close to that curve tend to be associated with positions in the cavity (e.g., at 25″5, or 1.06 pc, southwest of IRS 1, where $T_d = 112$ K) rather than in the ring or Northern Intruder, where, as already discussed, UV radiation is strongly attenuated. The required luminosity is 6.0×10^6 $L_\odot$. If we use the extinction properties of outer-cloud dust, then the dust temperatures imply a luminosity of 1.1×10^7 $L_\odot$. Thus, the dust temperatures imply that the UV luminosity propagating to the edge of the cavity is (6–11) $\times 10^6$ $L_\odot$. Since it is likely that roughly half of the UV photons emitted near the center of the cavity are absorbed by cavity dust and emitted in the infrared (i.e., the UV intensity at 1 pc from IRS 1 is the attenuated field near the outer edge of the cavity; see § 6), we infer from the dust temperatures that the emitted infrared luminosity of the cavity is also (6–11) $\times 10^6$ $L_\odot$, or (9 $\pm$ 3) $\times 10^6$ $L_\odot$, and the total UV luminosity emitted in the cavity is (1.2–2.2) $\times 10^7$ $L_\odot$, or (1.7 $\pm$ 0.5) $\times 10^7$ $L_\odot$. These values agree with the cavity's observed infrared luminosity of (9 $\pm$ 4) $\times 10^6$ $L_\odot$ and the total infrared luminosity of (1.7 $\pm$ 0.5) $\times 10^7$ $L_\odot$. It is worth emphasizing this good agreement in the luminosities determined for Sgr A by essentially two independent approaches: direct observation of the infra-red luminosity with a significant correction for intervening interstellar extinction, and analysis of the UV luminosity required to heat the dust to the inferred temperatures.

The UV heating sources emit about 1.7×10^7 $L_\odot$, of which roughly half (9 $\pm$ 3 $\times 10^6$ $L_\odot$) propagates to the edge of the cavity. Within the uncertainties, as little as 40% (i.e., [8 − 3 $\times 10^6$ $L_\odot$] [9 + 3 $\times 10^6$ $L_\odot$] = 0.42) or as much as 100% of the radiation escaping the cavity is absorbed in the ring. The ring does not subtend 4π sr at the cavity center, so the upper limit is uninteresting. For a cavity diameter of 2 pc, the lower limit corresponds to a ring thickness at its inner edge of about 0.8 pc, a value that drops to about 0.6 pc if, as inferred by Davidson et al. (1992), as much as 2×10^6 $L_\odot$ of the ring's infrared luminosity results from heating of the dust by the old stellar population. One's impression from the available maps of the Galactic center at various wavelengths is that this lower limit is within the plausible range of values.

Among the primary candidate objects to provide the central UV luminosity of (1.7 $\pm$ 0.5) $\times 10^7$ $L_\odot$ are a group of about a dozen compact, broad-line "He I emission stars" and probably an associated, but not yet detected, population of fainter OB stars distributed across the central $\sim 20''$ of the Galactic center (Forrest et al. 1987; Allen et al. 1990; Krabbe et al. 1991). Most of the He I stars are coincident with compact 2 μm continuum sources, which supports the claim that many of these contin-uum peaks are internally heated (e.g., Rieke et al. 1989). These

objects appear to be hot stars (mass-losing blue supergiants and/or Wolf-Rayet stars) that ionize the helium in their winds. From data on late Ofpe/WN stars and other blue supergiants, Krabbe et al. (1991) infer that the ratio of luminosity to 2.2 μm flux density for these stars is $8 \times 10^5 L_\odot$ Jy^{-1} (adjusted to 8.5 kpc for the Galactic center distance). The dereddened 2.2 μm emission from the individual objects implies luminosities in the range $(0.4-5) \times 10^6 L_\odot$, with the total being as high as 1×10^7 $L_\odot$. Objects such as IRS 1, IRS 16C, and IRS 16NE, with 2.2 μm flux densities of a few janskys (e.g., Krabbe et al. 1991), may each emit about $2 \times 10^6 L_\odot$.

8. SUMMARY AND CONCLUSIONS

Our maps of the 10–30 μm emission from warm dust in the central 5 pc of the Galaxy have permitted us to draw the following conclusions about the distribution of neutral and ionized gas and the energetics in the Sgr A cavity and the inner part of the molecular ring.

1. The 30 μm optical depth indicates that the mid-infrared–emitting dust is distributed in a low-density cavity, where the average gas density away from filaments is about 300 cm^{-3}, bordered by a high-density ridge, where the average gas densities is as high as 10^5 cm^{-3}. The cavity and ridge correspond to the well-known ionized cavity and the inner part of the neutral-gas ring, respectively.

2. We see a high-density tongue of warm dust that extends into the center of the cavity from the northern part of the ring. Because the dust associated with this tongue, which we call the Northern Intruder, is heated by radiation in the cavity, we confirm previous speculations that high-density matter actually protrudes into the cavity from the ring and that significant gas is therefore probably falling into the cavity and fueling star formation there. We identify the Intruder with the concentration of neutral oxygen mapped by Jackson et al. (1993). The mass of the Intruder is approximately 50 $M_\odot$, which is nearly an order of magnitude larger than the mass of ionized gas associated with cavity.

3. By comparing the distribution of warm dust mass to the 8 GHz thermal bremsstrahlung emission, we show that *all* the major ionized filaments (the Western Arc, the Northern Arm, the Bar, and the Eastern Arm) in the cavity are actually ionization fronts at the interfaces between the low-density cavity and the high-density regions defined by the neutral-gas ring and the Northern Intruder. The locations of these ionization fronts and the distributions of dust temperatures imply that the dominant UV heating and ionizing sources are centrally located in the cavity.

4. The dust temperatures decrease away from the center of the cavity and show a significant drop near the interfaces of the cavity and the higher-density regions, as expected generally from external heating of dense clouds. However, in some dense regions, particularly the southwest molecular cloud complex, the dust temperatures appear to be higher than expected for such dense regions. This effect may result from there being either a tilt of the cavity-ring boundary to our line of sight or a local heating source. A third alternative is that UV radiation penetrates deeply into those cloud complexes because the clouds are clumpy, or porous. This small-scale clumpiness and the easily observed larger-scale clumpiness permit UV photons from the cavity to propagate far out into the molecular ring.

5. After correcting the observed flux densities for interstellar extinction, we estimate that the infrared luminosities emitted by the cavity and ring are $(9 \pm 4) \times 10^6 L_\odot$ and $(8 \pm 3) \times 10^6$ $L_\odot$, respectively, and the total infrared luminosity is $(1.7 \pm 0.5) \times 10^7 L_\odot$. Depending on the assumed wavelength-dependence of the extinction, the dust temperatures near the edge of the cavity require that the UV heating flux there correspond to a luminosity of $(6-11) \times 10^6 L_\odot$, or $(9 \pm 3) \times 10^6 L_\odot$. Since we estimate that about half of the UV photons emitted by sources near the cavity center are absorbed by dust in the cavity, the implied total UV luminosity emitted by sources powering the Sgr A region is $(1.7 \pm 0.5) \times 10^7 L_\odot$. Thus, the observed infrared luminosities are comparable to those emitted by the cluster of UV sources and absorbed by the cavity dust.

6. Within the uncertainties, all, or as little as 40%, of the UV radiation that propagates to the edge of the cavity is absorbed by the neutral-gas ring. The lower limit corresponds to a ring thickness of 0.8 pc if the inner diameter of the ring is 2 pc. If as much as $2 \times 10^6 L_\odot$ of the ring's infrared luminosity results from heating of the dust by the old stellar population, as proposed by Davidson et al. (1992), the lower limit to the ring thickness is 0.6 pc.

REFERENCES

Allen, D. A., Hyland, A. R., & Hillier, D. J. 1990, MNRAS, 244, 706
Becklin, E. E., Gatley, I., & Werner, M. W. 1982, ApJ, 258, 135
Becklin, E. E., & Neugebauer, G. 1975, ApJ, 200, L71
Chan, K.-W., Moseley, S. H., Casey, S., Harrington, P., Dwek, E., Loewenstein, R., & Glaccum, W. 1995, paper presented at 185th AAS meeting (Tucson)
Davidson, J. A., et al. 1992, ApJ, 387, 189
Dent, W. R. F., Mathews, H. E., Wade, R., & Duncan, W. D. 1993, ApJ, 410, 650
Draine, B. T., & Lee, H. M. 1984, ApJ, 285, 89
Eckart, A., Genzel, R., Krabbe, A., Hofmann, R., van der Werf, P. P., & Drapatz, S. 1992, Nature, 355, 526
Forrest, W. J., Shure, M. A., Pipher, J. L., & Woodward, C. E. 1987, in AIP Conf. Proc. 155, The Galactic Center, ed. D. C. Backer (New York: AIP), 153
Gatley I. 1982, in AIP Conf. Proc 83, The Galactic Center, ed. G. R. Riegler & R. D. Blandford (New York: AIP), 25

Gatley, I., Becklin, E. E., Werner, M. W., & Wynn-Williams, C. G. 1977, ApJ, 216, 277
Gezari, D., Dwek, E., & Varosi, F. 1993, preprint
Gezari, D., Ozernoy, L., Varosi, F., McCreight, C., & Joyce, R. 1994, in The Nuclei of Normal Galaxies: Lessons from the Galactic Center, ed. R. Genzel & A. I. Harris (Dordrecht: Kluwer), in press
Gezari, D. Y., et al. 1987, in AIP Conf. Proc. 155, The Galactic Center, ed. D. C. Backer (New York: AIP), 146
Gezari, D. Y., & Yusef-Zadeh, F. 1990, in ASP Conf. Ser. 14, Astrophysics with Infrared Arrays, ed. R. Elston (San Francisco: ASP), 214
Gillett, F. C., Kleinmann, D. E., Wright, E. L., & Capps, R. W. 1975, ApJ, 198, L65
Güsten, R. 1987, in AIP Proc. 155, The Galactic Center, ed. D. C. Backer (New York: AIP), 103
Güsten, R., Genzel, R., Wright, M. C. H., Jaffe, D. T., Stutzki, J., & Harris, A. I. 1987, ApJ, 318, 124

Harvey, P. M., Campbell, M. F., & Hoffmann, W. F. 1976, ApJ, 241, L183
Herter, T., Gull, G. E., Megeath, S. T., Rowlands, N., & Houck, J. R. 1989, ApJ, 343, 696
Herter, T., Houck, J. R., Shure, M., Gull, G. E., & Graf, P. 1984, ApJ, 287, L15
Jackson, J. M., et al. 1993, ApJ, 402, 173
Jackson, J. M., Ho, P. T. P., & Barrett, A. H. 1987, in AIP Conf. Proc. 155, The Galactic Center, ed. D. C. Backer (New York: AIP), 99
Krabbe, A., Genzel, R., Drapatz, S. & Rotaciuc, V. 1991, ApJ, 382, L19
Lacy, J. H., Achtermann, J. M., & Serabyn, E. 1991, ApJ, 380, L71
Mathis, J. S. 1990, ARA&A, 28, 37
McCarthy, J. F., Forrest, W. J., Briotta, D. A., & Houck, J. R. 1980, ApJ, 242, 965

Rieke, G. H. 1974, ApJ, 193, L81
Rieke, G. H., & Low, F. J. 1973, ApJ, 184, 415
Rieke, G. H., Rieke, M. J., & Paul, A. E. 1989, ApJ, 336, 752
Rieke, G. H., Telesco, C. M., & Harper, D. A. 1978, ApJ, 220, 556
Roberts, D. A., Goss, W. M., van Gorkom, J. H., & Leahy, J. P. 1991, ApJ, 366, L15
Savage, B. D., & Mathis, J. S. 1979, ARA&A, 17, 73
Serabyn, E., & Lacy, J. 1985, ApJ, 293, 445
Smith, C. H., Aitken, D. K., & Roche, P. F. 1990, MNRAS, 246, 1
Werner, M. W., et al. 1976, ApJ, 204, 420
Zylka, R., Mezger, P. G., Ward-Thompson, D., Duschl, W. J., & Lesch, H. 1995, A&A, 297, 83

The Magnetic Field Structure in High-Mass Star Formation Regions

J. A. Davidson
SETI Institute; NASA Ames Research Center, MS 245-6, Moffett Field, CA 94035-1000

D. Schleuning, J. L. Dotson, C. D. Dowell, and R. H. Hildebrand
Department of Astronomy and Astrophysics, Yerkes Observatory, and Enrico Fermi Institute, The University of Chicago, Chicago, IL 60637
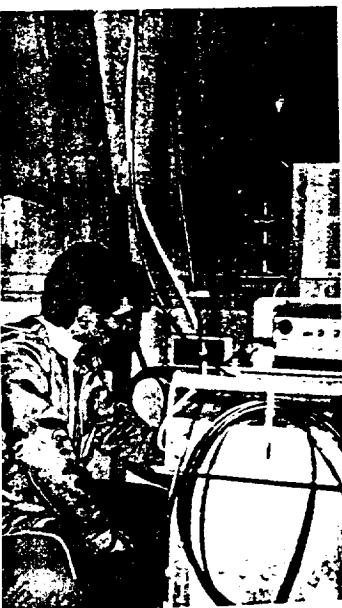
ABSTRACT. We present a preliminary analysis of far-IR polarimetric observations, which were made to study the magnetic field structure in the high-mass star formation regions of M42, NGC2024, and W3. These observations were made from the Kuiper Airborne Observatory (KAO), using the University of Chicago far-IR polarimeter, Stokes.

man (1981)

Gull, Ray Russell (1978)

1. Introduction

It has long been thought that magnetic fields are important to the process of star formation. Magnetic fields probably influence the macroscopic formation of molecular clouds (e.g., Parker 1966). Magnetic pressure and tension may also regulate the efficiency of star formation in molecular clouds by halting cloud collapse until ambipolar-diffusion occurs (Mouschovias 1976). Once cloud cores have formed, magnetic fields may be the agents that help transfer angular momentum of the material in the cores to material in the outer envelopes, enabling further collapse to form protostars (Mouschovias & Paleologov 1980). Not only are magnetic fields invoked to make accretion possible, but to end it. Pudritz & Norman (1983) suggested that the observed molecular outflows from Young Stellar Objects (YSOs) could be magnetically driven. The force of these outflows could halt further accretion. More recently, Shu, Adams, & Lizano (1987) have suggested that the ratio of magnetic to gravitational energy in a molecular cloud could be one factor determining whether a particular cloud will form high-mass stars, since the accretion rate for a given protostar is proportional to the cube of the virial speed of the medium being accreted, and the virial speed can be enhanced by a high magnetic flux to mass ratio; the increase in accretion rates leads to more massive stars, since more massive protostars are formed before outflows can terminate the process.

In this paper we discuss the properties of the magnetic fields in three star formation regions as inferred from recent results of far-IR polarimetry. We will assume that polarized far-IR fluxes are due to the emission from

The Magnetic Field Structure in High-Mass Star Formation Regions

J. A. Davidson
*SETI Institute; NASA Ames Research Center, MS 245-6, Moffett Field,
CA 94035-1000*

D. Schleuning, J. L. Dotson, C. D. Dowell, and R. H. Hildebrand
*Department of Astronomy and Astrophysics, Yerkes Observatory, and
Enrico Fermi Institute, The University of Chicago, Chicago, IL 60637*

ABSTRACT. We present a preliminary analysis of far-IR polarimetric observations, which were made to study the magnetic field structure in the high-mass star formation regions of M42, NGC2024, and W3. These observations were made from the Kuiper Airborne Observatory (KAO), using the University of Chicago far-IR polarimeter, Stokes.

1. Introduction

It has long been thought that magnetic fields are important to the process of star formation. Magnetic fields probably influence the macroscopic formation of molecular clouds (e.g., Parker 1966). Magnetic pressure and tension may also regulate the efficiency of star formation in molecular clouds by halting cloud collapse until ambipolar-diffusion occurs (Mouschovias 1976). Once cloud cores have formed, magnetic fields may be the agents that help transfer angular momentum of the material in the cores to material in the outer envelopes, enabling further collapse to form protostars (Mouschovias & Paleologov 1980). Not only are magnetic fields invoked to make accretion possible, but to end it. Pudritz & Norman (1983) suggested that the observed molecular outflows from Young Stellar Objects (YSOs) could be magnetically driven. The force of these outflows could halt further accretion. More recently, Shu, Adams, & Lizano (1987) have suggested that the ratio of magnetic to gravitational energy in a molecular cloud could be one factor determining whether a particular cloud will form high-mass stars, since the accretion rate for a given protostar is proportional to the cube of the virial speed of the medium being accreted, and the virial speed can be enhanced by a high magnetic flux to mass ratio; the increase in accretion rates leads to more massive stars, since more massive protostars are formed before outflows can terminate the process.

In this paper we discuss the properties of the magnetic fields in three star formation regions as inferred from recent results of far-IR polarimetry. We will assume that polarized far-IR fluxes are due to the emission from

rotating, dust grains, which have their rotation axes aligned with the local magnetic field. It then follows that far-IR polarization measurements map the structure of magnetic field lines in the plane-of-the-sky; the field lines are perpendicular to the E-vector of the polarized emission.

2. Observations and Results

The far-IR polarimetry reported here was carried out on the KAO over a three year period from 1991 to late 1993. We used the far-IR polarimeter of the University of Chicago, Stokes. This instrument is described in Platt et al. (1994). Measurements were made at 100 μm with a spatial resolution of 35". Stokes has an array of 32 beams in a 6 x 6 configuration (with the corner beams omitted), covering an area of 3.7 x 3.7 on the sky. A list of the star forming regions studied by us during this period and an overview of our results are given by Hildebrand et al. (1994). Here we will discuss three regions of high-mass star formation, NGC 2024, M42, and W3.

2.1 NGC 2024 and M42

NGC 2024 and M42 are two regions in the Orion Cloud Complex, which lies in the Cygnus Arm of our galaxy only 500 pc from our sun. This complex of dark clouds, H II regions, supernova remnants, and both high-mass and low-mass star formation sites, buckles out of the plane of the Galaxy in a horseshoe shape extending vertically below the plane about 20 degrees or 180 pc (see the CO maps of Maddalena et al. 1986). NGC 2024 and M42 are small regions within the giant molecular clouds, Orion B and Orion A respectively, where high-mass stars have recently formed and are still forming; hence, these regions contain both H II regions and bright far-IR sources. The large scale magnetic field structure in the diffuse regions of the Orion Complex is predominantly perpendicular to the Galactic plane as determined by the optical polarization measurements of stars located in the Orion Complex region reported in Mathewson and Ford (1970).

Figure 1 shows continuum maps of NGC 2024 at 40 and 100 μm (Thronson et al. 1984), and at 350 μm (Mezger et al. 1988). Superimposed on the 100 μm map are vectors, showing our measurements of the direction and degree of polarization at 100 μm. The three maps in Figure 1 show how the short wavelengths highlight the warm, HII region in NGC 2024 (a region with an E-W morphology), while the long wavelengths highlight the cold, dark, dust lane (a region with a N-S morphology). The 100 μm emission lies between these two extremes. Polarimetry based on this emission will be complicated by the superposition of two distinct regions in the same line-of-sight. Our 100 μm polarimetry results show that in the outer regions of NGC 2024 the magnetic field seems orderly and approximately perpendicular to the plane of the Galaxy, but near and in the dust lane (in projection) they are distorted. However, this could be the effect of two uniform fields in projection, one in the warm gas and the other in the cold gas. Complementary observations at about 60 μm and 400 μm, for example, can help to disentangle these projection effects.

M42 is a compact, blister, H II region (diameter of ~0.5 pc) in front of and eating into the dense molecular cloud, OMC-1. The HII region is excited
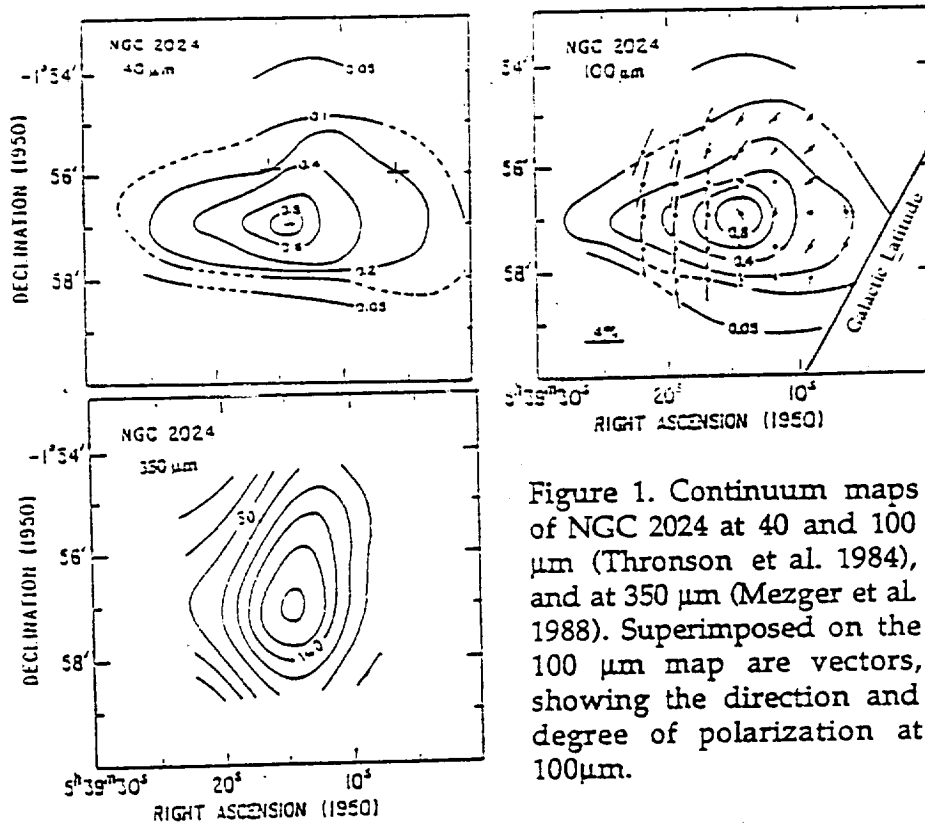
Figure 1. Continuum maps of NGC 2024 at 40 and 100 μm (Thronson et al. 1984), and at 350 μm (Mezger et al. 1988). Superimposed on the 100 μm map are vectors, showing the direction and degree of polarization at 100μm.

by OB stars in the Trapezium Cluster which lie in front of OMC-1. Within OMC-1, but presumably near its surface, lie four mass concentrations along a ridge (based on the CS measurements of Mundy et al. 1988), each about 0.04pc in diameter and 50 $M_\odot$ in mass. One is a bright IR source, BN-KL, which contains two massive YSOs, BN and IRc-2, of about 20 $M_\odot$ each; IRc-2 exhibits a powerful bipolar outflow. (Also forming within OMC-1 are a large number of low-mass stars, which are more evenly distributed.) Figure 2 shows our far-IR flux and polarization map of the M42/OMC-1 region. Indicated in this figure is the region called the molecular bar, which is thought to be part of the OMC-1 cloud that envelops the bottom of the HII region; it protrudes towards the observer (see Thronson et al. 1986). Our polarization measurements in Figure 2 were all made in November 1993 using Stokes. Previous 100 μm polarimetry observations of this region by Gonatas et al. (1990), made with the single-beam, University of Chicago polarimeter on the KAO, measured only ten positions in this region. The Gonatas et al. results agree with those presented here.

The polarization measurements in Figure 2 imply that: (i) the overall direction of the field in the OMC-1 ridge region is similar to the direction measured for the field on a larger scale using optical polarimetry (see Figure 12 in Hildebrand et al. 1994); (ii) the magnetic field in the OMC-1 ridge is perpendicular to the ridge; and (iii) the magnetic field in the molecular bar

region is distorted from the overall field. This picture of the magnetic field structure is consistent with the uniform magnetic field in the OMC-1 cloud being a simple compression of the external large scale field, where the contraction of the OMC-1 cloud has been predominantly in the direction of the magnetic field lines. The distortion in the molecular bar could be due to pressure on the cloud by the foreground HII region. The HII region compresses the field into the OMC-1 cloud; from our perspective, this compression maintains the uniformity of the field behind the HII region, but distorts the field in the OMC-1 cloud to the south of the HII region where the cloud is being compressed perpendicularly to our line-of-sight. In Section 3, we will look at this picture more quantitatively.

Figure 3 shows an outline of the OMC-1 cloud with the polarization vectors of Figure 2 rotated by 90 degrees to represent the mean direction of the magnetic field on the plane-of-the-sky. In the north region of the map, magnetic field lines have been sketched to give a probable field configuration. Here it can be seen that the magnetic field lines have been bent towards the dense BN-KL region in a way predicted by Mouschovias (1976) for a cloud which is initially spherical and contracting in the presence of a uniform
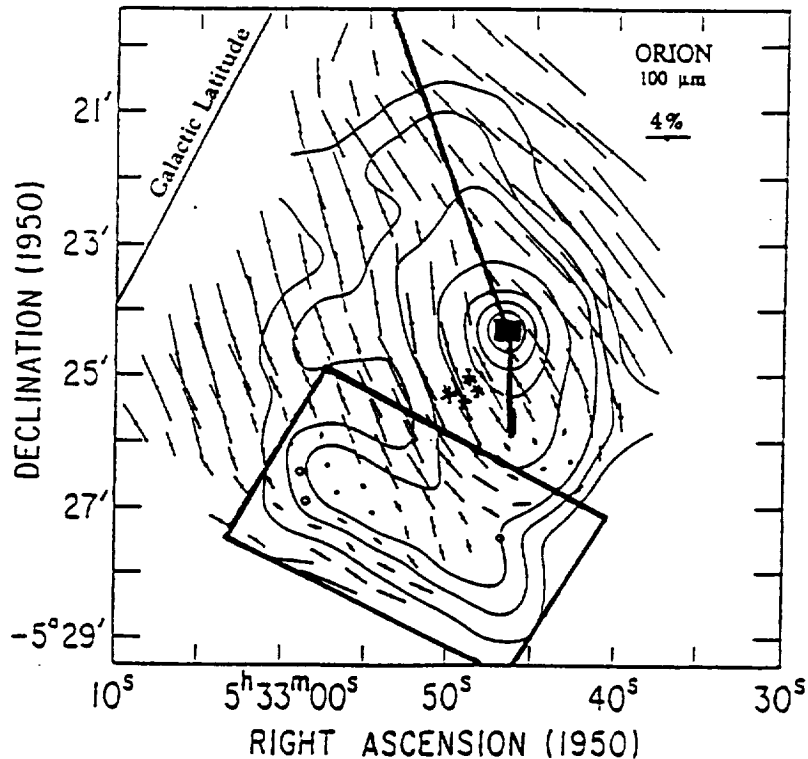

Figure 2. Our far-IR flux and polarization map of the M42/OMC-1 region. Vectors show the direction and degree of polarization. Also shown are the locations of the OMC-1 ridge (solid line), the BN-KL high-mass star formation region (solid square), the Trapezium Cluster (four stars), and "the molecular bar" (rectangle).
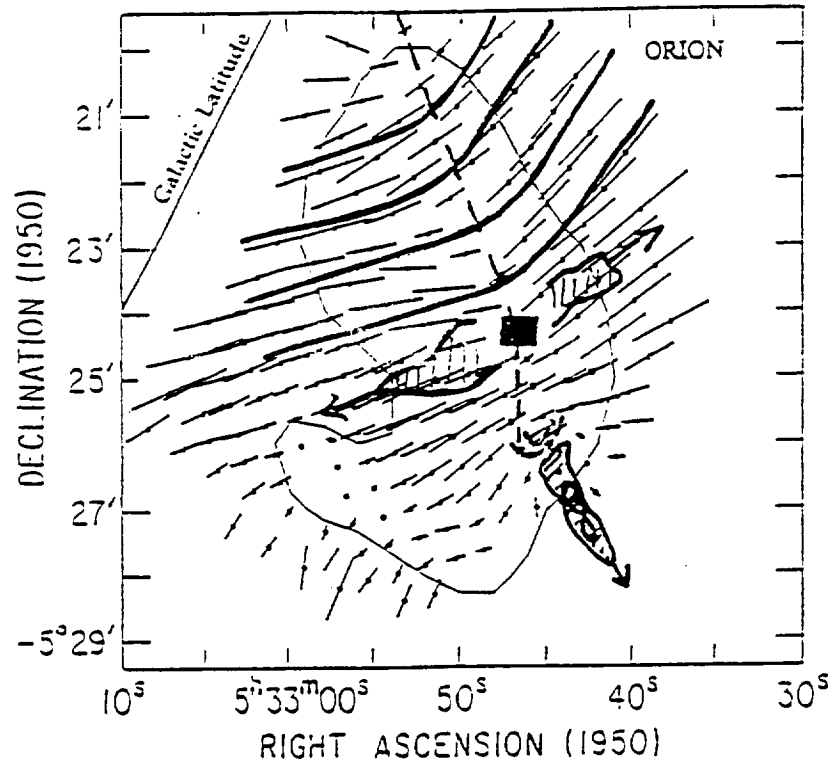
Figure 3. An outline of the OMC-1 cloud with the polarization vectors of Figure 2 rotated by 90 degrees to represent the mean direction of the magnetic field on the plane-of-the-sky. Probable magnetic field lines are sketched in the north. Also sketched are two observed outflows.

magnetic field until field gradients and distortion halts further contraction in the outer regions. Also shown in Figure 3 are the outflows observed in the OMC-1 region.

2.2 W3

W3, W4, and W5 form a chain (~ 240 pc long) of HII regions and clouds in the Perseus Arm of the Galaxy about 2.4 Kpc from our sun. This chain lies in the plane of the Galaxy. Optical polarization measurements imply that the magnetic field in this region of the Galaxy, on scales greater than 5 degrees, is aligned with the projection of the Galactic plane. Based on the molecular line work of Lada et al. (1975), it would seem that the well-developed, large H II region of W4 has expanded into the molecular cloud of W3, causing sequential high-mass star formation at the interface. Figure 4 shows our 100 μm photometry and polarimetry of a section of this interface, commonly designated W3, where the HII region of W4 lies to the east and the undisturbed cloud of the W3 region lies to the west of the region shown. Based on the vectors in Figure 4, one observes that: (i) the magnetic field lines

in this region are, on average, highly inclined to the plane of the Galaxy and, therefore, to the large scale magnetic field in the region; and (ii) the magnetic field within the region shown in Figure 4 is highly distorted. A possible explanation for the large inclination to the Galactic plane is that the H II region of W4 has pushed the ambient magnetic field into the overall configuration seen in Figure 4, a situation similar to the molecular bar in OMC-1. The distortion may be caused by gravitational or rotational effects, by expansion of internal H II regions, or by random turbulence generated by outflows. All of these potential causes of distortion are present in this part of W3, where at least 5 high-mass star formation sites are located. It should be noted that at the distance of W3, the M42/OMC-1 region shown in Figure 2 would occupy only a 1'x1' area. It is too early in our analysis to say which cause of distortion is dominant.

Figure 4. Our far-IR flux and polarization map of W3. Vectors show the direction and degree of polarization. Also shown is the direction of constant Galactic latitude.

3. Discussion

To quantify the qualitative scenario presented for M42 in Section 2.1, we must first estimate the magnetic field strength. There is no theory which can relate the degree of polarization to field strength; too many competing effects are involved (see Hildebrand 1988). However, an estimate of the strength of the field can be obtained by comparing the level of distortion in the direction of polarization to the forces known to be present. Distortion can be random

or systematic. Systematic distortions are caused by large scale forces such as gravity or H II shock fronts; random distortions are forces on the small scale such as turbulence. Chandrasekhar & Fermi (1953) were among the first to analyze field distortions to provide information about magnetic field strengths. Their analysis assumed that if the magnetic field is frozen into the medium and if signals travel along the field lines at the Alfvén speed $V_A = B/(4\pi\rho)^{1/2}$, then a small velocity perturbation, ∂V, perpendicular to the field lines will distort the field lines so as to produce a small transverse magnetic component, ∂B, satisfying : $\partial B/B = \partial V/V_A$. Here $\partial B/B$ can be obtained from the angular deviation, $\partial\phi$, of the magnetic field, or of the direction of polarization. If ∂V is random, as in turbulence, the above relation can be averaged over a number of data points and an estimate of the magnetic field given by

$$B = (<\partial V^2>/<\partial\phi^2>)^{1/2}(4\pi\rho)^{1/2},$$

where B is the strength of the total magnetic field, not just the field in the plane-of-the-sky. Before one can use this estimate, one must subtract the systematic distortions from the random. We have not yet done this in a sophisticated way, but the magnetic field lines sketched in Figure 3 crudely trace a likely systematic distortion in the magnetic field lines in the north. If we assume that along the ridge the field lines should be perpendicular to that ridge (as drawn), then deviations from this could be attributed to random forces such as turbulence. We selected the data points along the ridge, north of BN-KL, and found $(<\partial\phi^2>)^{1/2} \leq 5^\circ$ rms. Substituting this value into the above relation, and using

$$\Delta V_{FWHM}/(8\ln 2)^{1/2} \approx \sigma_{turb}= (<\partial V^2>)^{1/2} = 1.1\text{km s}^{-1}$$

and $n = 10^5$ cm^{-3} (values from Mundy et al. 1988 for the northern OMC-1 ridge), we calculate an estimate for the magnetic field strength of approximately 3 mG. There is a caveat to this estimate, however: Zweibel (1990) argued that if a cloud is clumpy, where the clumps are dense and small so that ambipolar-diffusion has occurred leaving them untied to the cloud's magnetic field lines, but the motions of the unresolved clumps contribute significantly to the velocity dispersion measured for the cloud, then the estimate given above could be a gross overestimate.

Is 3 mG consistent with available Zeeman measurements? Troland, Heiles, & Gross (1989) have measured the Zeeman Effect in the 21 cm absorption line of H I towards M42. Their measurements covered the area shown in Figure 2 and were made with comparable beam sizes. Based on their measurements, they determined the strength of the magnetic field along the line-of-sight in the 400 cm^{-3}, H I gas, which lies just in front of the H II region of the Trapezium stars, to be about 70 μG. The value of the field strength for this foreground gas in the plane-of-the-sky is unknown, but if we assume it to be similar to that along the line-of-sight, then the total magnetic field strength is about 100 μG. If we assume a scaling law between gas density and magnetic field strength, $B/B_0 = (n/n_0)^\alpha$, and substitute the

measured magnetic field strengths with their corresponding gas densities for the OMC-1 and the HI regions, we find $\alpha = 0.6$. This value is just outside the range calculated by Mouschovias (1976) for cloud contraction with field lines frozen-in (i.e., 0.3 - 0.5). This could be the result of our estimate being too high or of forced contraction of OMC-1 in the direction perpendicular to its magnetic field lines by the expansion of the HII region in the foreground.

We can use the Virial Equation to see if the HII region in front of OMC-1 is capable of distorting the magnetic fields in the region:

$$(0.5)(d^2I/dt^2) = 2K + 2T + M + W + \text{Surface Terms},$$

where I is the generalized moment of inertia; K, T, M, and W are the kinetic, thermal, magnetic, and gravitational energies of the OMC-1 ridge region; and the surface terms are due to thermal, kinetic, and magnetic forces acting on the surface of OMC-1 from the HII region. Here we have approximated:
$2K \approx 3M_r\sigma_{turb}^2$; $2T \approx 3M_rc_s^2$; $2M \approx M_r V_A^2$; $W \approx -G M_r^2/R_r$; and

Surface Terms $\approx -[P_{HII} + B_{HII}^2/24\pi](4\pi R_r^3)$. In these expressions M_r and R_r are the mass of the OMC-1 ridge and its radius, and P_{HII} and B_{HII} are the gas pressure and magnetic field in the H II region. Using probable parameter values for the HII and OMC-1 regions as summarized in Genzel and Stutzki (1989) and Mundy et al. (1988), and our own estimates of the magnetic field strength and scaling law, we find that : (i) Within the OMC-1 ridge, the kinetic plus thermal terms are approximately equal and opposite the gravitational term and, therefore, cancel; and (ii) the magnetic term in the OMC-1 region is an order of magnitude greater than any other term except for the surface term, which within an uncertainty of three can be considered equal. These two results imply that magnetic fields are dynamically important, and that they have severely decreased the star formation rate in OMC-1, both by preventing gravitational collapse and by preventing the HII region from more severely compressing the molecular cloud.

4. Summary

The analysis of the far-IR polarimetry results presented here is only of first order. A more thorough analysis will improve the accuracy of the strength estimated for the magnetic field in OMC-1 (as well as in other clouds summarized in Hildebrand et al. 1994) by: (i) better separating random from systematic field distortions (e.g. Myers & Goodman 1991); and (ii) better determining which velocities are associated with the random motion of the gas tied to the magnetic field lines (as argued in Zweibel 1990). In addition, our maps of the magnetic field structure can be used to model probable magnetic field configurations, and thus better estimates of the dynamical importance of the magnetic fields in these clouds can be obtained using the magnetic tension term as well as the pressure term in the force equation of the gas in the clouds.

If one accepts our first order analysis at face value, however, then in summary: (i) the magnetic field - density law in M42/OMC-1 seems to be somewhat steeper than predicted by Mouschovias (1976), possibly because of the compression due to the HII region in the foreground of OMC-1; (ii) the

deformation of magnetic field lines by HII regions could also explain the large and small scale magnetic field configurations in W3, where the field lines in the HII region/W3 cloud interface are highly inclined to those of the large scale field in that region of the Galaxy, and the fields within W3 are distorted where there are embedded HII regions around YSOs; and (iii) the magnetic fields in M42/OMC-1 may well be dynamically important, being a major regulator of star formation, in that clumps within OMC-1 must wait for ambipolar-diffusion before further collapse can occur.

The measurement of magnetic fields in the dense ISM is a young study where measurements on large as well as small scales are still required. In the future, observations must include complementary far-IR and sub-mm polarimetry measurements, so that warm and cold regions along a common line-of-sight can be disentangled (recall the situation in NGC2024). In addition, future Zeeman measurements must use molecules which trace the more dense ISM than heretofore, in order to determine the structure and strength of the field in the line-of-sight of dense star formation regions, studies which will complement far-IR and sub-mm polarimetry of these same regions. And finally we look forward to more sensitive telescopes, which will enable the above studies to be extended to low-mass star formation regions.

References

Genzel, R., & Stutzki, J. 1989, Ann. Rev. Astr. Ap., 27, 41

Gonatas, D. P., et al. 1990, ApJ, 357, 132

Hildebrand, R. H. 1988, Q.J.R.Astr.Soc. 29, 327

Hildebrand, R. H., Dotson, J. L., Dowell, C. D., Platt, S. R., Schleuning, D., Davidson, J. A., Novak, G. 1994 in Proc. of the Airborne Astronomy Symposium on the Galactic Ecosystem: From Gas to Stars to Dust, eds. M. Haas, J. A. Davidson, and E. F. Erickson, (A.S.P. Conf. Series), paper 111

Lada, C. J., Elmegreen, B. G., Cong, H. L., & Thaddeus, P. 1975, ApJ, 226, L39

Maddalena, R. J., Morris, M., Moscowitz, J., Thaddeus, P. 1986, ApJ, 303, 375

Mathewson, D. S., & Ford, V. L. 1970, Mem. R. Astr. Soc., 74, 139

Mezger, P. G., Chini, R., Kreysa, E., Wink, J. E., & Salter, C. J. 1988, A&A, 191, 44

Mouschovias, T. C. 1976, ApJ, 207, 141

Mouschovias, T.C., & Paleologov, E. V. 1980, ApJ, 237, 877

Mundy, L. G., Cornwell, T. J, Masson, Scoville, N. Z., C.R., Baath, L. B., & Johansson, L. E. B. 1988, ApJ, 325, 382

Myers, P. C., & Goodman, A. A. 1991, ApJ, 373, 509

Parker, E. N. 1966, ApJ, 145, 811

Platt, S. R., Dotson, J. L., Dowell, C. D., Hildebrand, R. H., Novak, G., & Schleuning, D., 1994 in Proc. of the Airborne Astronomy Symposium on the Galactic Ecosystem: From Gas to Stars to Dust, eds. M. Haas, J. A. Davidson, and E. F. Erickson, (A.S.P. Conf. Series), paper 707

Pudritz, R. E., & Norman, C.A. 1983, ApJ, 274, 677

Shu, F. H., Adams, F. C., & Lizano, S. 1987, Ann. Rev. Astr. Ap., 25, 23

Thronson, H. A., Lada, C. J., Schwartz, P.R., Smith, H. A., Smith, J.,
    Glaccum, W., Harper, D. A., & Loewinstein, R. F. 1984, ApJ, 280, 154
Thronson, H. A., et al. 1986, A.J., 91, 1350
Troland, T. H., Heiles, C., & Gross, W. M. 1989, ApJ, 337, 342
Zweibel, E. G. 1990, ApJ, 362, 545

The Magnetic Field Structure in the Galactic Center

Jacqueline A. Davidson

SETI Institute, NASA Ames Research Center. MS 245-6, Moffett Field, CA 94720. USA

Abstract. We review the present understanding of the magnetic field structure in the central 200 pc of our Galaxy as revealed through far infrared and radio polarimetry with the emphasis placed on far infrared polarimetry. This review will serve to illustrate the important contribution polarimetry makes to the study of magnetic fields in our Galaxy.

1. Introduction

Most of this conference has been devoted to understanding the nature of interstellar dust grains and how these can be aligned to produce observable polarization. Although the alignment mechanism is by no means certain at this point (see Draine 1996 and Roberge 1996 in these proceedings). we will assume in this paper that the spin axis of the largest moment of inertia of a dust grain is to some degree aligned with the magnetic field embedded in the medium being observed (probably either by the Davis-Greenstein mechanism or by ambipolar diffusion). And we note that in emission the resulting polarized E-vector from such a dust grain will be perpendicular to the local magnetic field direction. In this paper, armed with the above assumptions. we will review the magnetic field structure within the center of our Galaxy as probed by far infrared (FIR) polarimetry (see acknowledgements).

Heiles (1996) outlined the structure of the large scale magnetic field in the disk of our galaxy for radii greater than 5 kpc. These fields are found to lie basically in the plane of the Galaxy and seem to follow the Galactic spiral structure. Here we will review observations of the magnetic field structures within the central 200 pc of our Galaxy. Ultimately. the aim is to measure the magnetic field throughout the central 5 kpc so as to complete the picture of our Galaxy's magnetic field structure. Such an observational result would be very useful to test Galactic dynamo models. Our immediate aim in studying the magnetic field within the central 200 pc region, however. is to see how magnetic fields effect the energetics and dynamics at the very center of our Galaxy, and how these effects can be related to observations of Active Galactic Nuclei (AGN), where magnetic fields have been invoked to direct powerful galactic jets from massive black hole accretion disks.

The Magnetic Field Structure in the Galactic Center

Jacqueline A. Davidson

SETI Institute, NASA Ames Research Center, MS 245-6, Moffett Field, CA 94720

Abstract. We review the present understanding of the magnetic field structure in the central 200 pc of our Galaxy as revealed through far-infrared and radio polarimetry with the emphasis placed on far- infrared polarimetry. This review will serve to illustrate the important contribution polarimetry makes to the study of magnetic fields in our Galaxy.

1. Introduction

Most of this conference has been devoted to understanding the nature of interstellar dust grains and how these can be aligned to produce observable polarization. Although the alignment mechanism is by no means certain at this point (see both Draine and Roberge in these proceedings), we will assume in this paper that the spin axis of the largest moment of inertia of a dust grain is to some degree aligned with the magnetic field embedded in the medium being observed (probably either by the Davis-Greenstein Mechanism or by Ambipolar Diffusion). And we note that in emission the resulting polarized E-vector from such a dust grain will be perpendicular to the local magnetic field direction. In this paper, armed with the above assumptions, we will review the magnetic field structure within the center of our Galaxy as probed by far-infrared (FIR) polarimetry (see acknowledgements).

Heiles (in these proceedings) outlined the structure of the large scale magnetic field in the disk of our galaxy for radii greater than 5 kpc. These fields are found to lie basically in the plane of the Galaxy and seem to follow the Galactic spiral structure. Here we will review observations of the magnetic field structures within the central 200 pc of our Galaxy. Ultimately, the aim is to measure the magnetic field throughout the central 5 kpc so as to complete the picture of our Galaxy's magnetic field structure. Such an observational result would be very useful to test Galactic dynamo models. Our immediate aim in studying the magnetic field within the central 200 pc region, however, is to see how magnetic fields effect the energetics and dynamics at the very center of our Galaxy, and how these effects can be related to observations of Active Galactic Nuclei (AGN), where magnetic fields have been invoked to direct powerful galactic jets from massive black hole accretion disks.

2. Cloud Dynamics within the Central 200 pc

In order to understand the magnetic field structure within the central 200 pc it is necessary to study the gas motions in this region so as to: (1) obtain a three dimensional picture from two dimensional observations; and (2) determine possible field line distortions by gas motions, since it is assumed that the field lines are frozen into the gas. To understand the dynamical environment within the central 200 pc, it is necessary to look first at larger scales. Inside the central 5 kpc of the Galaxy, the Galactic plane orbits are determined by the mass distribution of the Galactic Bulge, Bar and Disk stars. The resulting orbits are not always circular. Calculations described in Binney et al. (1991) and Binney (1994) show that the circular orbits at 5 kpc, which connect smoothly with the orbits of the spiral disk, give way to unstable orbits of a Llindblad resonance between 5 to 2 kpc from the center of the Galaxy. For radii less than 2 kpc (the estimated length of the Galactic Bar) the orbits in the plane of the Galaxy are more elliptical than circular. For radii greater than 300 pc the major axis of the elliptical type orbits lie along the same direct as the bar, but for radii less than 200 pc the orbits have their major axis lying perpendicular to the length of the bar. For radii less than 100 pc the orbits are nearly circular again. The result is that cloud- cloud collisions should be quite common near a radius of 250 pc where the elliptical orbits with different major axis directions overlap. Such collisions could explain the relatively large number of clouds within the central 200 pc which do not follow Galactic orbits, but seem to have low angular momentum causing them to fall towards the Galactic center. In addition, recent observations by Uchida, Morris, & Bally (1994) show the possible existence of an expanding molecular ring, about 200 pc in diameter. The motion of the ring may have been generated by a powerful supernovea episode at the Galactic center about 10^6 to 10^7 years ago. This ring may also be responsible for cloud-cloud collisions causing angular momentum loss.

The central 200 pc region of the Galaxy was mapped by Odwenwald & Fazio (1984) in the FIR. This map shows a clumped but continuous distribution of FIR emission lying on the plane of the Galaxy stretching from Sgr B2 in the north to Sgr C in the south. Such emission blends together distinct clouds along the same line-of-sight which can be separated only by modelling velocity information from molecular/atomic line observations, as will be shown in later sections. Sgr A defines the Center of our Galaxy, about which most of the clouds are moving in near Galactic orbits, but there are numerous exceptions.

3. Magnetic Field Structure within the Central 200 pc based on Synchrotron Measurements

Figure 1 has been reproduced from Anantharamaiah et al. (1991) and is a 90 cm map of the region bounded by Sgr B2 just to the north (but excluded here) and Sgr C in the south. The intense 90 cm emission in the center of the map is Sgr A. The six filamentary features seen in Figure 1 have also been studied at other frequencies (Yusef-Zadeh, Morris, & Chance 1984; Liszt 1985; Morris & Yusef-Zadeh 1985; Bally & Yusef-Zadeh 1989; Gray et al. 1991), and are found to be non-thermal. In addition, Anantharamaiah et al. found that the synchrotron
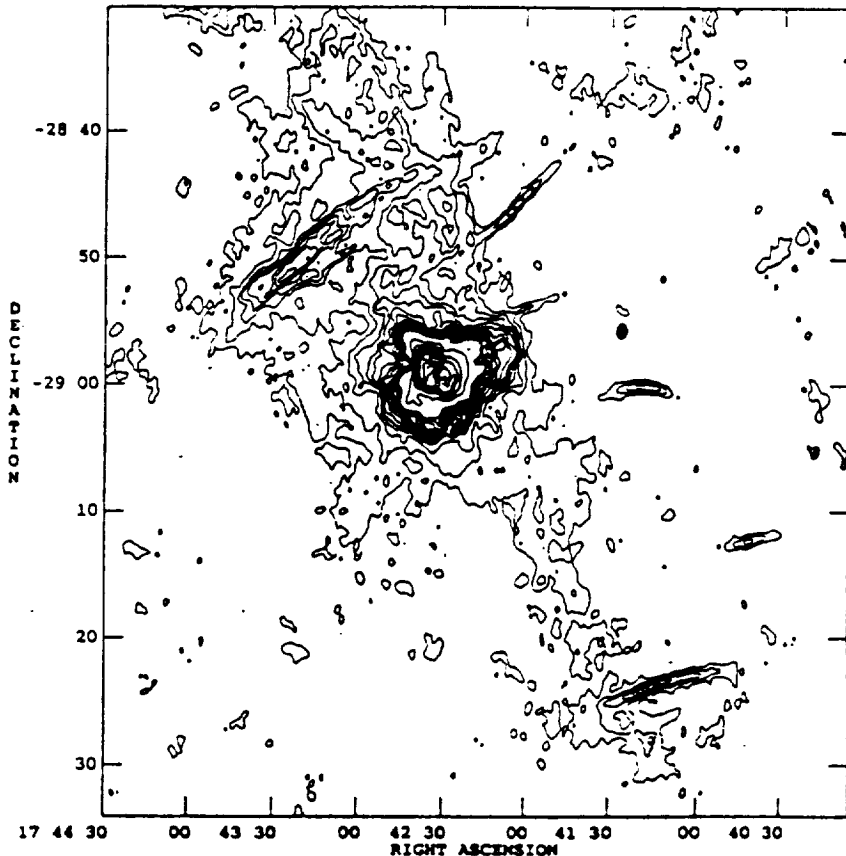
Figure 1. A 90 cm map of the central 200 pc of the Galaxy from Anantharamaiah et al. (1991).

spectra are flat ($\alpha = 0$ or slightly positive, where F_ν is proportional to ν^α) for some filaments but for others their spectra are more steep (α negative). This is consistent with a picture where sources of relativistic electrons lie close to the filaments with flat spectra, but that such sources have extinguished for filaments with steep spectra where the short-lived high energy electrons have decayed.

Radio polarization measurements corrected for Faraday rotation (Tsuboi et al. 1986) show that the non-thermal filaments are polarized with the magnetic field lines lying along them (i.e., perpendicular to the Galactic plane). The magnetic field strength within the filaments has been estimated to be on the order of a few mG, based on the observation that the filaments remain straight even in a region which has large intercloud velocity dispersions (Morris 1994). This estimation assumes cloud/filament interactions. Such an interaction seems evident in the case of the largest non-thermal filament called the Arc, and a cloud defined by thermal emission called the Sickle (or G0.18-0.04), which lies
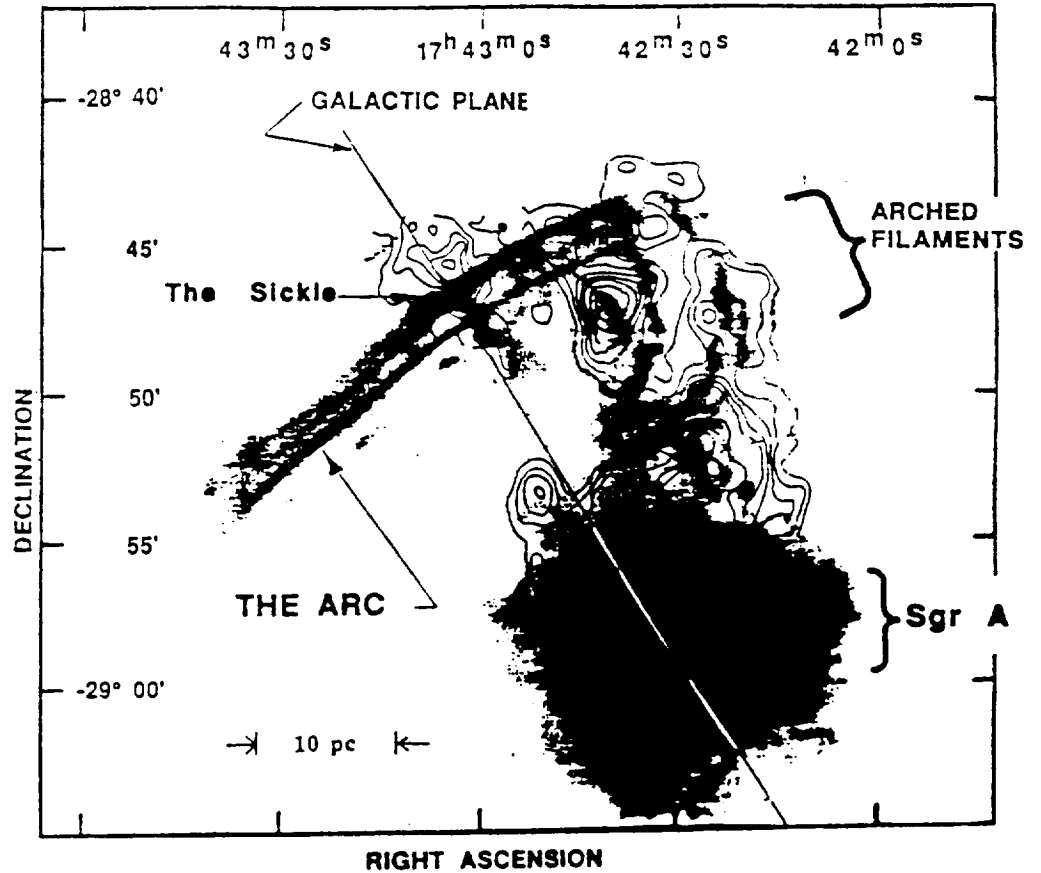
3

Figure 2. A 20 cm map of the Galactic Center Region by Yuseh-Zadeh, Morris, & Chance (1984), superimposed on contours of CS line emission by Serabyn & Güsten (1987) and (1991).

on the Galactic plane where the Arc intercepts the plane (Yuseh-Zadeh & Morris 1987; Serabyn & Güsten 1991; also see Figure 2).

Morris (1994) speculated that the poloidal magnetic fields measured in the filaments are pervasive throughout the central 200 pc and are only "illuminated" where there are sources of relativistic electrons. It is unclear, however, what could be the sources of the relativistic electrons. Such a pervasive field is probably anchored in the Galactic Halo or Bulge, because if it were anchored in the gas in the Galactic plane, as suggested by Shibata & Uchida (1987), there should be evidence for magnetic field line distortions in the filaments due to the azimuthal and radial velocities of Galactic plane clouds. If a poloidal field of about 1 mG does pervade the central 200 pc region then the magnetic energy within this central region, although not larger than the enclosed gravitational energy, equals both the cloud kinetic energy and coronal gas energy of the region (Morris 1994). Another speculation (Serabyn & Güsten 1991) is that the

4

filaments represent isolated flux tubes. This theory has the added difficulty, however, of having to explain a flux confining mechanism other than gas pressure, because the estimate magnetic pressure within the filaments far exceeds the gas pressure surrounding them. A further scenario, which is a hybrid of the above models, is one where the filaments lie in a compressed, cylindrical ring surrounding the Galactic center (Heyvaerts et al. 1988; Lesch et al. 1989), probably related to the 200 pc expanding ring. Such a geometry cannot be ruled out.

The poloidal magnetic fields observed in the synchrotron filaments lie in the diffuse gas. In this review we will examine the magnetic field structure in the dense gas in this central region of our Galaxy, using FIR polarimetry observations of two regions in particular, the Circumnuclear Ring about Sgr A* and the Arched Filaments which arch off the Arc above the plane of the Galaxy. The location of these two regions are shown on the 20 cm map of the central 50 pc region made by Yusef-Zadeh, Morris, & Chance (1984) and reproduced here in Figure 2. Unlike the 90 cm map of Figure 1, this figure clearly shows regions of thermal ionization as well as non- thermal. The Arched Filaments are thermal. In brief we will also mention two other dense regions in the central 200 pc, Sgr B2 and the Sickle, the latter also shown in Figure 2.

4. The Circumnuclear Ring around Sgr A* and the Northern Streamer

Most of the emission seen in Figure 2 for Sgr A is non-thermal and originates from Sgr A East, a supernova remnant, which lies close but behind the center of the Galaxy. The center of the Galaxy itself, known as Sgr A West, emits mostly thermal radiation except at its very center where the non-thermal source, Sgr A*, is located. Becklin, Gatley, & Werner (1982) discovered a ring of warm gas and dust surrounding Sgr A*. Later Güsten et al. (1987) measured this ring in the HCN (1-0) line and showed that its rotation was consistent with a Galactic orbit. The central cavity defined by the dust in the ring is about 2 pc (approx. 1') in diameter and the ring's outer dimension as defined by the HCN measurements is about 10 pc in diameter.

Figure 3a, b, and c shows a summary of 100 μm polarimetry results for Sgr A West from Werner et al. (1988), Hildebrand et al. (1990) and (1993). All observations were carried out on the Kuiper Airborne Observatory (KAO) using polarimeters from the University of Chicago. The first two sets of results were achieved with a single beam polarimeter, the last set was achieved using a 16 beam array polarimeter. The resolution improved over the three observation periods from 55" to 40" to 35". The position vectors (marking the direction of the E-vector) are superimposed on 100 μm photometry maps of Sgr A West which show the double peak signature of the ring surrounding Sgr A* (represented by a cross). The photometry maps are from Becklin, Gatley, & Werner (1982) and Davidson et al. (1992).

If taken at face value, all the position vectors are perpendicular to the Galactic plane which implies a magnetic field lying along the Galactic plane. This field is perpendicular to the poloidal field seen about 20 pc to the north in the Arc. However, since the ring is rotating (with a period of about 10^5 years),
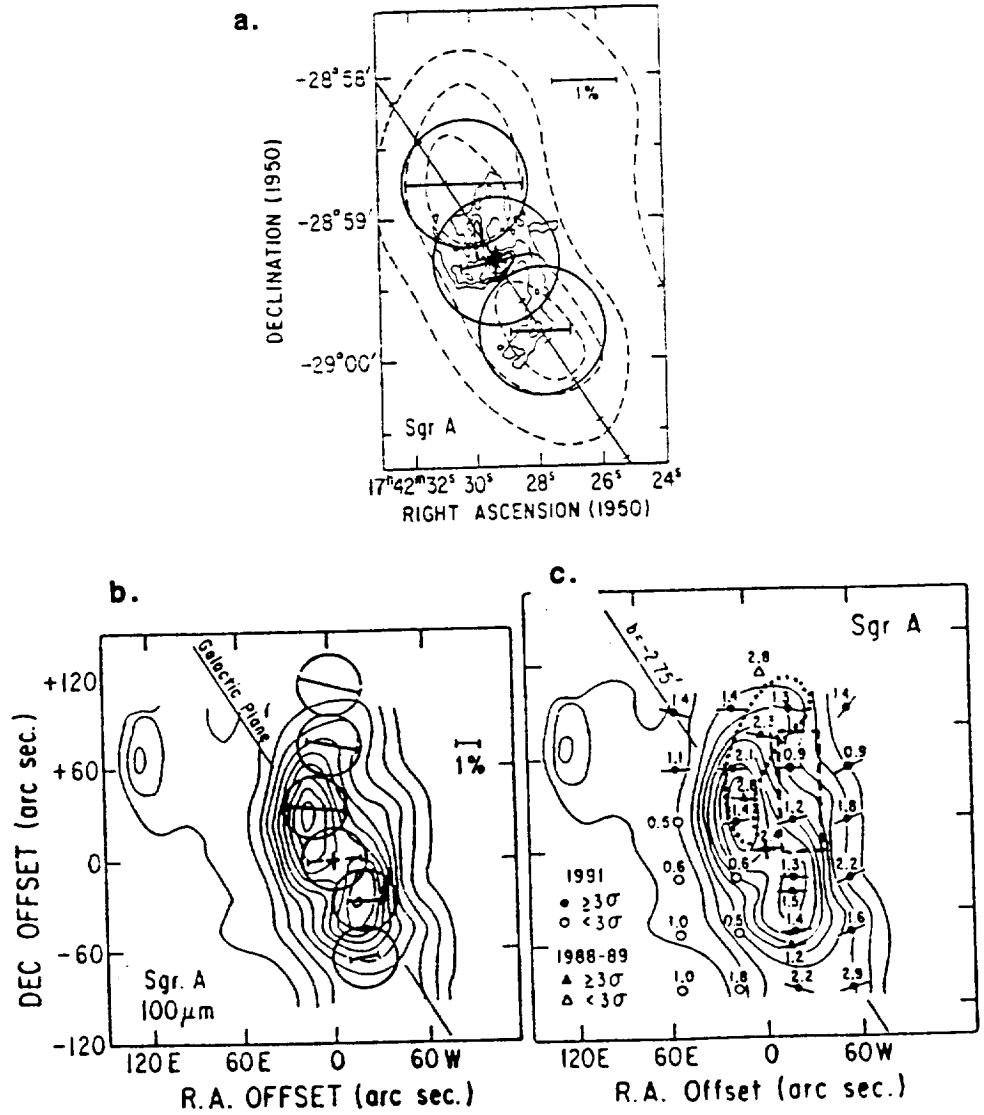
5

Figure 3. A summary of the FIR polarimetry results for the Circum-
nuclear Ring about Sgr A*. (a) is from Werner et al. (1988), (b) is
from Hildebrand et al. (1990), and (c) is from Hildebrand et al. (1993)
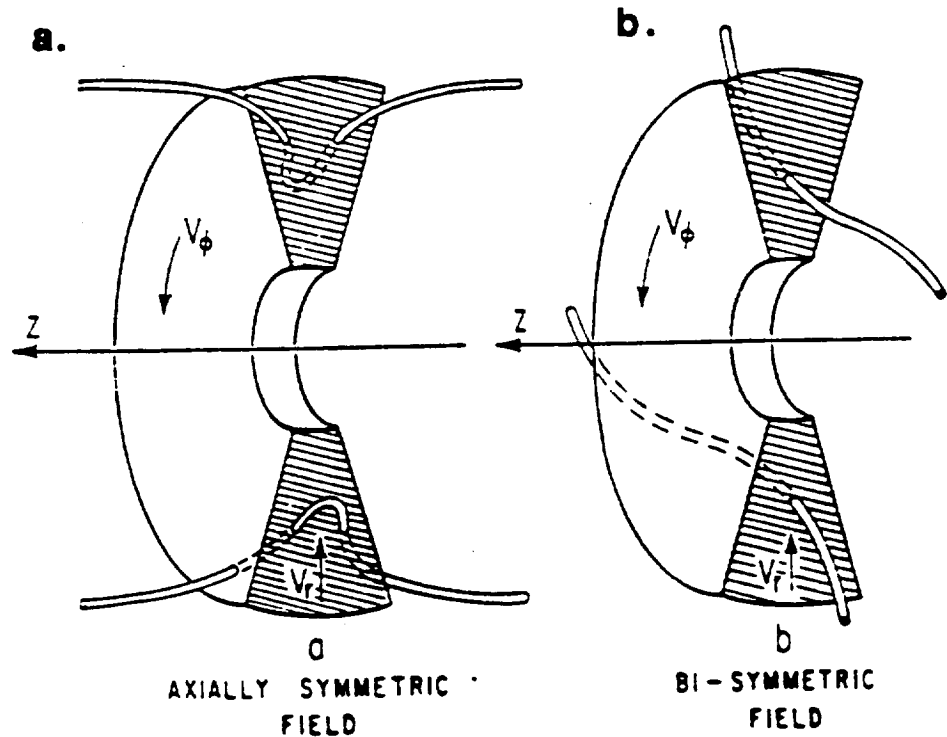(see text for details).

Figure 4.   Cross-section of the Circumnuclear Ring with axially symmetric and bi-axially symmetric magnetic field configurations.

a uniform field along the plane cannot be a solution if the field lines are frozen into the gas motion. There are two possible magnetic field structures:

1. The magnetic field was originally perpendicular to the plane of the Galaxy and was then advected into the ring by accretion and distorted so as to lie along the plane of the Galaxy within the ring (Hildebrand et al. 1990 and 1993, see Figure 4a). This structure has axial symmetry.

2. The magnetic field was originally parallel to the plane of the Galaxy and was then "wound-up" into a spiral or toroidal field within the ring (Werner et al. 1988, see Figure 4b). This structure has bi-axial symmetry.

Hildebrand et al. (1993) examined both these possibilities and found that the first symmetry is far more consistent with the data. The model chosen by Hildebrand to test for axial symmetry was that of Wardle & Königl (1990). This self-similar model assumes the ring about Sgr A* is a neutral, homogeneous, accretion disk, threaded by open advected poloidal field lines, which are distorted until ambipolar diffusion occurs. It also assumes that the ring is thin and is inclined so that it's long axis on the sky is nearly north-south and that its rotation axis is about 70 degrees or (180 - 70) degrees to the line-of-sight; an assumption justified by observations. Using this model, Wardle & Königl were

able to calculate the angle of the polarization position vector at each point on the sky, averaged within a 45″ beam, assuming uniform grain alignment throughout the ring. The absolute degree of polarization was not determined, only the 3-dimensional direction of the position vector (i.e., the relative degree of polarization as viewed from Earth). Since the model is self-similar, the resulting polarization position vector does not change with radius along a radial direction except for beam effects near the origin. Exploiting this fact, Hildebrand et al. (1993) plotted the position angle of the polarization vectors against the angle subtended by the position being considered on the ring, the center of the ring and the north axis, as measured in the counter-clockwise direction from the north axis. This representation is reproduced in Figure 5a, where the data are represented by squares or crosses and models from Wardle & Königl are represented by curves. Each curve represents a different ratio of B_z : B_θ : B_r, where B_z is the component of the magnetic field lying along the rotation axis of the ring (the direction of the large scale poloidal field), B_θ is the field component in the azimuthal direction of the ring, and B_r is the field component in the radial direction. Different conditions in the ring, lead to different degrees of ambipolar diffusion which in turn lead to different degrees of field line distortion because of rotation and accretion. Figure 5a shows that the best model of fit is "gc2" where $B_\theta > B_r > B_z$ in the ring.

A similar, but not self-similar, model was constructed by Hildebrand et al. for the bi-axial symmetry scenario shown in Figure 4b. In this model open planar field lines are advected and wound-up until ambipolar diffusion occurs (Parker 1979). If ambipolar diffusion is weak then the field lines become more and more toroidal. The data clearly show, however, that the field lines cannot be too toroidal, since the measured polarization does not vanish in the north and south of the ring where the field lines should be nearly parallel to the line of sight. In addition, OH Zeeman observations by Killeen, Lo, & Crutcher (1992) show the magnetic field strength along the line of sight to be about 2mG towards the observer in both the north and south regions of the ring. If the field were toroidal, there should be a direction change between these two regions. Hence, ambipolar diffusion must limit the amount by which the field lines are wound-up. Hildebrand et al. (1993) examined the case where the field lines form an S-shape within the ring. Figure 5b shows a plot of the predicted polarization angles for the model against the ring's polar angle on the sky as defined above for Figure 5a. Since this is not a self-similar model, there is a radial dependence, and this is represented by a number of curves, each representing the model for different radii. Also included for comparison are the measured polarization angles, each point given with its radius from Sgr A*. Figure 5b shows that the bi-axial model is not consistent with the data.

Actually, it must be stressed at this point that not all the data points shown in Figure 3c have been used in the comparisons between data and the models in Figure 5 a and b. In Figure 3c there are two regions which have been bounded, one with a dotted contour and one with a dashed contour. Both these probably contain considerable contamination from non-ring material along the line-of-sight, and so have been excluded from the above ring discussion. Based on HCN molecular line measurements of Güsten et al. (1987) and Jackson et al. (1993), and molecular H_2 line measurements by DePoy et al. (1989), the gas inside the dashed contour is probably not part of the ring since its velocity and
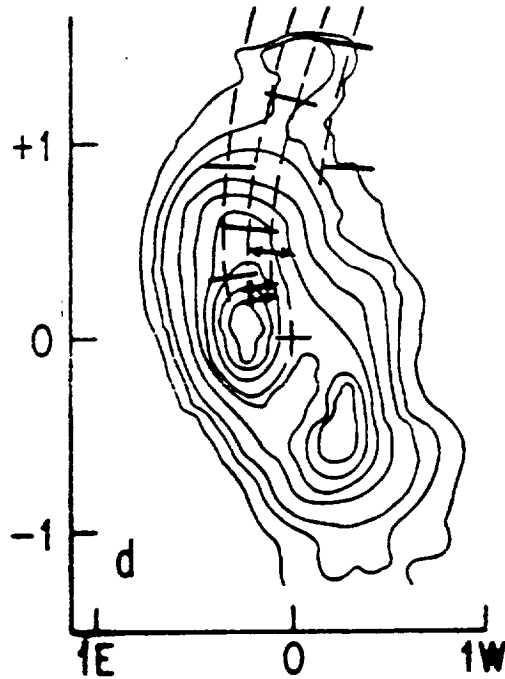
Figure 6.   100 μm polarization vectors of the Northern Streamer sup-
perimposed on a 50 μm map of the region, reproduced from Hildebrand
& Davidson (1994).

follow its curvature. This trend is followed down to small scales within the
cavity as shown by the 12.4 μm polarimetry results for Aitken et al. (1986)
and Aitken et al. (1991) (see also Rouche in these proceedings). Hildebrand &
Davidson concluded that the magnetic structure seen in this feature is probably
due to tidal shearing as the cloud falls towards the center.

   In short, to summarize the current thinking in regards to the magnetic field
structure in Sgr A West:

1. The field in the ring is unlikely to be toroidal or even the more general
   case where it is bi-axially symmetric.

2. The polarization data are consistent with an active accretion disk model
   with axial symmetry where $B_\theta > B_r > B_z$. Although this is not an
   excellent fit (either there is some distortion present or the model in Wardle
   & Königl is not correct in detail), it is true to say that the data are more
   consistent with an axial symmetric configuration than a bi-axial symmetric
   configuration.

3. In addition to the ring magnetic field structure, there is a streamer falling
   into the central cavity from the north, which seems to have sheared its
   internal magnetic field.

Before moving onto the Arched Filaments, we note here the work of Desch & Roberge in these proceedings. The Wardle & Königl model assumed uniform grain alignment with the embedded magnetic fields, but did not address the actual alignment process. But Desch & Roberge have reproduced polarization vectors consistent with the Hildebrand et al. data, based only on observables, the Wardle & Königl model for the magnetic fields, "gc2", assumptions of certain dust grain properties, and alignment by Ambipolar Diffusion. Their result shows that grain alignment by Ambipolar Diffusion is a very real possibility in the Circumnuclear Ring where strong ambipolar diffusion is taking place, at least in the Wardle & Königl model.

5. The Arched Filaments

The 20 cm radio image of the central 50pc region of the Galaxy (shown in Figure 2) clearly shows the non-thermal Arc north of Sgr A. Seemingly branching off from the Arc are a set of thermal, fleecy filaments called the Arched Filaments, whose source of ionization, thermal energy and geometric structure is unclear. Infrared and radio emission is consistent with excitation from a large number of embedded stars (Erickson et al. 1991), however, the structure of these filaments hint that stellar excitation may not be the full explanation (Morris & Yusef-Zadeh, 1989).

Serabyn & Güsten (1987) found from CS (2-1) line observations that underlying the Arched Filaments is a cloud with an unexpected velocity for a cloud north of the Galactic center; it is blueshifted, counter to the Galactic rotational velocities in that region. Furthermore, the cloud has significant internal shearing since its northern regions have a predominant velocity of 0 kms^{-1}, which moves smoothly to -50 kms^{-1} in the south. The Arched Filaments were mapped at 90 and 50 μm by Davidson et al. (1994) from the KAO with about 25'' resolution. Their results show that the arched filament structure seen at 20 cm (see Figure 2) is also apparent in the FIR. However, a close comparison of the 20 cm, FIR, and CS maps of the region show a relative displacement of features. The interpretation by Serabyn & Güsten (1987) and Davidson et al. (1994) is that the ionized filaments are a surface phenomenon, with the FIR tracing the photodissociation region (PDR) beneath them and the CS molecular line tracing the cloud underlying the PDR region. Thus FIR polarimetry in this region would trace the magnetic field in the PDR of the Arched Filaments. Morris et al. (1992) and Morris, Davidson, & Werner (1995) reported on recent 100 μm polarimetry measurements of the Arched Filaments, and their results are reproduced in Figure 7 superimposed on the cartoon of the ionized filaments. These observations were made from the KAO using the University of Chicago, 32 beam, array polarimeter with 35'' beams. It is clear from this figure that the magnetic field (perpendicular to the E-vector) lies along the filaments and bends where they do. This gives rise to the question, does the magnetic field in the cloud play a role in defining, at least morphologically if not energetically, the filament structure of the ionized gas?

Using the arguments in Chandrasekhar & Fermi (1953), Morris et al. (1992) estimated the magnetic field strength within the dashed contour shown in Figure 7 by comparing the degree of uniformity of the polarization angles to the known
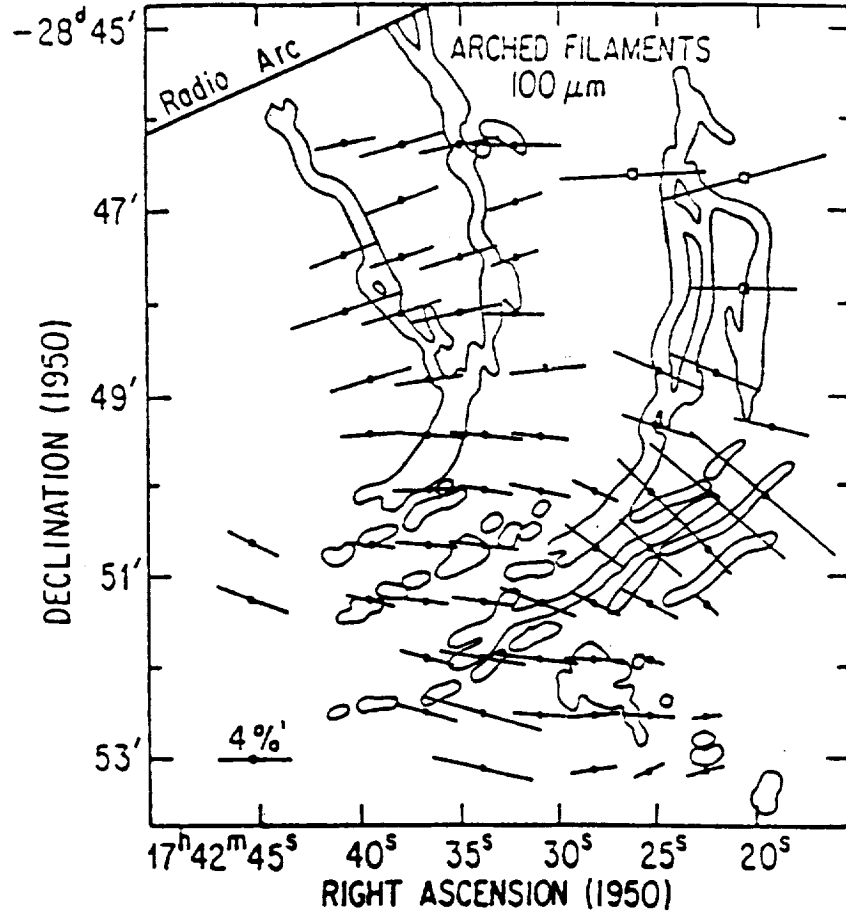
Figure 7. 100 μm polarimetry results on the Arched Filaments, reproduced from Morris, Davidson,& Werner (1995).

turbulence of the gas in which the magnetic fields are frozen. These arguments assume that if the field lines are frozen into the gas and signals travel along the field lines at the Alfvén speed, then a small velocity perturbation perpendicular to the field will distort the field lines so as to produce a small transverse magnetic component such that the ratio of the magnetic field distortion to magnetic field strength will be the same as the ratio of the velocity perturbation to the Alfvén velocity. If the turbulence is random and isotropic, then this relation can be averaged to give a relationship between the dispersion of the polarization angles, the turbulent velocity dispersion and the magnetic field strength (see Zweibel in these proceedings for more details). The failures of this argument have been discussed by Zweibel (Zweibel (1990) and Zweibel in these proceedings). Notwithstanding, we have used the Chandrasekhar/Fermi method here, because conditions are more favorable than usual for its use since:

1. The region is highly ionized, so flux freezing is likely;

2. The PDR of the Arched Filaments (traced in the FIR) is not deep (Erickson et al. 1991), so line-of-light effects which tend to average out the angular dispersion (see Jones in this proceedings) are kept to a minimum;

3. The magnetic field lines are likely to lie predominantly in the plane of the sky, since Uchida & Güsten (1995) have placed an upper limit to the line-of-sight field component of only a few tenths of a mG, based on their OH Zeeman measurements. This is only a tenth of the estimate for the total field strength (see below), hence, projection effects are minimal;

4. The filling factor based on CS and FIR measurements is quite high, so the effects of clumps on the Chandrasekhar /Fermi method are also minimal.

The averaged Chandrasekhar/Fermi relation gives a mean magnetic field strength of 6 mG inside the dashed contour in Figure 7, using the measured polarization angular dispersion for that region of 7 degrees, an average one dimensional gas velocity dispersion of 13 kms^{-1}, and a gas density of 10^4 cm^{-1}.

It is interesting to note that if this field strength is correct, then the bend in the filaments in the south-west section of the Arched Filaments represents a magnetic tension per unit volume which is comparable (and opposite) to the gravitational force per unit volume at that distance from the Galactic center. The bend, therefore, in the western filaments may be driven gravitationally. In addition, the filaments must be tidally unstable, having a gas density many times less than that required for stability. Thus the velocity structure of the filaments, their location, and their magnetic field orientation, imply the ionized Arched Filaments lie on the surface of a cloud falling into the Galactic center and is in the process of being severely sheared (Morris et al. 1992); a very similar case to that in the Northern Streamer within the Circumnuclear Ring surrounding Sgr A* (Hildebrand & Davidson, 1994). This transient picture of the filaments is further strengthened when one looks at various timescales of the region. The rotational period for the Galaxy at 20 pc from the center is about 10^6 yrs, the free-fall time for a cloud 20 pc from the Galactic center is about 10^5 yrs, and the Alfvén timescale for the magnetic field structure in the Arched Filaments is about 10^5 yrs. The latter timescale is just the ratio of the length of the filaments divided by the Alfvén velocity of the magnetic fields embedded within the filaments. This timescale gives an estimate of the lifetime of a particular magnetic structure. It would seem, therefore, that the structure known as the Arched Filaments will disappear within one rotational period of the Galaxy at 20 pc.

Although a consistent picture can be put together for the dynamics of the Arched Filaments, the same is not true for their energetics. Morris, Davidson, & Werner (1995) reported that the FIR luminosity of the filaments is $10^7 L_\odot$, and that the dust temperature along the filaments has a clumpy distribution but there is no evidence for a temperature gradient (see also Erickson et al. 1991). The average dust temperature along the filaments is about 50 K, between the filaments the dust temperature is below 40 K. The gas temperature in the PDR portion of the filaments, which is most likely traced by the FIR emission, is about 250 K (Erickson et al. 1991). Genzel et al. (1990) and Erickson

et al. (1991) argue that the observed ionization, luminosity and temperatures observed for the filaments are consistent with heating by early-type stars. However, the filaments' uniform temperature distribution requires either an unusual placement of these stars, or an extremely luminous cluster of such stars at least 10 pc away. Such a cluster has yet to be identified, but the cluster of emission stars found by Cotera et al. (1995) is an interesting possibility. Alternatively, there could be a magnetic origin to the luminosity and ionization, which would explain the observed morphology in a straight forward way. Two possible such processes which have been suggested so far are magnetic induction and magnetic reconnection. An MHD induction could arise if the cloud underlying the Arched Filaments impinges on the poloidal field (traced by the Arc) at a relative velocity. The cloud's kinetic energy to some degree could then be converted to the acceleration of ionized particles, further ionization through collisions, and then increased thermal energy through ohmic heating. An MHD reconnection process could arise if the non-parallel magnetic fields in the large scale poloidal field and the sheared magnetic field in the Arched Filaments reconnect at a rate proportional to the relative velocity of the two systems. The energy released is proportional to the magnetic field energy available for reconnection in the system. Unfortunately, as shown by Morris & Yusef-Zadeh (1989) and Morris et al. (1992), neither MHD induction nor reconnection can come close to obtaining the large luminosity observed, although such processes could explain the level of observed ionization.

6. The Sickle

Very recent (July 1995) FIR (60 μm) polarimetry observations of the Sickle (G0.18-0.04; Morris et al. private communication) show that the magnetic field in the Sickle runs along the ridge of the ionized gas, which is parallel to the Galactic plane. So here too, the magnetic field in a dense cloud is perpendicular to the field in the diffuse gas. This is puzzling at first, since the Sickle is quite obviously interacting with the Arc (Yuseh-Zadeh & Morris 1987; Serabyn & Güsten 1991). But Serabyn & Morris (1994) have proposed that this interaction could be the source of the accelerated elections along the Arc if there is sizable magnetic energy available for magnetic reconnection. The reconnection can result from either the fields in the Arc being distorted or the cloud underlying the Sickle being magnetized with fields non-parallel to the fields in the Arc. The observations support both scenarios: Either the field lines observed in the Sickle are the highly distorted lines from the Arc due to the ram pressure of the Sickle against the Arc, or they are the magnetic field lines intrinsic to the underlying cloud of the Sickle. In the former case the Sickle is like the Circumnuclear Ring about Sgr A*; a dense gas highly distorting the local poloidal field lines. In the latter case the Sickle is more like the Arched Filaments; a dense gas dragging its own distorted field lines from another part of the Galaxy.

7. Srg B2

There has also been polarimetry work on the cloud Sgr B2, which in projection lies approximately 120 pc north of Sgr A. Kane et al. (1993) measured two

locations on the ridge of Sgr B2 with 30″ resolution at 1.3 mm, and found position vectors approximately parallel to the Galactic plane, which would imply a magnetic field direction parallel to the poloidal fields. However, this may not be the case, since 100 μm polarimetry observations show that although the position vectors in the FIR are parallel to the Galactic plane on the ridge of Sgr B2, just off the ridge they are perpendicular to it (Novak, private communication; and Hildebrand et al. 1995). Very recently (July 1995), 60 μm polarimetry of Sgr B2 have shown higher polarization levels at 60 μm than at 100 μm for the ridge of Sgr B2 with position angles which agree (Dowell, private communication). This suggests that on the ridge, the polarization is due to absorption, not emission (Dowell et al., in preparation). This is perhaps not too surprising for the FIR, since Sgr B2 has an extremely high column density, but it is more difficult to believe for 1.3 mm observations. However, if polarization is due to absorption (even at 1.3 mm), then the magnetic field in the ridge of Sgr B2 is in the same direction as the field just off the ridge, that is parallel to the Galactic plane, not the poloidal field.

8. Summary and Future Studies

In short, the magnetic fields observed in the diffuse gas in the inner 200 pc of the Galaxy seem to lie perpendicular to the Galactic plane, whereas the fields measured in the dense gas of this region (e.g., the Circumnuclear Ring, the Northern Streamer, the Arched Filaments, the Sickle, and possibly Sgr B2) seem to lie almost parallel to the Galactic plane. In each of the dense gas cases (except Sgr B2), the field direction can be explained by a distortion due to gas motion. Either the magnetic field embedded in the gas is the local poloidal field distorted, or is a field dragged and distorted by the gas from another location. Conversely, it is also true to say that the gas motion in the Galactic center has been affected by the magnetic fields present: in the Circumnuclear Ring, the magnetic fields may be assisting gas accretion through angular momentum loss; in the Arched Filaments, the tension in the field lines may be preventing the underlying cloud from disintegrating through shear, and thus may be indirectly (if not directly) the cause of the strange energetics occurring in the filaments.

Much theoretical and observational work is yet to be done, before the overall magnetic field structure within the central 200 pc of our Galaxy is understood. But it can already be seen that there are certain properties in the gas/magnetic field interaction which may lead to AGN activity in a more energetic galactic nucleus than ours. And that certain elements of a dynamo are also present, with gas motions changing poloidal fields to fields with azimuthal components.

Sadly, with the closing of the KAO at the end of 1995, and its replacement, SOFIA (the Stratospheric Observatory for Infrared Astronomy), not flying until 2000, there will be little opportunity for further study of the magnetic field structure using FIR polarimetry until the next century. However, then there will be the possibility of FIR polarimetry with 3 times the spatial resolution and 10 times the sensitivity (more if the sensitivity of the polarimeters are also improved). This means much larger regions of the Galactic center can be mapped, with much better resolution. In addition, there are studies being prepared at present to use submillimeter (SMM) polarimetry. These studies will reveal the

structure of the magnetic fields in the cold components of the Galactic center clouds, whereas FIR polarimetry highlights the warm components of the clouds (see Hildebrand in these proceedings). One such study which will be of particular importance to the holistic study of the magnetic structure within the central 200 pc is the large-scale, SMM, polarimetry mapping of the central 200 pc, being planned using a telescope at the South Pole (see Novak in these proceedings). In addition, mid- infrared observations using large format arrays on large ground-based telescopes (see both Aitken and Rouch in these proceedings) will be able to study in detail many of the hot interaction regions discussed in this review, not only the Northern Streamer. Combining the Mid-Infrared, FIR, and the SMM polarimetry efforts will fill the gaps now in our picture, and show if some of our guesses are correct. For example, if the magnetic field in the Circum-nuclear Ring is indeed advected poloidal fields, then farther from the ring, one should start to see the position angles change to indicate a poloidal field.

References

Aitken, D,K., Rouche, P., Bailey, J., Briggs, G., Hough, J. & Gross, W.M. 1986, MNRAS, 218, 363

Aitken, D. K., Gezari, D., McCaughrean, M., Smith, C.H., & Rouche, P.F. 1991, ApJ, 380, 419

Anantharamaiah, K. R., Pedlar, A., ekers, R. D. & Goss, W.M. 1991, MNRAS, 249, 262

Bally, J. & Yusef-Zadeh, F. 1989, ApJ, 336, 173

Becklin, E. E., Gatley, I., & Werner, M. W. 1982, ApJ, 258,135

Binney, J. J, Gerhard, O. E., Stark, A. A, Bally, J., Uchida, K. I., 1991, MNRAS, 252, 210

Binney, E. E. 1994, in Nuclei of Normal Galaxies: Lessons from the Galactic Center, eds: R. Genzel & A.I. Harris, Dordrecht: Kluwer, 75

Chandrasekhar, S., & Fermi, E. 1953, ApJ, 118, 113

Cotera, A.S., Erickson, E.F., Simpson, J. P., Colgan, S. W. J., Allen, D. A., & Burton, M. G., 1995 in Proc. of the Airborne Astronomy Symp. on the Galactic Ecosystem: From Gas to Stars to Dust, eds: M. R. Haas, J. A. Davidson, & E. F. Erickson, San Francisco: ASP, 511

Davidson, J. A., Werner, M. W., Wu, X., Lester, D. F., Harvey, P. M., Joy, M. & Morris, M. 1992, ApJ, 387, 189

Davidson, J. A., Morris, M., Harvey, P.M., Lester, D. F., Smith, B., & Werner, M. W. 1994, in Nuclei of Normal Galaxies: Lessons from the Galactic Center, eds: R. Genzel & A.I. Harris, Dordrecht: Kluwer, 231

DePoy, D. L., Gatley, I., & Mclean, I.S. 1989, in IAU Symp. No. 136: "The Center of the Galaxy", ed: M. Morris, Dordrecht: Kluwer, 411

Erickson, E. F., Colgan, S. W. J., Simpson, J. P., rubin, R. H., Morris, M. 1991, ApJ, 370, L69

Genzel, R., Stacey, G. J., Harris, A. I., Townes, C. H.. Geis, N., Graf, U. U., Poglitsch, A., & Stutzki, J. 1990, ApJ, 356, 160

Genzel, R., Hollenbach, D. J., Townes, C. H., Eckart, A., Krabbe, A., Lutz, D., & Najarro, F. 1994, in Nuclei of Normal Galaxies: Lessons from the Galactic Center, eds: R. Genzel & A.I. Harris, Dordrecht: Kluwer, 327

Gray, A. D., Cram, L. E., Ekers, R. D., & Goss, W. M. 1991, Nature, 353, 237

Güsten, R., Genzel, R., wright, M. C. H., Jaffe, D. T., Stutzki, J., & Harris, A. I. 1987, ApJ, 318, 124

Heyvaerts, J., Norman, C., & Pudritz, R. E. 1988, ApJ, 330, 718

Hildebrand, R. H., Gonatas, D. P., Platt, S. R., Wu, X. D., Davidson, J.A., Werner, M.W., Novak, G., & Morris, M. 1990, ApJ, 362,114

Hildebrand, R. H., Davidson, J. A., Dotson, J., Figer. D. F., Novak, G., Platt, S. R., & Tao, L. 1993, ApJ, 417, 565

Hildebrand, R. H., & Davidson, J. A. 1994, in Nuclei of Normal Galaxies: Lessons from the Galactic Center, eds: R. Genzel & A.I. Harris, Dordrecht: Kluwer, 199

Hildebrand, R. H., Dotson, J. L., Dowell, C. D., Platt. S. R., Schleuning, D., Davidson, J. A., & Novak, G. 1995 in Proc. of the Airborne Astronomy Symp. on the Galactic Ecosystem: From Gas to Stars to Dust, eds: M. R. Haas, J. A. Davidson, & E. F. Erickson, San Francisco: ASP, 97

Jackson, J. M., Geis, N., Genzel, R., Harris, A. I., Madden, S., Poglitsch, A., Stacey, G. J., & Townes, C. H. 1993, ApJ, 402, 173

Kane, B. D., Clemens, D. P., Barvainis, R., & Leach, R. W. 1983, ApJ, 411, 708

Killeen, N. E. B., Lo, K. Y., & Crutcher, R. 1992, ApJ, 385, 585

Lesch, H., Crusius, A., Schlickeiser, R., & Wielebinski, R. 1989, A&A, 217, 99

Liszt, H. S. 1985, ApJ, 203, L65

Lo, K.Y., & Claussen, M. J. 1983, Nature, 306, 647

Morris, M., & Yusef-Zadeh, F. 1985, AJ, 90, 2511

Morris, M., & Yusef-Zadeh, F. 1989, ApJ, 343, 703

Morris, M., Davidson, J. A., Werner, M., Dotson, J., Figer, D.F., Hildebrand, R., Novak, G., & Platt, S. 1992, ApJ, 399, L63

Morris, M. 1994, in Nuclei of Normal Galaxies: Lessons from the Galactic Center, eds: R. Genzel & A.I. Harris, Dordrecht: Kluwer, 185

Morris, M., Davidson, J. A., & Werner, M. W. 1995 in Proc. of the Airborne Astronomy Symp. on the Galactic Ecosystem: From Gas to Stars to Dust, eds: M. R. Haas, J. A. Davidson, & E. F. Erickson, San Francisco: ASP, 477

Odwenwald, S. F., & Fazio, G. G. 1984, ApJ, 283, 601

Parker, E .N. 1979, Cosmical Magnetic Fields: Their Origin and Their Activity, Oxford: Clarendon Press

Serabyn, E. & Güsten, R. 1987, A&A, 184, 133

Serabyn, E. & Güsten, R. 1991, A&A, 242, 376

Shibata, K., & Uchida, Y. 1987, PASJ, 39, 559

Tsuboi, M., Inoue, M., Handa, T., Tabara, H., Kato, T., Sofue, Y., & Kaifu, N. 1986, AJ, 92, 818

Uchida, K., Morris, M., & Bally, J. 1994, in Nuclei of Normal Galaxies: Lessons from the Galactic Center, eds: R. Genzel & A.I. Harris, Dordrecht: Kluwer, 99

Uchida, K. & Güsten, R. 1995, A&A, in press

Wardle, M., & Königl, A. 1990, ApJ, 362, 120

Werner, M. W., Davidson, J. A., Morris, M., Novak, G., Platt, S. R., & Hildebrand, R. H. 1988, ApJ, 333, 729

Yusef-Zadeh, F., Morris, M., & Chance, D. 1984, Nature, 310, 557

Yusef-Zadeh, F., & Morris, M. 1987, AJ, 94, 1178

Zweibel, E. G. 1990, ApJ, 362, 545

AIRBORNE ASTRONOMY SYMPOSIUM ON THE GALACTIC ECOSYSTEM: FROM GAS TO STARS TO DUST

Edited by
Michael R. Haas, Jacqueline A. Davidson,
and Edwin F. Erickson

SOFIA: The Future of Airborne Astronomy

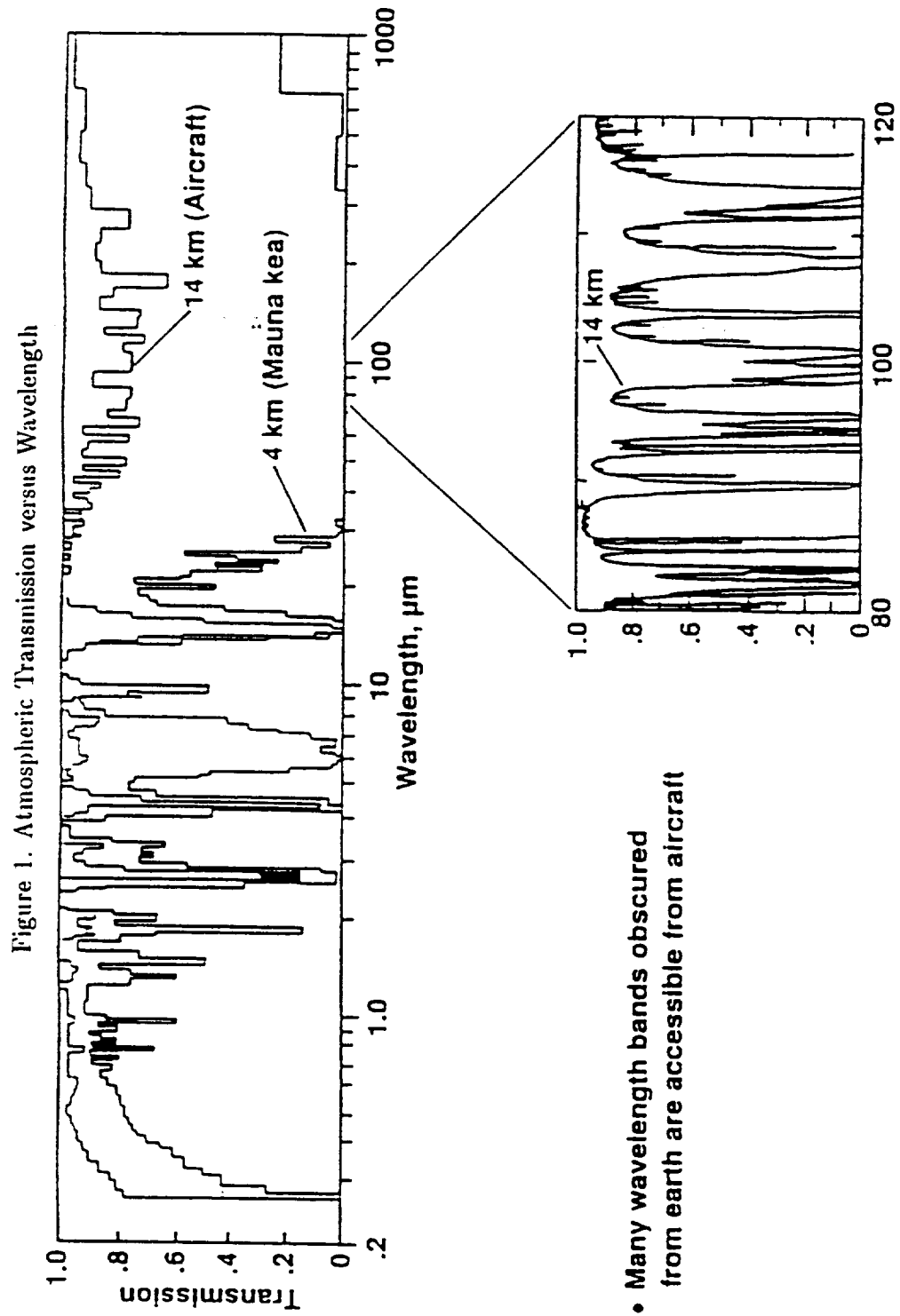E. F. Erickson *NASA/Ames Research Center, MS 245-6, Moffett Field, CA 94035-1000*

J. A. Davidson *SETI Institute; NASA/Ames Research Center, MS 245-6, Moffett Field, CA 94035-1000*

Abstract. For the past 20 years, the 91 cm telescope in NASA's Kuiper Airborne Observatory (KAO) has enabled scientists to observe infrared sources which are obscured by the earth's atmosphere at ground-based sites, and to observe transient astronomical events from anywhere in the world. To augment this capability, the United States and German Space Agencies (NASA and DARA) are collaborating in plans to replace the KAO with a 2.5 meter telescope installed in a Boeing 747 aircraft: SOFIA – The Stratospheric Observatory for Infrared Astronomy. SOFIA's large aperture, wide wavelength coverage, mobility, accessibility, and sophisticated instruments will permit a broad range of scientific studies, some of which are described here. Its unique features complement the capabilities of other future space missions. In addition, SOFIA has important potential as a stimulus for development of new technology and as a national resource for education of K-12 teachers. If started in 1996, SOFIA will be flying in the year 2000.

1. Airborne Astronomy – the Legacy

For nearly three decades astronomers have been making infrared observations from aircraft based at NASA's Ames Research Center in California. In 1965 Gerard Kuiper used the NASA Convair 990 to show that the clouds of Venus were nearly devoid of water, demonstrating the advantages of airborne observations in the near infrared. In 1968 the Ames Learjet was used by Frank Low to measure far infrared luminosities of Jupiter and Galactic nebulae. In 1974 the Kuiper Airborne Observatory (KAO) started its now 20 year career as a national facility for astronomy. Its users have produced ~ 1000 refereed publications, and ~ 50 Ph.D. theses for students at U.S. and foreign universities; it also supports kindergarten through high school teacher outreach programs. A good review of the KAO program and its contributions to science, education, and technology is given by Larson (1994).

Most infrared radiation from astronomical objects which never reaches the ground is detectable from the lower stratosphere. This fact is the principal justification for an airborne telescope. Figure 1 plots computed atmospheric transmission (Traub & Stier 1976) as a function of wavelength for aircraft (14 km) and mountain-top (4 km) altitudes. The absorption is largely due

Figure 1. Atmospheric Transmission versus Wavelength

• Many wavelength bands obscured
  from earth are accessible from aircraft

to water vapor, with significant contributions from carbon dioxide and ozone in some wavelength bands. The model assumes overhead water quantities of 2.3 μm for the aircraft and 1.2 millimeters for the ground-based telescope, and a zenith angle of 60 degrees. From 14 km, the broadband atmospheric transmission is adequate (≥70%) for photometric observations at most infrared wavelengths, but the emissivity limits detector sensitivity due to the fluctuations in the arrival rate of the photons from the sky. A number of the water lines in the far infrared are still saturated at aircraft altitudes, as shown in the lower panel. Between these lines the transmission can exceed 95%, the emissivity is correspondingly low, and so high resolution spectrometers can achieve sensitivity limited principally by the emission of the telescope.

Despite the numerous saturated atmospheric lines at aircraft altitudes, most important astronomical spectral features can be measured from an airborne observatory. To demonstrate this, we list in Table 1 the spectral features originating in the interstellar medium (ISM) which have been observed from the KAO. These features characterize important phases of material in the ISM: molecules, neutral and ionized atoms, and solids, as discussed in Section 3. A sample of the research done from the KAO is presented in this volume.

The extensive scientific and technical heritage of the airborne program, and particularly our experience with the KAO, provides a solid basis to project the performance and the design of the next generation airborne observatory − SOFIA.

2. Characteristics and Performance

SOFIA's characteristics are summarized in Table 2. The large aperture and wavelength range, routine accessibility to most infrared wavelengths, and mobility are unique features of the observatory (Caroff 1994). Relative to the KAO, SOFIA will be roughly ten times more sensitive for compact sources, enabling observations of fainter objects and measurements at higher spectral resolution. Also, it will have three times the angular resolving power for wavelengths greater than about 10 μm, permitting more detailed imaging throughout the far infrared.

The anticipated performance of SOFIA is indicated as a function of wavelength in Figures 2 through 5. Figure 2 shows the expected image quality, which is limited by seeing from the air flow over the telescope cavity at visible and near infrared wavelengths, and by diffraction at long wavelengths. The specified performance of the optical system limits the image quality in the ∼ 4−10 micron range. Figure 3 shows the anticipated photometric sensitivity per pixel, which is simply scaled from the performance achieved on the KAO. Here "PSC" and "FSC" refer to the IRAS Point Source and Faint Source Catalogues, respectively. We see that SOFIA would be able to observe any of the compact infrared sources in these catalogues. High resolution spectrometers are expected to be available for most of the wavelength range of SOFIA, as indicated in Figure 4. Interstellar lines are typically broadened to a km/sec or more, whereas higher resolving power can be useful for study of solar system objects. Spectroscopic sensitivity, shown in Figure 5, corresponds to the spectral resolving power shown in Figure 4. Narrow lines emitting more than 0.1% of the total continuum emission from the IRAS sources should be detectable. The important cooling lines of neutral

Table 1

INTERSTELLAR SPECTRAL FEATURES DETECTED FROM THE KUIPER AIRBORNE OBSERVATORY

DUST GRAINS

λ (μm)	SPECIES
2.95?, 6.3, 7.1 a	NH₃ Ice
5.2, 5.6, 6.2, 6.9, 7.6, 7.8	PAH
5.5 a	HCO in Ice
6.0, 62, 45 a/e	H₂O Ice
6.8 a	Hydrocarbon
19.0 a/e	silicate
24-30+	MgS (?)
45, 62 a/e	H₂O

ATOMS

λ (μm)	SPECIES
1.88, 2.62, 2.67, 2.76, 4.65, 5.91, 6.6, 7.5, 52.5	H I
3.1, 7.5	N II
4.5	Mg IV, Ar VI (?)
5.6	Mg V
6.6	Ni II
6.98	Ar II
7.63	Ne VI
8.99, 21.8	Ar III
17.9, 26.0	Fe II
18.7, 33.4	S III
22.9	Fe III
24.3	Ne V
25.2	S I
25.9	O IV
34.8	Si II
36.0	Ne III
51.8, 88.4	O III
57.3	N III
63.2, 146	O I
121.9, 205	N II
158	C II
158	¹³C II
370, 609	C I

MOLECULES

λ (μm)	SPECIES
1.4, 18 a	C₂
2.0, 2.6, 7.5 a	C₂H₂
2.3, 4.6, 77, 81, 87, 97, 100, 103, 119, 124, 153, 163, 174, 186, 200, 289, 302, 650	CO
2.9 a	C₂H
3.0, 3.5, 7.5 a	HCN
5.0 a	C₃
8.5	SiO
17.0	H₂
53.4, 84.4, 84.6, 119.3, 119.5, 149, 163.1, 164.4, 202 a/e	OH
154, 308	H₂CO
120.0, 120.2 a/e	H₂OH
125, 166, 524	NH₃
149.1, 149.4, 203	CH
479	HCl
790, 1600	H₂O
805	H₂D⁺

Almost all of these features were first detected from NASA's airborne observatories, and cannot be studied from ground-based sites. Features seen in absorption are indicated with "a", and seen in both emission and absorption with "a/e". Whereas the dust features typically originate in regions cooler than a few hundred degrees Kelvin, the various gaseous lines originate in regions ranging in temperature from $\sim 10^5$ K down to ~ 10 K. Thus these infrared spectral features characterize material in all phases of the interstellar medium: solid particles, molecules, neutral atoms, and ionized atoms.

Table 2
Summary of Basic SOFIA Characteristics

In-flight access to focal plane instruments – continuous
Vehicle – Boeing 747
Operating altitudes – 41,000 to 45,000 feet
Aircraft-limited duration at or above 41.000 feet $\gtrsim$ 5 hours
Nominal flight duration (crew-limited) – 7.5 hours
Research flights per year – ~ 160
Number of PI teams flown per year – ~ 60
Number of focal plane instruments flown per year – ~ 15
Frequency of science proposal peer review – annual
Stabilized telescope system weight – ~ 8,000 kg
Effective primary mirror diameter – ~ 2.5 meters
Wavelength range – 0.3 to 1600 microns
Telescope configuration – Nasmyth
Design f/ ratio – ~ 20
Design plate scale – 4 arcseconds/mm
Unvignetted field of view – 8 arcminutes
Telescope optical image quality $\lesssim$ 1 arcseconds
Shear layer seeing – ~ 3 arcseconds (0.3 to ~5 microns)
Diffraction-limited at wavelengths – $\gtrsim$ 10 microns
RMS pointing stability – $\lesssim$ 0.2 arcseconds
Telescope emissivity – $\lesssim$ 15%
Telescope elevation range – 20 to 60 degrees
Nominal operating optics temperature – ~ 250K

oxygen at 63 μm and C^+ at 158 μm from photodissociation regions are typically this strong relative to the continuum. Shocked interstellar gas will produce a higher line to continuum ratio.

3. Science

The infrared spectral regime encompasses a multitude of rich and varied physical processes and is uniquely suited for the study of cosmic birth on all scales. SOFIA will be an essential tool in many of these studies. Among the primary goals of SOFIA scientists is a detailed and comprehensive study of the processes which lead from cold clouds in the Interstellar Medium (ISM), through the formation and evolution of stars and planetary systems, to the eventual return of processed material to the ISM. Astronomers will also use SOFIA's superior spatial and spectral resolution to examine the dust and gas in the vicinity of our Galactic Center, to search for the signature of a massive black hole which may be the central powerhouse of the Galaxy, and to examine the origin of the massive stars observed there. On still larger scales, SOFIA will provide new understanding of global star formation in galaxies and the origin of the extraordinary luminosities of some infrared-emitting galaxies discovered by IRAS. In addition, the unique mobility of an airborne observatory
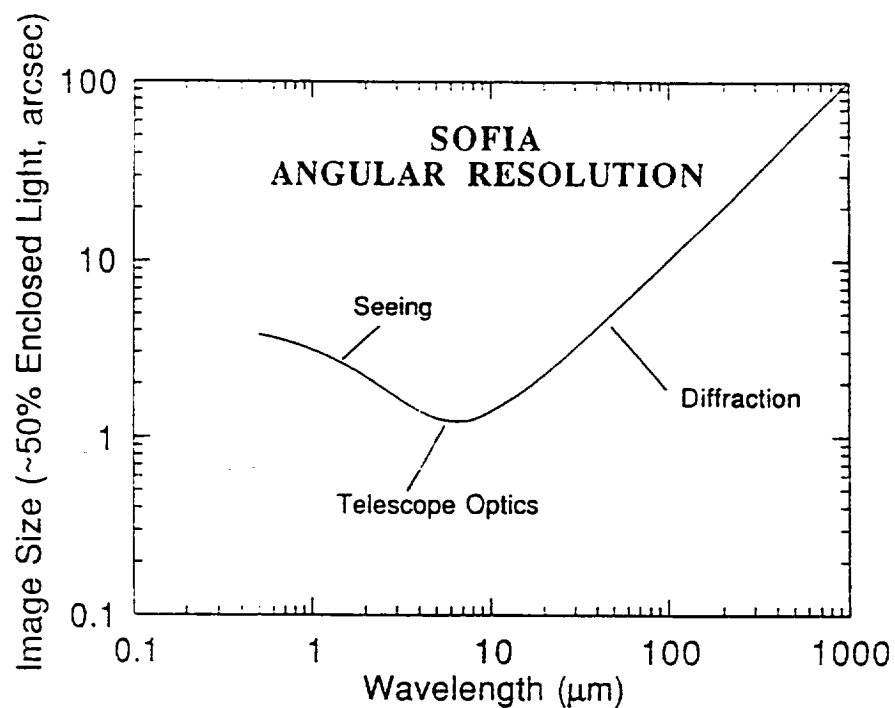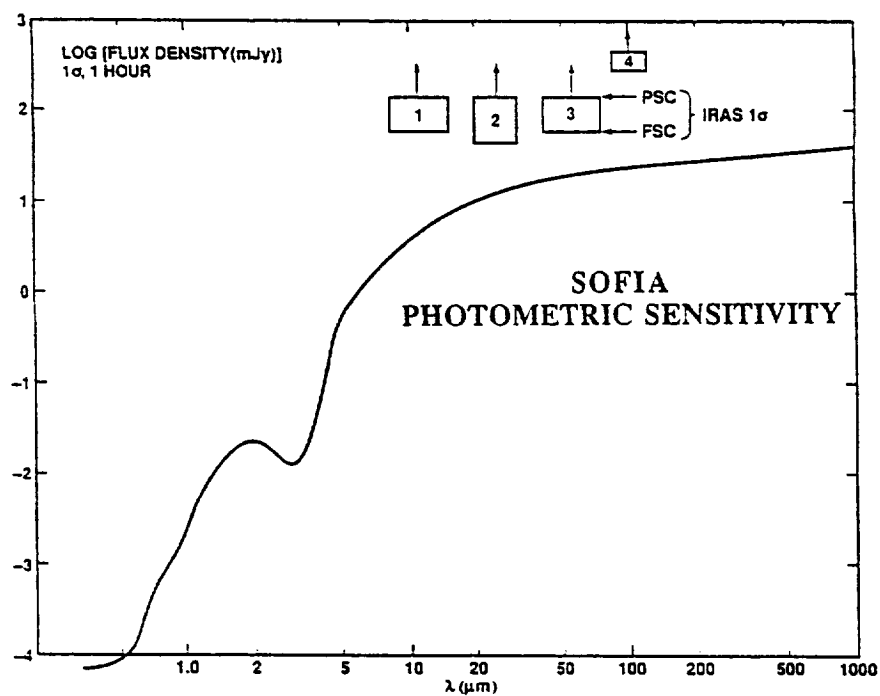
Figure 2. Anticipated image quality versus wavelength.

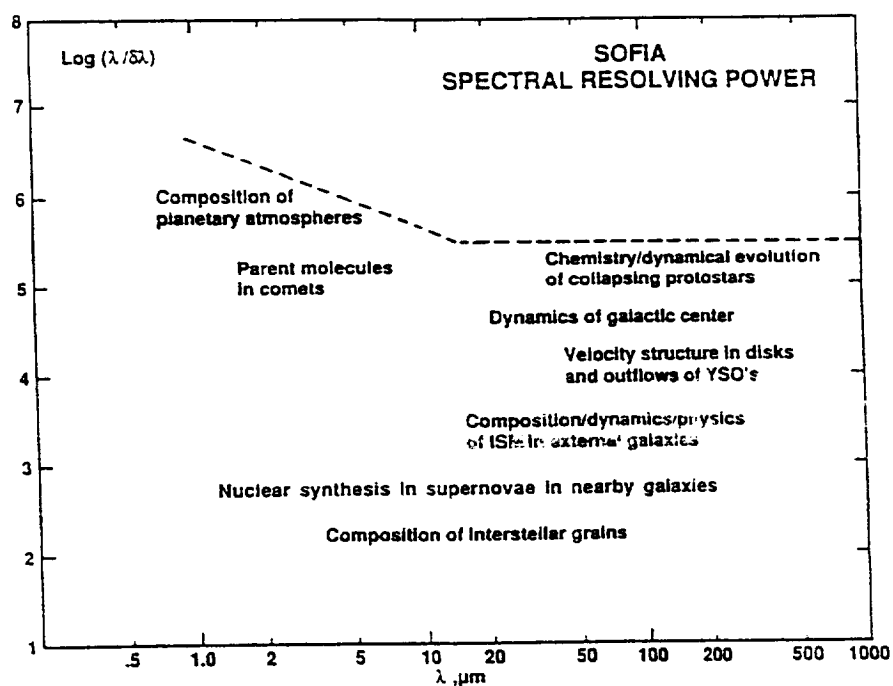Figure 3. Anticipated photometric sensitivity versus wavelength.

Figure 4. Anticipated spectral resolving power versus wavelength.
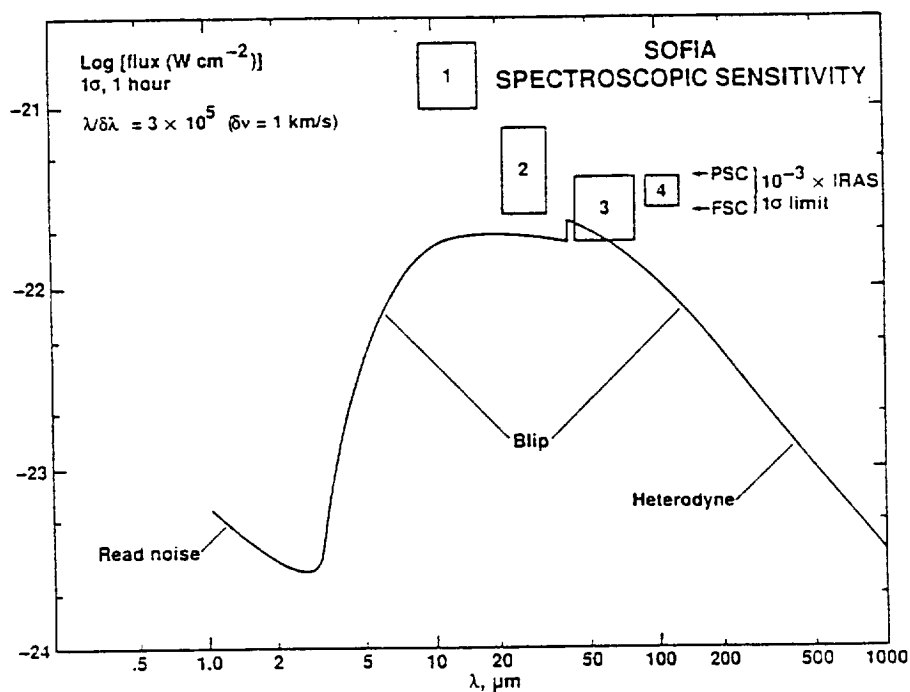

Figure 5. Anticipated spectroscopic sensitivity versus wavelength.

allows effective response to a number of highly localized and sometimes quite transient phenomena, such as solar eclipses, comets, novae, supernovae, and stellar occultations by solar system bodies. We discuss a number of specific examples below:

(i) The Interstellar Medium

All galaxies are permeated by an Interstellar Medium, but with properties which may vary greatly from galaxy to galaxy. Fundamental components of the ISM – solids, molecular gas, neutral atomic gas, and ionized gas – are characterized by infrared, far-infrared, or sub-millimeter emission and this emission generally dominates the cooling of the gas and dust. Observations of the ISM are critical to the study of the cycle of gestation, birth, evolution, and death of stars for the following reasons:

(a) The composition of the ISM determines the chemical makeup of the objects which form from it; (b) The structure, energy balance, and physical state of the ISM in a particular region determine the nature of subsequent evolution, for example in the formation of high mass versus low mass stars; (c) The structure and dynamics of the ISM, in turn, are strongly influenced by young stars which interact with the ISM via wind-driven shocks and ultraviolet radiation; and (d) Interesting phenomena are often embedded in dense, dusty regions of the ISM and can only be observed indirectly through the interaction of the source with the ISM. Therefore an understanding of the properties of the ISM is essential to interpret observations of the embedded sources correctly.

From SOFIA, astronomers would map the total and polarized thermal continuum from cool dust in molecular clouds with high spatial resolution, as well as the corresponding power radiated in atomic fine structure and rotational molecular lines. These measurements provide estimates of the density, luminosity, temperature, chemical and dust grain makeup, magnetic fields, dynamics, and detailed morphology of these regions.

Carbon chemistry is the basis of life as we know it, and has its beginnings in the ISM. Carbon emission lines also provide a large percentage of gas cooling in the ISM, thus altering the ISM environment and subsequent chemical evolution. Spectroscopy will yield particularly significant results on carbon chemistry in clouds, via
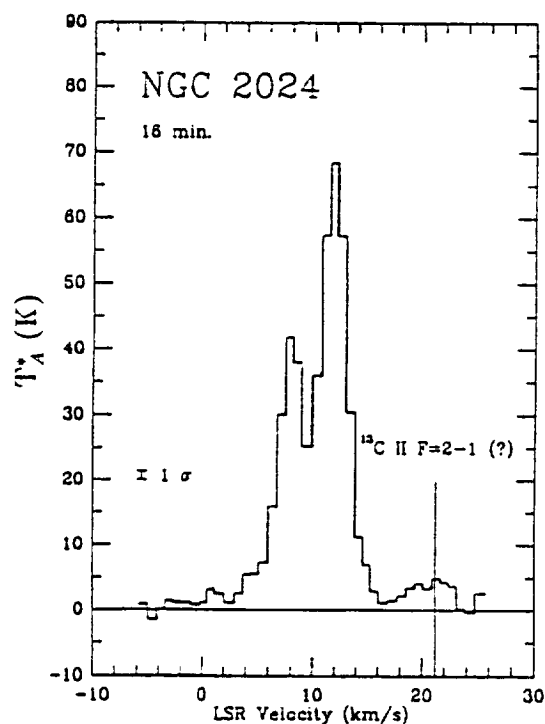

Figure 6. Velocity resolved spectrum of C^+ at 158 μm.

the 158 μm C$^+$ line, the 370 and 609 μm C lines, a host of FIR and submm rotational CO lines, and numerous near-infrared absorption lines of basic organic molecules such as CH_4, C_2H_2, and C_2H_4. As an example. Figure 6 shows a KAO measurement of the C$^+$ line from NGC 2024, a molecular cloud/ionized gas complex, obtained with a velocity resolution $\lesssim 1$ km/s. Line observations at such high spectral resolution provide information on systematic and turbulent motions within a cloud.

(ii) Star Formation

The ubiquitous associations of young stars with dark clouds clearly tells us that star formation occurs in dense regions of the ISM. The star formation process is not well understood. For example, it is not known why or when a region of a cloud will start to collapse. In order to form a one solar mass star, the collapse must extend to a radius of about 10^{17} cm in a quasi-stable dense clump in an interstellar cloud. This distance would correspond to just under an arcminute on the sky if we were observing the collapse in the nearest star formation region, the Taurus cloud, which is 160 pc away. SOFIA's ten arcsecond resolution at 100 μm will readily resolve this infall region. The radiation from the star formation region in its early stages of evolution would be dominated by an accretion shock around the small protostar, and would peak in the far-infrared due to the large dust opacity in the surrounding cloud.

A number of IRAS point sources have been studied from the KAO and have been shown to be visibly obscured young stellar objects (YSO's). The improved spatial resolution of the KAO over IRAS has allowed determination of the mean densities and temperatures of the infall regions and star formation environments. SOFIA's ten times better sensitivity and three times higher spatial resolution will enable us to make detailed images of the infall regions and their envelopes. SOFIA will, for the first time, detect the dominant cooling transitions of the infalling gas and directly measure the mass infall rate and velocity structure by high spectral resolution observations of the far infrared CO and O I emission lines. High spatial resolution observations of the dust continuum will probe the density structure of the circumstellar gas down to scales of 100 − 1000 AU. The ambient molecular core is expected to have a density $\propto r^{-2}$, while the infall region theoretically has a density $\propto r^{-3/2}$. The infalling gas and dust generally have sufficient angular momentum to impact an opaque ($\sim$100 AU) accretion disk which orbits and feeds the growing star. SOFIA will measure infrared OH spectral lines generated in the accretion shock and thereby determine the mass accretion rate, the location on the disk where the infalling gas and dust mainly strike, and the angular momentum of the impacting material. In summary, SOFIA will revolutionize our understanding of the collapse phase of star formation.

In massive clouds, stars often form in clusters where we currently cannot separate the individual YSO's. Many of these could be isolated in the beam of SOFIA so that, for example, their individual luminosities. masses, and motions relative to one another could be determined. The shape and color of the continuum spectra reveal the evolutionary state of the system. These observations will greatly help us understand the process of fragmentation of large clouds to form star clusters.

(iii) Bipolar Outflows

Since the 1980's, observations have shown that many embedded YSO's are associated with powerful bipolar outflows. These outflows may collide with the circumstellar gas and cause accretion to cease. In this way, they may help determine the final mass of the star. Several theories have arisen to explain the origin of these protostellar winds; they share a common idea that magnetic fields rotating with the protostar or the disk fling trace ions from the inner part of the disk outwards and these ions drag neutral gas along. With SOFIA we can look for evidence of simultaneous inflow along the equatorial plane with outflow along the poles, determine the stage in the evolution of a star when the outflows "turn on", trace the shock interaction of the outflow with the circumstellar gas, and measure the mass-loss rates in the protostellar winds with good fidelity by observing the luminosities in shock-excited O, S, and Si II fine structure lines. FIR polarimetry from SOFIA of the infall regions will show, in the more luminous cases, the association between magnetic fields and outflows.

(iv) Circumstellar Disks

Circumstellar disks have been observed around T Tauri stars, which are thought to be very young stars with masses comparable to that of our Sun. These stars and their disks are formed in obscuring parent clouds. It is thought that the outflows mentioned above could eventually halt the disk accretion. The outflows could also dissipate the surrounding cloud, making the YSO's eventually visible as T Tauri stars. At a later evolutionary stage the disks will dissipate or form planets, and there will be considerable disk clearing. Theoretical models predict that OH emission produced by shock waves set up in the disks by accreting material should be detectable from SOFIA, and the OH line luminosities and profiles can be used to measure the mass accretion rate feeding the disk and the location on the disk where the infalling gas and dust mainly strike. Photometric submm and FIR observations help determine the mass of the disk, which is an essential quantity in understanding planet formation and how disk instabilities may cause the orbiting particles to spiral inwards and accrete onto the star. The disk mass and the accretion rate onto the disk determine the timescale for the formation of the disk; if this timescale is very short it may indicate that, on average, the disk feeds material onto the star as fast as infalling material feeds the disk. Observations of T Tauri stars have shown indirectly that circumstellar disks are generally not much more than 100 AU in diameter – comparable to the size of the solar system – or about 0.6 arcsec at 160 pc. However, HL Tau has been observed at millimeter wavelengths to have a dim 4000 AU (or 24 arcsecond) diameter disk, and FIR photometry from the KAO shows extended emission associated with several T Tauri stars, for example SVS 13. One theory posits that the extended disks are caused by ordered magnetic fields in the ambient cloud which channel the infalling material to an equatorial "pseudo-disk" that is not rotationally supported. The infalling gas then falls radially inward along the equator until it strikes the much smaller rotationally supported disks. Thus at an early stage of their evolution, these disks may be sufficiently extended and luminous to be imaged directly at FIR and submm wavelengths from SOFIA, which would be an exciting and extremely important input to theoretical understanding of low- and intermediate mass star formation.

At later stages of circumstellar disk evolution, when planets are forming or have formed, the disks are harder to see. However, there are ~ 50 candidates for evolved stars with disks which are on the order of 20 times closer to Earth than the nearest T Tauri star, and at their distances 100 AU in the disk corresponds to 10 − 15 arcsec on the sky. The spatial resolving power and sensitivity of SOFIA will allow direct imaging of the structure of a number of these disks for the first time in the FIR. For example, Beta Pictoris ("β Pic") is a main-sequence star that is 17 pc away from Earth with an infrared-luminous disk discovered by IRAS. The infrared disk diameter is ~ 2400 AU, or 140 arcseconds, with the bulk of the infrared flux coming from the central 30 arcseconds. The total IRAS 60 μm flux of the disk, when distributed into five arcsecond diameter pixels – the resolution of SOFIA at 60 μm – will require less than 30 minutes of integration on SOFIA for a signal to noise ratio of 10. It will be possible, therefore, to determine the disk temperature profile and morphology. Combining these results with the knowledge of the illuminating star, β Pic, will enable the properties of the dust in the disk to be studied, in particular the dust-grain size distribution. Figure 7 shows the visible β Pic system with the 5 arcsecond diameter, 60 μm SOFIA beam. The properties of the dust are important since it is probably from these particles that the cores of planets may eventually form, if not in the β Pic system, then in similar disks around other stars.

Figure 7. Optical photograph of the β Pic disk, with 60 μm SOFIA beam size superposed. The stellar image has been blocked with an occulter.

SOFIA can map spectroscopic features in the disk as well, for example the water ice feature at 48 microns and the polycyclic aromatic hydrocarbon (PAH) features at 5.2, 6.2 and 7.7 microns. Such features help to ascertain the composition of the dust and hence the nature of planets which may be forming at particular locations in the disk.

(v) Our Solar System

The initial composition of our pre-solar nebula is of great interest because it contained the building blocks of the planets and of life. SOFIA's ability to explore an early pre-planetary system environment through observations of nearby circumstellar disks was discussed in §(iv). SOFIA will also image, spectroscopically as well as photometrically, dense clumps in nearby dark clouds, in order to determine the composition of future pre-solar nebulae. However, to better understand the origin of our Solar System, studies of comets, planets, and satellites are essential.

Comets

Comets are aggregates of ice, dust, and organic solids that accumulated in the region of the solar nebula where the outermost planets formed, and as such they are the most accessible repositories of chemical remnants of the original interstellar material that spawned the solar nebula. Observations of many comets show that they are an eclectic sampling of different regions of the solar nebula; some show abundant reduced carbon, some show no carbon at all, some exhibit silicate minerals, and others show hydrocarbons and minerals in various proportions.

Spectroscopic studies of comets in the near infrared ($2-8\,\mu$m) with SOFIA can address questions of the chemistry and processing of carbon in the solar nebula through analyses of the reduced carbon (CH_3OH = methanol, and other organics) and oxidized carbon (CO_2 = carbon dioxide). Carbon dioxide in comets cannot be observed from the ground, but with a favorable Doppler shift, high-resolution spectroscopy from SOFIA will permit observations of this key molecule in the volatile carbon budget. Even though the discovery of organic material in the nuclear dust of Comet Halley was achieved from the ground looking at the C–H stretch feature near 3 microns, in order to determine the nature of the molecules producing this feature we must observe these species between 5 and 8 μm where the C–O, C–C, and C–N stretch bands are found. Again these wavelengths cannot be observed from the ground, but are readily accessible to an airborne platform.

Similarly, water in comets cannot be detected from ground-based observatories, but as demonstrated by its discovery in Comet Halley from the KAO (Figure 8), water is readily measured at high spectral resolving power ($\sim 10^5$) from the lower stratosphere. The ortho-to-para ratio in the hydrogen in H_2O in comets (measurable at 2.75 μm), as well as the deuterium content of the water (HDO/H_2O), establishes the temperature of formation of the comets (~ 30 K for Halley), as well as the local chemistry of the solar nebula at the comet formation site(s). A basic question about the local chemistry is whether the processing of water and the organics was controlled by kinetics or by ion-molecule reactions. The relevant observations can only be made from SOFIA, whose large aperture, long lifetime, and sensitive two-dimensional array spectrometers will make available many more comets than can be observed from the KAO.

Finally, SOFIA will have the sensitivity to study solid state features (such as water ice and olivine) in short period comets. These comets have orbits that extend to about 7 AU from the Sun, and therefore may contain material that has undergone considerable processing by solar radiation. Comparison of these materials with those seen in long period comets, which sample a more pristine environment, will be extremely interesting.

Planets and Satellites

A related fundamental question concerns the initial compositions of the volatiles incorporated into the giant planets and their satellites during formation, since these would imply certain conditions in the regions of the solar nebula where they formed. Two extreme models are that the outer planets and their satellites consisted of (a) water, methane, and ammonia (in order of decreasing abundance) or (b) carbon monoxide, water, and molecular nitrogen. In the
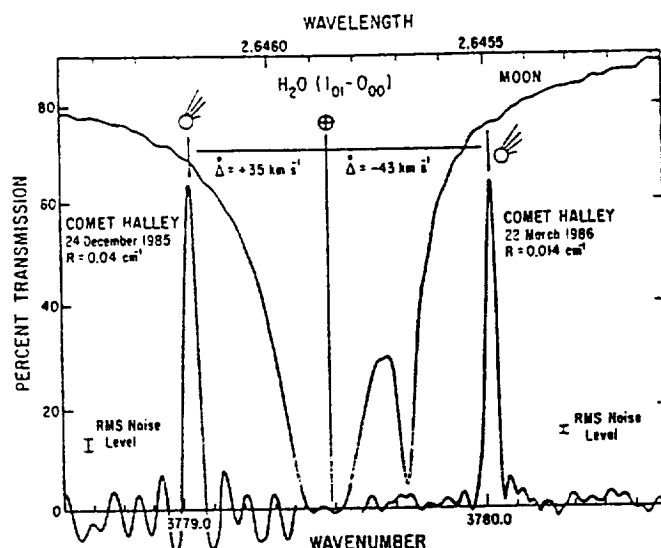
Figure 8. Spectra of water in Comet Halley and the moon taken from the KAO, which was scheduled to maximize the Doppler-shifted separation of the comet and telluric features. The spectral resolving power is $\sim 2 \times 10^5$.

currently accepted model, the giant planets consisted of composition (b), while in their satellites composition (a) dominated. Jupiter and Saturn might have converted the carbon monoxide to carbon dioxide and methane, and the nitrogen to ammonia, but Uranus and Neptune should have retained substantial amounts of their original composition. The satellites of the outer planets may retain surface spectral signatures of the primordial partitioning of these constituents. It is therefore important to determine the composition of the volatile-rich outer planet satellites and Pluto, the composition of their atmospheres (if any) and the nature of the surface-atmosphere interactions.

Better understanding of the atmospheres of the giant planets will further elucidate questions about the chemistry of the solar nebula. High resolution spectroscopy from near infrared to submillimeter wavelengths enabled by SOFIA will be especially suited to measurements of trace constituents in the atmospheres of the giant planets. Several trace gases on Jupiter (e.g., GeH_4 and CO, present at the 10^{-8} levels of concentration with respect to H_2) have been found with the KAO in the $2 - 5$ μm spectral region. The determination of a larger inventory of these constituents in Jupiter and the other giant planets from sub-millimeter spectra, and the computation of the vertical distribution profiles, will yield fundamental information on the photochemistry in the atmospheres of these planets. Some of the same photochemical processes occur in the atmospheres of the Earth and other terrestrial planets, thus allowing comparative studies of direct relevance to our own planet.

SOFIA's angular resolution will permit zonal resolution on a number of Solar System bodies. Imaging spectroscopy will reveal spatial variations of atmospheric, comatic, or surface constituents with a resolution of about 2 arcsec in the near infrared, increasing to 10 arcsec at 100 microns. The spatial resolution also reduces line broadening. On Mars (diameter 4800 km), 2 arcsec

corresponds to ~ 400 km, and on Jupiter (diameter 14300 km) to ~ 700 km. Spatially resolved spectra of Mars with SOFIA will give important information on the exchange of volatiles (CO_2, and perhaps H_2O) between the polar caps and the temperate regions as the Martian seasons change. and will reveal the zonal and latitudinal distribution of the major and minor atmospheric constituents. SOFIA can resolve the Great Red Spot of Jupiter in the $2 - 8$ μm region where the chromophores, causing the still-unexplained color, may have their diagnostic spectral signatures.

In addition, much valuable research will be done from SOFIA on planetary bodies too small to be spatially resolved. For example, Pluto and Triton are two significant bodies in the outer Solar System, each composed of a mixture of rock and ice. Their tenuous atmospheres (of mostly nitrogen) appear to be in vapor pressure equilibrium with their surface ices. Both Triton and Pluto experience extreme seasonal cycles, and determining the interaction between their surfaces and atmospheres over these cycles is quite complex. Understanding this interaction requires simultaneous knowledge of several related parameters, such as the dimensions of the body, albedo distribution across the surface, temperature, surface composition, and atmospheric density. Significant variations in the parameters will occur during the lifetime of SOFIA. A unique contribution to this problem will be SOFIA's observations of stellar occultations by Pluto and Triton over the years, to determine the densities of their tenuous atmospheres at various points in their seasonal cycles. The same observations are vital in constraining the diameter of Pluto (Triton's diameter is already well known from spacecraft data). FIR photometric measurements from SOFIA can provide the color temperature and its variation with rotation and season for both bodies. In combination with optical photometry, these data will provide information on the albedo distribution and its time variation. Finally, low-resolution IR spectroscopy will provide new information on the composition of the surface ices.

Stellar occultations, which probe Solar System objects with a spatial resolution of only a few kilometers, are of course applicable to a variety of other problems. An airborne observatory is ideally suited to this powerful technique, since it permits the telescope to be optimally located and weather-free for a particular event. The value of deployment has been demonstrated by the KAO's history of occultation work, most dramatically by the discovery of the ring system around Uranus in 1977 (Figure 9).
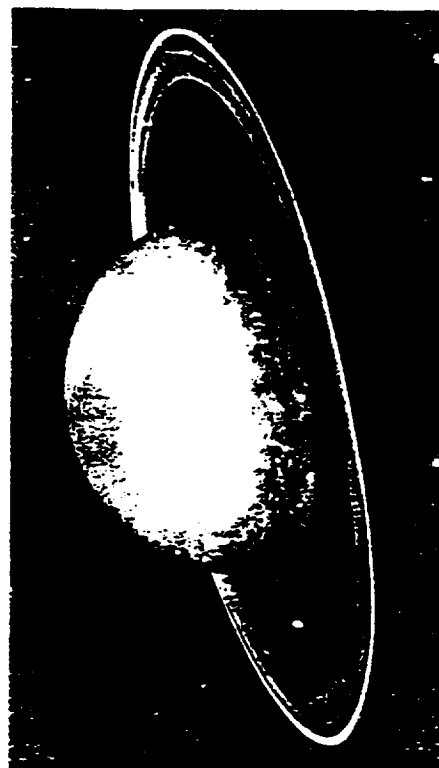

Figure 9. Artist's concept of the rings of Uranus discovered from the KAO.

SOFIA will be capable of observing many more occultations than the KAO, with greatly improved signal-to-noise, because of its increased aperture. Besides the studies of Triton and Pluto, SOFIA can obtain temperature, pressure, and number density profiles of the atmospheres of Uranus and Neptune, bodies for which no spacecraft entry probes are currently planned. SOFIA can also be used, in conjunction with ground-based information observations, to vastly improve our knowledge of Saturn's ring dynamics through observations of a series of ring occultations. From observations spanning several years, the orbits of the edges and narrow singlets in the ring system can be determined with much greater precision than has been possible with flyby spacecraft. Improved orbital information will lead to further understanding of the ages of the rings (whether they were formed with Saturn or more recently), the evolutionary processes in particle disks, and the internal structure of Saturn (from its gravitational harmonic coefficients).

As spacecraft are sent to Jupiter (Galileo), Saturn (Cassini), and to the small bodies of the Solar System (e.g., Clementine and NEAR), supporting observations from SOFIA will be of long-term importance. For example, the infrared spectrometer ($\sim$ 15 – 500 μm) planned for Cassini has a spectral resolution of only 1 cm^{-1}, sufficient for detection of molecular lines in the far-infrared, but insufficient for observations of the intrinsic line profiles. Complementary high-resolution spectroscopy from SOFIA will establish the intrinsic line shapes to reveal physical conditions, in the atmospheres of Saturn and Titan, for example. Similarly, results obtained from SOFIA may help to define future space missions, as the KAO occultation results on Pluto have done for the Pluto Fast Flyby mission.

(vi) The Sun

The star that influences Earth the most is our Sun, not only through its radiation but through its solar wind as well. The solar wind originates in the chromosphere and corona, although the energy transport mechanism which heats the corona and drives the wind is not well understood. Oscillation of the solar atmosphere probably plays a role in this process, and pioneering FIR observations on the KAO, combined with ground-based sub-millimeter observations, have detected the oscillations at different depths in the solar atmosphere. Wavelength-dependent phase differences show the vertical transport of energy at the oscillation frequency. Far-infrared beam sizes from SOFIA will be well matched to the size of the oscillation cells, and will provide improved information on the strength of the oscillations and on the correlation between adjacent cells. This will yield significant insight into the energy transport mechanisms in the solar atmosphere.

(vii) Stellar Structure

In the last fifteen years, studies of multi-mode pulsations in the Sun (helioseismology) have revealed a wealth of detail concerning the Sun's internal structure and dynamics. Observations of pulsations on other Sun-like stars would extend our understanding of stars in general, and in particular would permit more exhaustive tests of stellar evolution theories than previously possible. CCD ensemble photometry at visible wavelengths provides one of

the most promising techniques for measuring such pulsations, but the expected pulsation amplitudes for Sun-like stars are small (only about three micro-magnitudes), while the best ground-based observations (conducted with a network of 4 meter-class telescopes) produce detection limits about 5 times as large.

Ground-based photometry is limited in precision by scintillation noise, which arises mostly in the troposphere. Simple scaling of ground-based scintillation noise to SOFIA, ignoring the lower turbulence amplitude in the stratosphere, indicates that the signal-to-scintillation noise ratio will be at least a factor of 3 lower than for a 10 meter ground-based telescope. This noise level would permit detection of solar-like pulsations within about 3 hours of observing time from SOFIA on any of about 300 stars. Rough amplitude estimates alone would significantly probe the mechanisms that excite and damp oscillations in stars like the Sun. For suitable stars (G and K dwarfs brighter than roughly 6th magnitude), observing the same star for 2 hours at the beginning and end of a 7.5-hour flight would allow resolution of the so-called "large frequency separation" in the stellar frequency spectrum, which immediately yields a precise estimate of the mean stellar density. Observations of one star over several nights could provide accurate frequency estimates for up to a dozen pulsation modes. Thus SOFIA will enable a significant program of stellar seismology.

(viii) Reprocessing of the ISM

The bulk of the elements heavier than helium have been synthesized in dying stars. These stars have finished the hydrogen burning phase in their cores and have commenced burning helium to form heavier elements. The central material is then mixed to the surface and is observable in the infrared in the form of bands of molecules, such as CN and CO, in the stellar spectrum. As the star evolves, these surface elements can be ejected back into the ISM by stellar winds, as in the case of the red giants, or in some cases by the loss of the star's whole outer shell, either at a non-catastrophic rate, as in the case of a planetary nebula, or at an explosive rate, as in the case of a supernova. In supernovae considerable nucleosynthesis of heavy elements can occur in the blast; for example observations from the KAO detected lines from nickel, cobalt, and iron atoms produced by the explosion of Supernova 1987A. The KAO also detected the formation of dust in the ejecta about 600 days after the explosion. SOFIA's sensitivity and resolution would permit improved studies of bright supernovae in other galaxies. Also, SOFIA will be well suited to study the common mass-loss stars such as the red giants and planetary nebulae, with sufficient sensitivity to permit resolution of the spectral lines of many important atoms and molecules, permitting studies of both the dynamics and rates of mass-loss.

(ix) Other Galaxies

Observations from the KAO discovered that spiral galaxies typically emit as much energy at far-infrared wavelengths as they do throughout the visible and ultraviolet. The extensive IRAS observations of galaxies showed that many have infrared luminosities exceeding their visible luminosities by factors of ten or more. ISO and SIRTF are anticipated to make great contributions
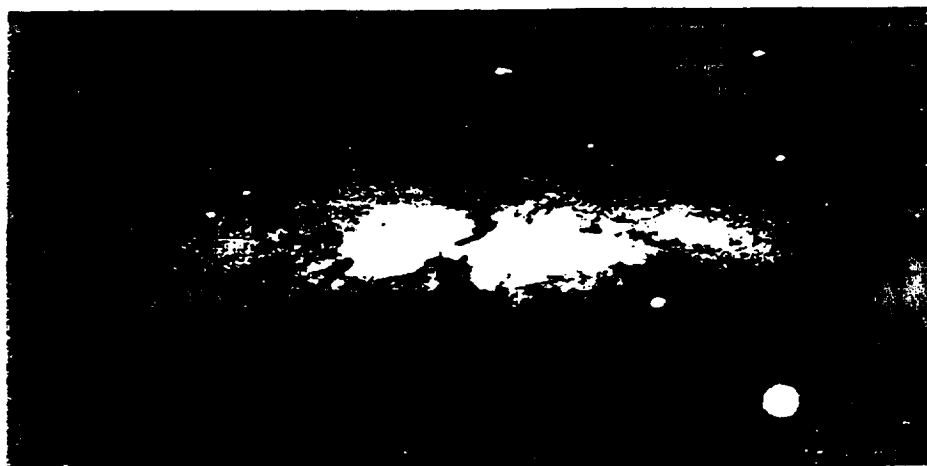
Figure 10. Optical photograph of M82.

to the understanding of other galaxies, but the high spatial resolution and the anticipated development of large far-infrared arrays enable SOFIA to make an important complementary contribution as well. SOFIA will observe nearby (~ 1 Mpc) spiral and irregular galaxies, nearby (~ 10 Mpc) starburst and Seyfert galaxies, and nearby (~ 100 Mpc) extremely luminous galaxies such as Arp 220 and Mrk 231. In the nearby spirals and irregulars, SOFIA's FIR arrays will investigate galactic structure and its influence on star formation at scales ~ 10 pc, primarily by mapping dust continuum and fine structure lines from atomic and ionized gas. At these scales, the relative positions and velocities of the molecular gas, dense photodissociated gas and H II regions, diffuse HI gas, dust IR continuum and the optical images of star forming regions will probe the roles of bars and spiral density waves in controlling star formation. Pressures in the neutral and ionized gas can be determined and correlated with star formation. Elemental abundance gradients can be measured as functions of galactocentric radius to constrain the past history of star formation and nucleosynthesis.

In nearby starbursts and Seyferts, SOFIA's ~ 100 pc resolution will map the star formation activity in the central kpc and may spatially separate the central interstellar medium affected by an AGN from the more extended region affected primarily by the ultraviolet radiation and shock waves induced by star formation and supernovae. NGC 1068 is an important example of a nearby Seyfert in which SOFIA will separate these two regions. M82 is a nearby starburst galaxy in which SOFIA will help unravel the nature of the central starburst. KAO measurements of O III (52 and 88 μm), N III (57 μm), O I (63 μm) and Si II (35 μm) line profiles from the obscured nucleus of M82 are consistently asymmetric and suggest strong variation in the emission from different components of the source. These components may be areas of intensive localized star formation, or recent supernova outbursts; supernovae are thought to occur in M82 every few years. Judging from radio maps, SOFIA could readily isolate some of the candidate components, but telescopes the size of the KAO and smaller (≤ 90 cm) cannot. The disturbed visible appearance of M82 (Figure 10) gives only a hint of the recent formation and violent demise of massive stars there.
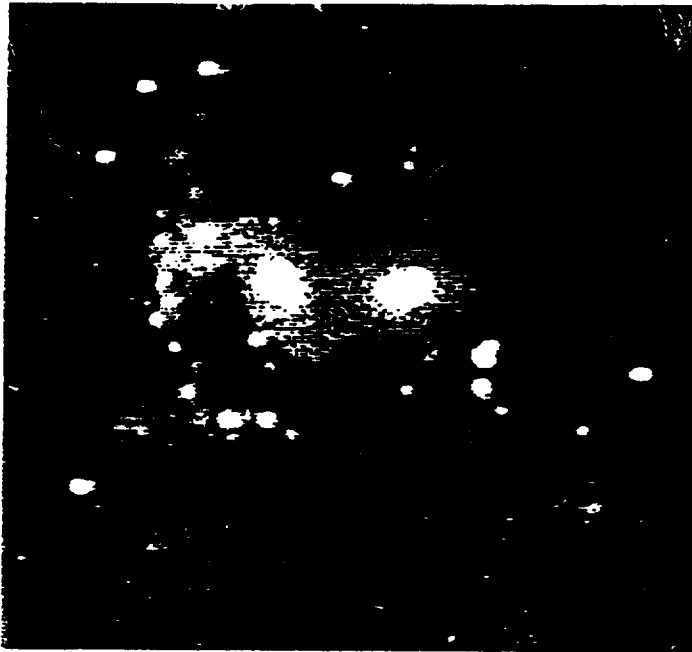
Figure 11. CCD image of the galaxy pair NGC 7318.

Many of the galaxies found to have large infrared excesses by IRAS have subsequently been identified as galaxies in collision. Study of these ultraluminous infrared mergers is seriously hindered at near-infrared, optical, and ultraviolet wavelengths because of the large obscuration by dust embedded in them. However, SOFIA will permit FIR, photometric, and spectroscopic imaging on a scale of $\sim$ 1 kpc, adequate to reveal brightness distributions of emitting dust and gas on a scale comparable to the visible structure seen in many of these systems, and ample to distinguish components such as the active nuclei, the young starburst (O and B stars), the older starburst (SNRs, red supergiants), the shocked clouds, and the old stellar population.

Figure 11 shows the interacting galaxy pair NGC 7318 in Stephan's Quintet. In this false color image, which is a superposition of two optical CCD images taken through different filters, one can distinguish the older generation of stars that make up the bulk of the galaxies from the distribution of ionized hydrogen gas, which traces sites of recent star formation activity within the galaxies. The nuclei of the two galaxies are separated by 20 arcseconds.

Images at different wavelengths, including those beyond 100 μm which IRAS did not sample, will yield temperature and optical depth profiles. Far-infrared and sub-millimeter spectroscopy will probe the excitation conditions, temperature, density, composition, and dynamics of the gas in these systems with similar spatial resolution. Far infrared rotational CO lines, and fine structure lines of O I, Si II, C II, O III, S III, and N III, will be important diagnostics.

(x) The Galactic Center

In many ways, the most exciting place in our own Galaxy is at its center where the stellar densities are very high, stellar collisions are probably frequent, and the existence of a central, massive black hole not unlikely. This region represents the closest galactic nucleus to us. Far-infrared observations have shown that the Galactic Center has an infrared luminosity of roughly 10^7 $L_\odot$, is enshrouded in a dense dust ring, is to some degree shaped by magnetic fields, and is obscured at visible wavelengths by the intervening dust in the galactic plane by a factor of roughly 10^{10}. The distribution of red stars can be studied (with large extinction corrections) in the near-infrared and the distribution of ionized gas can be studied at radio wavelengths. However, the neutral atomic gas, thermally emitting dust, and important characteristics of the ionized gas can best be studied at the wavelengths accessible from SOFIA.

The ring of dust emission about the galactic center, which was first discovered from the KAO, is about 3 arcminutes in diameter and the cavity it defines at the center is only 30 arcseconds in diameter. Current results show that material from the ring (or outside it) may be spiraling into the center, that high turbulent velocities are present, and that magnetic fields may be important in this region. The data are consistent with the existence of a massive central object, possibly a black hole, or a compact cluster of stars. The exact location and character of the dominant source of luminosity in the cavity is unknown; two possibilities are the emission from a black hole accretion disk or emission from a number of massive stars. Of all the candidates for a massive black hole, if it exists, the non-thermal point source SgrA* is the most probable. Further, there is indirect evidence for the existence of a wind or jet originating at SgrA* causing a mini-cavity to be formed in the gas and dust about 5 arcsec southeast of SgrA*.

SOFIA will clarify the picture within the cavity on three times finer spatial scales than possible with the KAO, by resolving regions of different velocities, ionization levels, magnetic field directions (i.e. polarizations), temperatures, and gas densities. For example, a more accurate estimate of the location, UV spectrum, and luminosity of the central powerhouse within the cavity would be obtained by SOFIA by mapping the distribution of dust, neutral atomic and ionized atomic emission within the cavity with a three-fold improvement in spatial resolution over that achievable on the KAO. SOFIA could also study the jet (or wind) originating from SgrA* by measuring the fine structure line emission from the mini-cavity which is 4 arcsec in diameter. Line dilution makes this study impossible from the KAO. In addition, SOFIA could address the puzzle of where the massive stars in the cavity originate, if they are the source of the luminosity. The main sequence lifetimes for such stars are too short for the stars to form farther out and then diffuse into the central cavity. There is no evidence for dense molecular gas in the cavity but SOFIA may show the existence of neutral atomic clumps, perhaps characterized by high velocities, that cannot be spatially resolved by the KAO.

SOFIA, with its superior FIR resolution, would reveal if the streamer of neutral atomic gas inside the cavity is spiraling into the center from the inner surface of the dust ring or from outside the ring, possibly from clouds tens of parsecs away. Using FIR polarimetry, SOFIA will also image the structure of the magnetic fields within the dust ring and the cavity at a resolution that
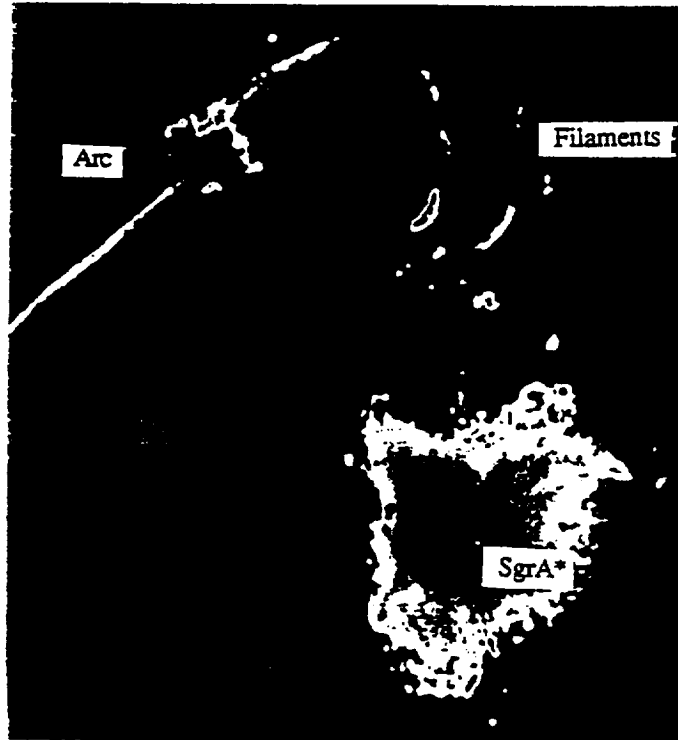
Figure 12. A grayscale radio (20 cm) image of the Galactic Center region. The figure is roughly 30 pc × 30 pc or ~ 15 × 15 arcmin in extent.

will be sufficient to test whether the dust ring is a magnetic accretion disk, removing its angular momentum centrifugally, or an assembly of unresolved magnetic streamers, or some other scenario.

Magnetic fields play an extensive role at larger scales in the vicinity of the Galactic Center as well. Ten arcminutes north of the dust ring, radio maps have shown the existence of peculiar large arcs of synchrotron emission, extending for about 20 pc perpendicular to the Galactic plane. The source of the electron excitation is unknown. These arcs seem, in projection, joined to the dust ring region of the Galactic Center via thermal arched filaments of ionized and neutral gas, and dust (see Figure 12). The KAO has shown that these filaments have luminosities ~ 10^7 $L_\odot$, and that the magnetic fields lie along the filaments, almost parallel to the Galactic plane. The source of ionization and heating of the arched filaments is also unknown, although undetected hot stars are the most likely candidate. However, the morphology of the filaments and the connection between the magnetic fields and such stars is a mystery. With the improved resolution of SOFIA we can use FIR fine-structure lines to examine ionization stratification in the arched filaments to seek the hypothetical embedded clumps of stars if they exist.

Obviously SOFIA will clarify our currently limited perception of phenomena in and around our own Galactic Center, which in turn will be a crucial step toward understanding similar phenomena seen on larger scales in many other galactic nuclei.

4. Comparison with Other Missions

Many important problems in modern astronomy require infrared observations with high sensitivity, high spectral resolution, and high angular resolution, or a combination of these capabilities. To fill these needs, the National Academy of Sciences Decade Survey (Bahcall) Committee has recommended *both* SOFIA and SIRTF (the Space Infrared Telescope Facility) as high priorities for development by NASA during the 1990's. A discussion and individual mission summaries of past and future infrared missions is contained in Session Nine of these proceedings, starting with the discussion summary by Caroff (1994).

Here we present a brief comparison of the principal missions SOFIA, SIRTF, ISO (the Infrared Space Observatory), KAO, and IRAS. Figure 13 and Table 3 depict the features of these missions which underlie the differences in their science goals. Table 3 compares launch/first flight dates, telescope diameters, design lifetimes, instrument complements, mobilities, and sponsors.

Table 3

KAO	IRAS	ISO	SOFIA	SIRTF
1974	1983	1995	2000	2002
0.91 meter	0.60 meter	0.60 meter	2.5 meter	0.85 meter
20+ years	1 year	$1\frac{1}{2}$ year	20 years	$2\frac{1}{2}$ years
12/Evolving	2/Fixed	4/Fixed	15/Evolving	3/Fixed
Deployable	Earth Orbit	Earth Orbit	Deployable	Solar Orbit
USA	USA+NED+UK	ESA+JPN+USA	USA+FRG	USA

Basically, the cryogenically cooled space missions achieve far higher sensitivity in broad wavelength bands, whereas the airborne facilities permit higher angular resolution and capacity to accommodate new instruments and science programs over a long lifetime. For example, the SOFIA science program will capitalize on its spatial and spectral resolution, for example in revealing how stars form, and on its mobility, which permits optimum observations of ephemeral events such as occultations. The SIRTF science goals exploit its excellent sensitivity and large detector arrays, for example to study galaxy formation at the edge of the visible Universe. SOFIA's targets will typically be galactic objects or nearby galaxies that may be studied in detail not possible with SIRTF, while many of SIRTF's targets will be faint or distant objects that would be undetectable with SOFIA. SIRTF's focal plane instruments are optimized for the highest priority scientific goals, but will be used for a range of scientific investigations. SOFIA's program is broad in scope because of its wide wavelength coverage, long lifetime, and annual opportunities to propose new science investigations and focal plane instruments.

As pointed out by Caroff (1994), in addition to its unique science potential, the airborne program provides unique continuity, training opportunities, and wavelength coverage to the infrared community.
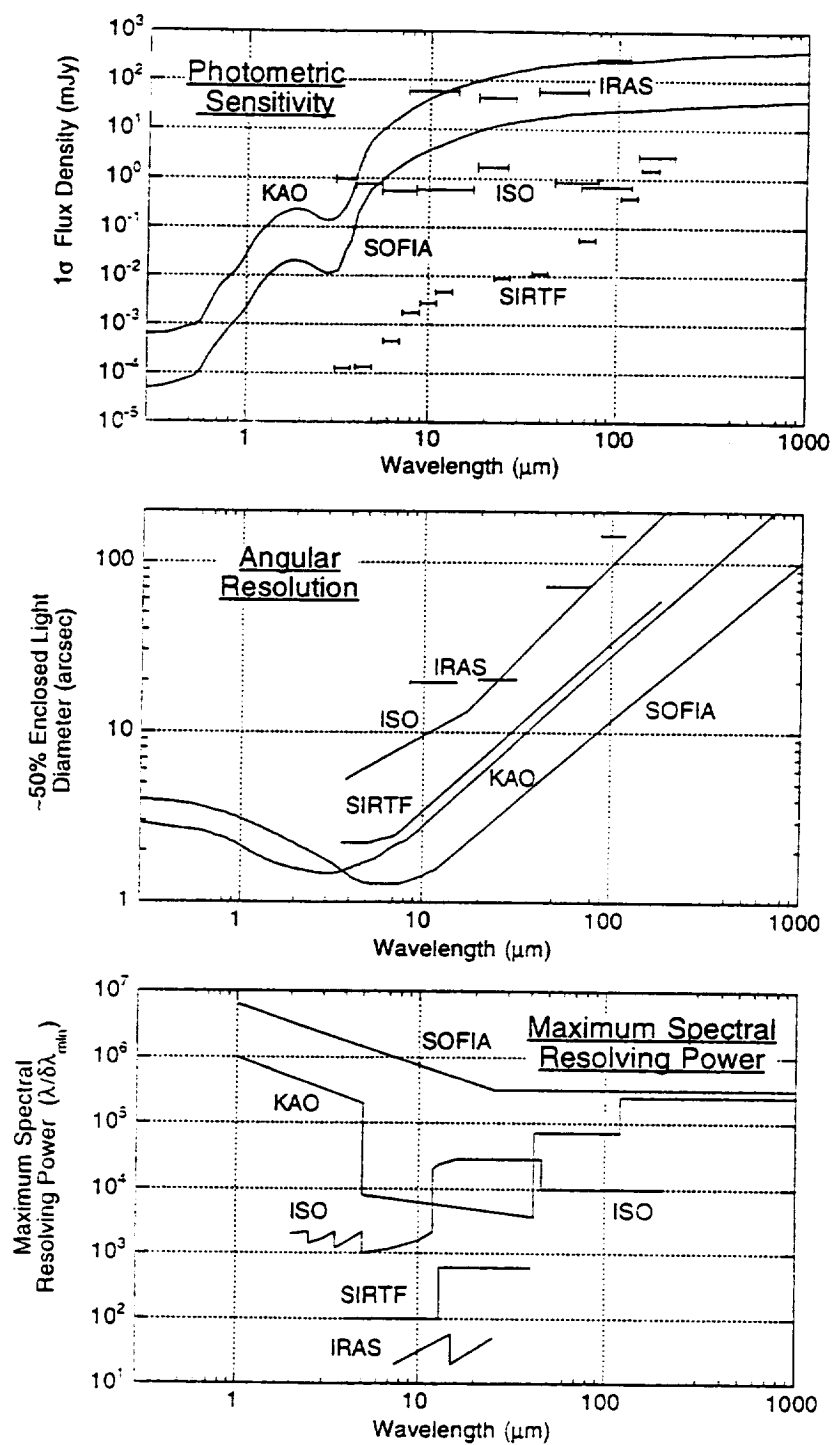
Figure 13.   Photometric sensitivity, angular resolution, and spectroscopic resolving power for the KAO, IRAS, ISO, SOFIA, and SIRTF as a function of wavelength.

5. Education

Scientific and technical literacy are among the most critical needs of our nation. We benefit not only from brilliant researchers and creative inventors, but also from understanding of and respect for scientific endeavors by the taxpayers who must support them, and who themselves will be working in an increasingly scientifically and technologically advanced world. Thus, education in the fields of science, mathematics, and technology is not simply an investment in future scientists and engineers, but an investment in the appreciation of society for these endeavors. Through its unique scientific mission, SOFIA can increase this appreciation.

For scientists, SOFIA will provide a unique window to view the invisible infrared universe. However, for educators, it will be an exciting and accessible example of leading-edge high technology in the telescope, the scientific instrumentation, and the mission operations systems. For the public, SOFIA will serve as a high visibility, modern scientific facility, *epitomizing* the American ideals of innovation, exploration, and achievement.

The extensive participation in SOFIA observations by the science community, and the opportunities for teachers and the media to experience science in action on board, guarantee the potential of SOFIA for education. The rapid response of an airborne observatory to ephemeral astronomical events also helps to attract and focus public attention on science, as was the case for the KAO observations of Supernova 1987A, and for the impact of Comet Shumaker-Levy on Jupiter in 1994. These events frequently require remote deployments, which will expose this modern flagship of astronomy to the public world-wide, amplifying its effectiveness in expanding awareness of science.

The education program on SOFIA will offer to non-scientists a first-hand view of scientific research: its excitement, hardships, challenges, frustrations, teamwork, and discoveries. The intent of the SOFIA educational program is to bring these experiences to American students, teachers and the public routinely and on a significant scale. These outreach efforts will be built into the core program and evolve from the experiences with programs currently conducted with the KAO, such as the Flight Opportunities for Science Teacher EnRichment (FOSTER). SOFIA will be larger and fly more frequently than the KAO, and thus can support an expanded program.

Outreach activities are planned which will serve (1) pre-college students and teachers, (2) undergraduate and graduate students and faculty, and (3) the public and the media. SOFIA will promote excellence in science, mathematics and technology education through direct involvement of non-scientists with the SOFIA investigators, and via workshops, internships, and utilization of existing educational infrastructure such as museums and planetaria. In addition, many people will be able to experience SOFIA research remotely through the Internet and telepresence. Ongoing internal and external evaluation of the program will assure its effectiveness, much as the peer review process will do for the science program. Educational activities on SOFIA will touch the spirit and imagination of many American youth.

6. Technology

The unique observing potential, 20 year lifetime, and frequent opportunities for participation which SOFIA will offer the scientific community assure the development and prompt application of new technologies. Many of these will surely be valuable in future space and ground-based astronomy, as well as in other areas. The history of the airborne astronomy program is a guide to this process: the chopping secondary mirror, a feature of all modern infrared telescopes, was initially developed for the Learjet telescope. This facility also allowed the first "hands-on" testing of far-infrared bolometer detectors and a He^3 refrigerator in an astronomical application.

KAO investigators have extended this work by making significant contributions to bolometer array and newer refrigerator technologies, which are used on ground-based submillimeter telescopes, as well as on the KAO. Detectors anticipated for use on SIRTF and AXAF are currently being flown in KAO instruments. Experience with KAO focal plane instruments has been applied to the design of the space missions IRAS, COBE, ISO, SWAS, Cassini, AXAF, WIRE, and SIRTF. Germanium photoconductor detectors developed for use on the KAO were actually used on IRAS. We anticipate that nearly all future space IR missions (e.g., FIRST and Edison) will reap major benefits from SOFIA-related technology.

Some of the technologies evolved in conjunction with SOFIA may have commercial applications. For example on the KAO, extensive research was done to develop infrared radiometers to measure the atmospheric water column depth overhead; this technique proved useful in detecting clear air turbulence, and the technology is now under review for suitability on commercial aircraft. In conjunction with wind tunnel testing of the SOFIA model, a pressure sensitive paint has been developed to provide very high spatial resolution of the pressure variations on airfoils; this technology has already been applied by major American aircraft companies in new wing designs. Future SOFIA technology could find application in aerodynamic noise reduction for aircraft, automated intelligent systems monitoring of real-time control systems, and mission operations and planning procedures for space flight.

7. Readiness

A configuration with the telescope cavity located behind the wing has been shown in predevelopment studies with aircraft modifiers to be much less expensive than putting the telescope ahead of the wing. Extensive analysis, including infrared observations of the exhaust plumes from NASA's Shuttle Carrier Aircraft (a Boeing 747), has shown that scattered emission from this source is not a concern for all but a very small class of possible science investigations. The aft configuration has been adopted as a cost cutting measure, although it may increase the seeing distortion of the images at near infrared wavelengths (Figure 2) due to the thicker boundary layer in the rear of the plane. Figure 14 depicts the design with the aft cavity installation of the telescope.

Wind tunnel tests of the airflow over the open-port telescope in an aft cavity have resulted in a quiet, low drag shear-layer control concept for SOFIA, and have demonstrated that the flow reattachment is stable and the control
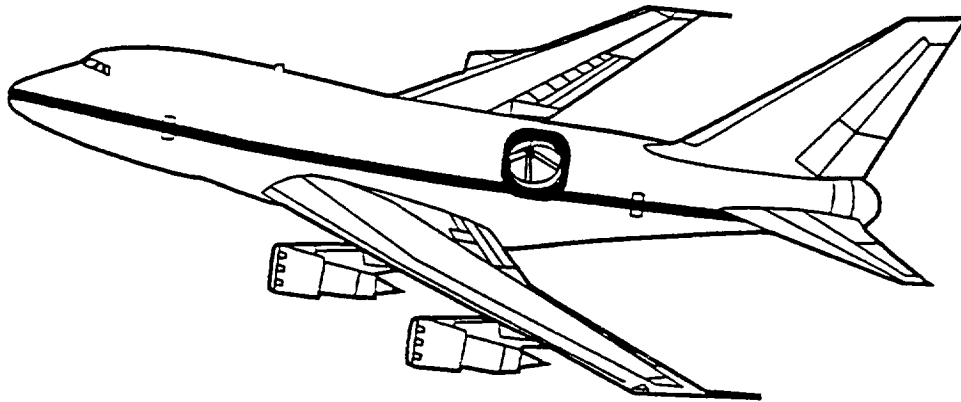
Figure 14. The baseline SOFIA design concept.

of the aircraft is not affected for expected flight conditions. These tests also provide good estimates of the wind loading on the telescope. Further wind tunnel tests are anticipated to select among the door design concepts currently being considered.

The telescope design (Figure 15) features an airbearing support and numerous other similarities to the KAO telescope, which has achieved sub-arcsecond pointing stability even in light turbulence. Structural and optical analyses indicate that either a metal or composite structure could be used, and that any of several (glass) primary mirror designs would work. The 2.5 m primary can be as slow as ~f/1.5 with the telescope in the aft location, so that figuring is not a problem; the chopped image quality is better for larger primary f-numbers.

SOFIA definition studies, sponsored jointly by NASA and the German Space Agency DARA, have been completed, and the project has been deemed ready for development by these agencies. If funding is available, NASA and DARA plan to begin the development of SOFIA in 1996, which would permit the first flights to occur in the year 2000.

8. Conclusion

The characteristics of SOFIA — its astronomical promise, moderate cost, maintainability, and opportunities for broad-based community participation — will extend the tradition of the airborne program for innovation, education, and exciting science. Its vision will penetrate dark reaches of our own and other galaxies, revealing objects and processes otherwise hidden from view with spatial resolution which will be unmatched until well into the next century. It will elucidate problems ranging from the spectacular death of massive stars to the inconspicuous incubation of low mass stars, from the composition of interstellar dust to the formation of prebiotic materials and protoplanetary
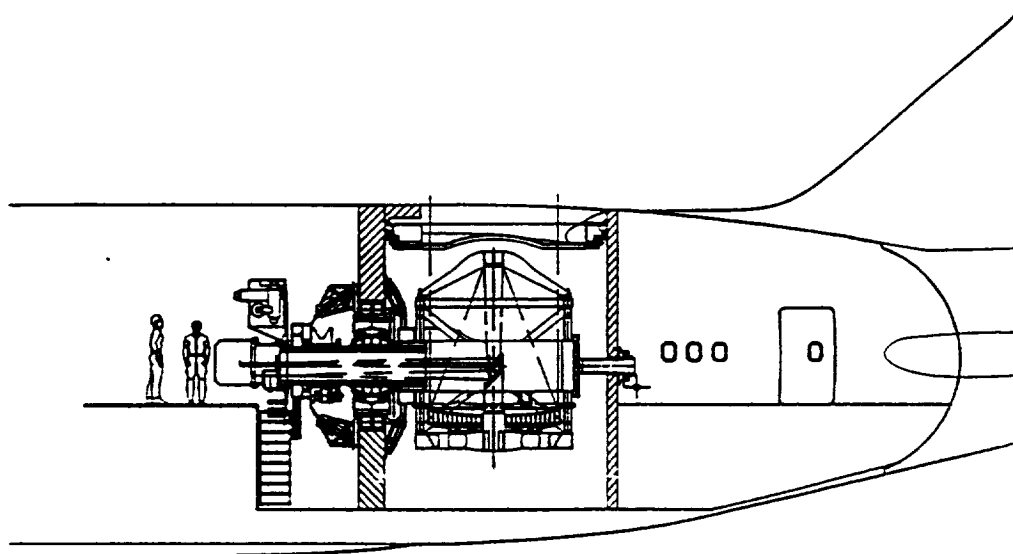
Figure 15. The SOFIA telescope installation in a Boeing 747-SP.

systems, and from the enigmatic character of our own Galactic Center to the nature of stupendous luminosity sources in colliding galaxies. SOFIA's image, performance, and accomplishments will be a credit to its heritage.

9. Acknowledgments

It is a pleasure to thank Al Betz, Harold Butner, Dale Cruikshank, Ted Dunham, David Hollenbach, and Dan Lester for contributions to the science section, Edna DeVore for contributions to the education section, and Mike Werner for assistance with the comparison of SOFIA to other missions. The photograph of M82 was provided by the Mount Wilson and Las Campanas Observatories, Carnegie Institution of Washington. The photograph of Beta Pictoris is credited to Bradford Smith (University of Arizona) and Richard Terrile (JPL). The picture of Uranus and its ring system was painted by Rick Sternbach. Howard Bushouse (Computer Sciences Corporation) provided the CCD image of NGC 7318. The drawings SOFIA and of the SOFIA telescope were produced by Dan Machak and Will Valloton (respectively) of NASA Ames.

10. References

Caroff, L. J. 1994, in Proc of the Airborne Astronomy Symp on the Galactic
       Ecosystem: From Gas to Stars to Dust, ed. M. R. Haas, J. A. Davidson,
       & E. F. Erickson (San Francisco: ASP), p 647
Larson, H. P. 1994, in Proc of the Airborne Astronomy Symp on the Galactic
       Ecosystem: From Gas to Stars to Dust, ed. M. R. Haas, J. A. Davidson,
       & E. F. Erickson (San Francisco: ASP), p 591
Traub, W. A., and Stier, M., 1976, Applied Optics, 15, 364

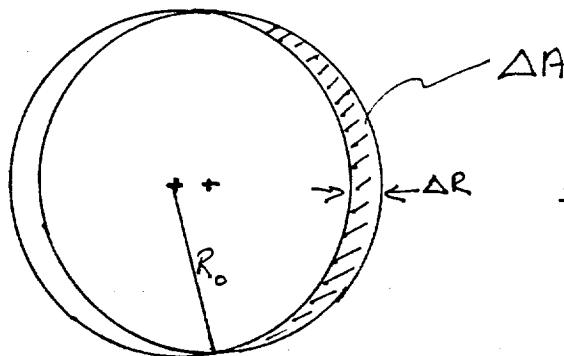# Tertiary Mirror Size for SOFIA

J. A. Davidson
11/1/95

This report follows from the report by Paul Harvey dated 3/22/89 on "Noise Considerations Dependent on Tertiary Size and Telescope Flexing." In this report we calculate the amount of oversizing required for the tertiary, based on arguments presented in the Harvey report.

Consider a single beam "emitted" from the center of the SOFIA focal Plane. Geometrically, a system with an $f/\# = 20$. will illuminate a 25 cm diameter circle 5 meters from the focal plane with such a beam. The tertiary lies about 5 meters from the focal plane.

Now consider a face-on view of the tertiary mirror with radius R_o as seen from the focal Plane.

$$A = \pi R_o^2$$

$$\frac{\Delta A}{A} \simeq \frac{\pi R_o \times \left(\frac{1}{2}\Delta R\right)}{\pi R_o^2} = \left(\frac{\frac{1}{2}\Delta R}{R_o}\right)$$

If the beam from the focal plane is displaced by ΔR

then $\quad \Delta A$ = Area off mirror where the detector "sees" the backplate with temperature T_B & emissivity ϵ_B.

$+ \ (A - \Delta A)$ = Area on mirror where the detector "sees" the mirrors in the optics with temperature T_M + emissivity ϵ_M AND the sky with temperature T_S + emissivity ϵ_S.

$\Rightarrow \Delta P$ = [Background Power looking @ mirror + off edge by ΔA]
$\qquad\qquad$ − [Background Power looking only at mirror A]

$$= \left[\epsilon_B B(T_B) - \left(\epsilon_M B(T_M) + \epsilon_S B(T_S) \right) \right] \Delta A \cdot F(R_0) \cdot \Omega_t \cdot \Delta \nu \cdot t$$

where $\quad F(r, \theta) \equiv$ Beam profile function
$\qquad\qquad \Omega_t \equiv$ Solid angle subtended by detector @ tertiary
$\qquad\qquad \Delta \nu \equiv$ bandpass of detector system
$\qquad\qquad t \ \equiv$ transmission of " " .

$$\Rightarrow \frac{\Delta P}{P} = \left[T - 1 \right] \frac{\Delta A \cdot F(R_0)}{\langle A \cdot \text{Beam} \rangle} \qquad \text{where } \langle A \cdot \text{Beam} \rangle = \int_A F(r, \theta) r \, d\theta \, dr$$

+ Where $P \equiv$ Background power looking only at the mirror
Here we have approximated that $\Omega_t \approx$ constant over the tertiary — which is almost true for SOFIA.

$$\Rightarrow \Delta A = \left(\frac{\frac{1}{2}\Delta R}{R_o} \right) \pi R_o^2 = 1.1 \times 10^{-4} R_o^2$$

$$\text{for } R_o \sim 15 \text{ cm}$$

Substituting all assumptions into the eq.^{n} for $\frac{\Delta P}{P}$ gives

$$\frac{\Delta P}{P} = [S-1] \frac{1.1 \times 10^{-4} R_o^2 \cdot \exp\left(-\frac{R_o^2}{\beta^2}\right)}{\pi \beta^2 \left[1 - \exp\left(-\frac{R_o^2}{\beta^2}\right)\right]}$$

$$= \left[1.4 \times 10^{-4} \left(\frac{R_o^2}{\beta^2}\right) \Big/ \left[\exp\left(\frac{R_o^2}{\beta^2}\right) - 1\right] \right]$$

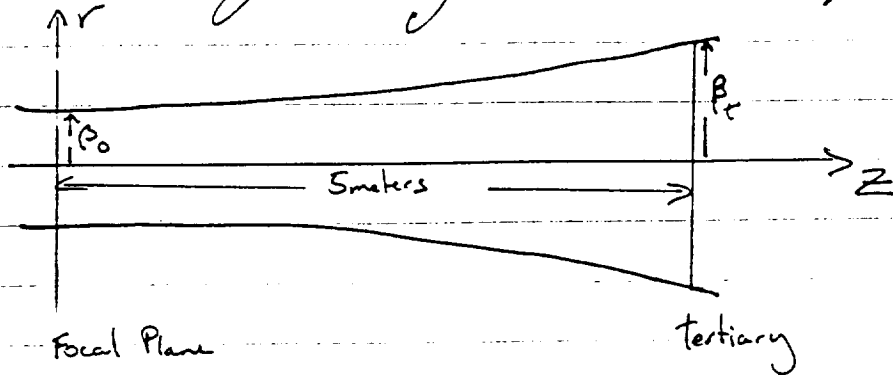$$= \frac{1.4 \times 10^{-4} x^2}{(e^{x^2} - 1)} \qquad \text{where } x = \frac{R_o}{\beta}$$

Here we will adopt the same criterion as Harvey, that is the noise introduced dynamically into the system should be one millionth of the background

$$\Rightarrow \frac{\Delta P}{P} = \frac{1.4 \times 10^{-4} x^2}{(e^{x^2} - 1)} \leq 10^{-6}$$

$$\Rightarrow x \geq 2.6$$

Consider next the following Gaussian Optics

From Goldsmith (1982) in "Infrared and Millimeter Waves" Vol 6
ed: K. J. Button, Academic Press, page 280

$$\beta(z) = \beta_0 \left(1 + \left(\frac{z\lambda}{2\pi\beta_0^2}\right)^2\right)^{1/2}$$

Which for $\lambda = 1.6mm$, $\beta_0 = \frac{(1.22)\lambda \cdot f_\#}{2\sqrt{\ln 2}}$ + $f_\# = 20$

$$\beta(5\text{meters}) = 6\,cm$$

$$\left[\text{Note: } B(z) \rightarrow \frac{z\lambda}{2\pi\beta_0} \approx 5.5\,cm \text{ for smaller } \lambda\right]$$

So if we want $x = \frac{R_0}{\beta_t} \gtrsim 2.6$

$$\Rightarrow R_0 = 15.6\,cm$$

From page 1, geometric optics gives $\frac{25}{2} = 12.5\,cm$
for the radius of the tertiary.

$$\Rightarrow \frac{R_0}{R_t} = \frac{15.6}{12.5} = 1.25$$

$\Rightarrow$ Tertiary should be 25% larger than defined by
the f-cone of the telescope.